Manipulation d’énergie thermique avec des ondes de surface électromagnétique aux échelles micro- et anoscopiques

Sergei Gluchko

To cite this version:

Sergei Gluchko. Manipulation d’énergie thermique avec des ondes de surface électromagnétique aux échelles micro- et anoscopiques. Autre. Université Paris Saclay (COmUE), 2017. Français. NNT : 2017SACLC075 . tel-01630077

HAL Id: tel-01630077
https://theses.hal.science/tel-01630077

Submitted on 7 Nov 2017

NNT : 2017SACLC075

THÈSE DE DOCTORAT DE L'UNIVERSITÉ PARIS-SACLAY,

préparée à CentraleSupélec.

ÉCOLE DOCTORALE N°579

Sciences mécaniques et énergétiques, matériaux et géosciences.

Spécialité de doctorat: Énergétique.

Présentée par

M. Sergei Gluchko

Thermal Energy Manipulation via Electromagnetic Surface Waves at Micro and Nanoscales

Thèse soutenue à Gif-sur-Yvette, le 06/10/2017.

Composition du jury:

M. Antoni Thomas	Maître de conférences, CentraleSupélec	Co-directeur de thèse
M. Greffet Jean-Jacques	Professeur, Institut d'Optique	Président du jury
M. Joulain Karl	Professeur, Université de Poitiers	Examinateur
M. Lemonnier Denis	Directeur de recherche, ISAE-ENSMA	Examinateur
Mme. Robert-Philip Isabelle	Directrice de recherche, Université de Montpellier	Rapportrice
M. de Rossi Alfredo	Ingénieur, Thales Research and Technology	Rapporteur
M. Soufiani Anouar	Directeur de recherche, CentraleSupélec	Examinateur
M. Volz Sebastian	Directeur de recherche, Université de Tokyo	Directeur de thèse

Acknowledgements

I want to thank my wife for incredible support and motivation she gave me during these three years of doctoral school. I also want to thank my parents for helping me at the earliest stages of my studies. I will always appreciate the freedom that they have been giving to me and I am feeling sorry for seeing them not so often during that time.

I would like to express my deepest gratitude and special thanks to my supervisors Thomas Antoni and Sebastian Volz who in spite of being extraordinarily busy with their duties, took time out to hear, guide and keep me on the correct path and allowing me to carry out my projects. I appreciate the time Thomas has spent with me sharing his broad experience in theoretical, experimental, and numerical physics. I am also grateful to both of my supervisors for providing me the opportunities to work on different projects in parallel, visiting scientific conferences and schools, and helping me to build my scientific network.

I also want to thank all the collaborators we worked together for different projects. I want to thank to the team of CALITREC project (Antoine Monmayrant, Evgene Popov, Anne-Laure Fehrembach, Sylvain Augè and Olivier Gauthier-Lafaye) for a valuable impact to my theses work. I want to thank Rèmy Braive who shared his incredible experience in nanofabrication and basically taught me almost everything I know about the clean room. I consider his help to be extremely important for my professional development. I want to thank my friend and a source of inspiration Jose Ordonez-Miranda. I consider his contribution to my theses to be undeniable and appreciate his help to almost any piece of work I have been doing.

I express my deepest thanks to "Nanoteam" at EM2C for taking part in useful decision and giving necessary pieces of advice and guidance and arranged all facilities to make life easier. I choose this moment to acknowledge their contribution gratefully.

It is my radiant sentiment to place on record my best regards, deepest sense of gratitude to Prof. Nomura and all the crew of his lab at University of Tokyo for their welcoming, careful and precious guidance, and their help in the clean room which were extremely valuable for my study both theoretically and practically.

I wanted to acknowledge Gloria Foulet, the head of the Laboratory of Experimental Physics, for the opportunity to work as a teaching assistant during these

three years and preparing the most exciting classes of my life in Superconductivity for engineer students of Ecole Centrale Paris. This was a great teaching experience.

I am also grateful to my friends-neighbors David Mercier, Gizem Okyay, Arthur Salmon, Roman Anufriev and Yunhui Wu who has been taken the desks next to mine at different parts of my PhD for all near-scientific discussions we had together. I also want to thank Mikyung Lim who joined our team for one year and had a significant influence on my work.

I perceive these three years as a big milestone in my career development. I will strive to use gained skills and knowledge in the best possible way, and I will continue to work on their improvement, in order to attain desired career objectives. Hope to continue cooperation with all of you in the future.

Abstract

Surface phonon-polaritons (SPhPs) are evanescent electromagnetic surface waves generated by the phonon-photon coupling and that propagate along the interface of a polar medium (such as SiO_2 and SiC) and a dielectric one. In this work, we investigate possible applications of SPhPs for enhancing the thermal performance of micro- and nanoscale devices, focusing of thermal energy with micro-structures, decreasing the diffraction angles of infrared radiation on sub-wavelength apertures, and demonstrating broadband coherent thermal emission. We also perform infrared spectroscopy microscopy measurements of microscale objects and demonstrate long-range thermally excited surface modes in a broad frequency range. Our results are obtained trough all theory, numerical simulations, and experiment. The results presented in this thesis can have possible applications in fields related to heat transfer, infrared optics, near-field thermal radiation, infrared microscopy, and polaritonics.

Résumé

Les phonons polaritons de surface (SPhPs) sont des ondes électromagnétiques de surface évanescentes générées par le couplage phonon-photon et se propageant le long d'une interface entre un milieu polaire (tel que SiO_2 et SiC) et un diélectrique. Dans ce mémoire, nous nous intéressons à de possibles applications des SPhPs pour améliorer les performances thermiques des nanosystèmes, en focalisant leur énergie thermique avec des micro- et nanostructures, en réduisant leurs angles de diffraction à travers des ouvertures sub-longueur d'onde, et en démontrant leur émission thermique cohérente large-bande. Nous avons aussi effectué des mesures par microscopie spectro-photométrique infrarouge de micro-objets et démontré l'excitation thermique de modes de grandes longueurs de propagation dans un large domaine spectral. Nos résultats sont obtenus sur des bases à la fois théoriques, de simulations numériques et expérimentales. Ces travaux sont pertinents dans les domaines liés au transfert thermique, à l'optique infrarouge, au rayonnement thermique de champ proche, à la microscopie infrarouge, et à la polaritonique.

Contents

List of Figures

General Introduction

Many modern industrial applications require precise control of heat when the sizes of the objects are in the order of hundreds of nanometers. There are numerous different approaches recently proposed which could help to tune the thermal properties of nanostructured materials by using phononic crystals, phonon superlattices, thin layered structures, graphene based structures, and Surface Phonon Polaritons (SPhPs). The latter are electromagnetic surface waves that are coupled with transverse optical phonons of the materials. These surface waves propagate along an interface of two optically active dielectrics and are usually observed for mid-infrared frequencies around 10 μm (that corresponds to the wavelength of maximal thermal emission for a block body at ambient temperature). The important property of these modes is that they can have a very large local density of states and can carry heat energy along the interface. These properties together with the fact that they can have a spatial coherence length of several wavelengths make them potential candidates for various applications in both enhancing the thermal conductivity of the materials and providing coherent thermal near-field radiation close to the interfaces. These surface modes have attracted significant attention during the last decade due to the fact that these effects can be achieved for cheap nontoxic materials frequently used in nano-fabrication (e.g. SiO_2, SiC, BN, VO). However, industrial applications remain challenging as these modes can only be excited in a very narrow frequency range that is limited by the materials used and as their propagation length is not long enough.

In this work, we demonstrate that by modifying the geometry of the interfaces we can significantly increase the performance of these surface modes for thermal applications. We consider amorphous glass as it is the most common dielectric used in nano-fabrication and demonstrate various effects through theory, numerical simulations, and experiments. Our work consists of five main parts. The fist part is a short introduction to the concept of SPhPs and some modern applications of these modes in heat transfer.

The second part consists of three chapters where we study focusing of thermal energy of SPhPs with conical and wedge structures, respectively, as well as superfocalisation of infrared light in far field. The idea of SPhP focusing is based on the tip effect. We perform an optimization of the cone and wedge aperture angles theoretically and study the frequency dependence of the focusing efficiency. In the superfocalisation chapter, we propose an optical system based on two thin parallel membranes supporting long-range surface modes that can significantly reduce the diffraction angles of sub-wavelength apertures. We perform a numerical study for thin amorphous glass membranes and compare the obtained diffraction angles of this new optical system with diffraction on an infinite slit of the same size. We also perform a parametric study of this system. The results obtained in this part will be potentially interesting for infrared near-field microscopy, nanoscale heat extraction devices, and mid-infrared optics.

In the third part of our work, we perform a detailed study of all possible long-range surface modes that can be supported by a plane interface between two dielectrics and by a thin dielectric film symmetrically surrounded by the air. We demonstrate that thin films can support not only SPhPs but also Zenneck and TM-guided thermally excited long-range surface modes theoretically, numerically, and experimentally. We also demonstrate that thin amorphous glass membranes produce coherent thermal radiation almost over the entire infrared spectrum and we experimentally measure the dispersion relation of long-range surface modes in such structure as well as their spatial coherence length. Based on our experimental results, we estimate the contribution of this long-range surface modes to the thermal conductivity of thin films to be more than one order of magnitude larger than the one of phonons. These outcomes are of possible interest for anyone working on surface waves as well as for the nanoscale heat transfer community and near-field radiation community.

The fourth and the last part shows the results of an ANR collaboration with our partners in designing a tunable Quantum Cascade Laser (QCL). We performed infrared optical characterization of very resonant infrared mirrors designed to reflect the output of the QCL. We developed an experimental methodology of infrared characterization of micro-size optical devices in reflectivity regime as well as infrared mapping of the spectral reflectivity for small incidence angles. This part of the work should be useful for the far-field infrared spectral microscopy community and for those interested in QCLs.

Part I

Introduction

Chapter 1

Heat Manipulation with Surface Waves

In this chapter, we briefly review the concept of Surface Phonon Polaritons and some of their applications.

1.1 Surface Phonon Polaritons

A polariton is a boson quasi-particle resulting from a strong coupling of electromagnetic surface wave with a dipole-like excitation. Surface Polaritons (SP) can be formed at the interface of two materials as an electromagnetic wave propagating along the interface and exponentially decreasing in the direction perpendicular to it. SP at the interface of metal and dielectric is called Surface-Plasmon Polariton (SPP). When Surface Polaritons are excited at the interface of two dielectrics due to the coupling of an optical phonon with the electromagnetic field, the SP is called Surface Phonon Polariton (SPhP). Plasmon polaritons and phonon polaritons can also exist in the whole volume of the material. Excellent reviews about SPhPs can be found in Joulain, Mulet, Marquier, Carminati, and Greffet (2005) and John Polo (2013).

Let us consider an interface between a polar dielectric (e.g. SiO_2, SiC, SiN) and air as shown on figure 1.1. The dipoles close to the interface emit an electromagnetic field as a result of the presence of transverse optical modes of phonons. This field can be either propagating to the far-field or being coupled to the interface between the materials. If the electromagnetic field was coupled to the interface, it can propagate along the interface until being scattered to the far-field or absorbed by the material. The mean free path of this electromagnetic wave can be significantly larger than the mean free path of phonons causing the propagation of heat energy through the electromagnetic field.

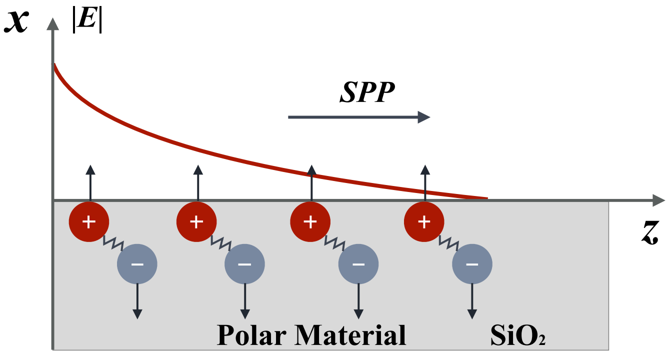

Figure 1.1: *Schematic illustration of Surface Phonon Polaritons excited at the interface of a polar dielectric and air.*

The propagation of the electromagnetic field is analyzed by solving Maxwell's equations under proper boundary conditions and is demonstrated in the chapter 5 for the SiO_2-air interface in details. An important feature of SPhPs is that they can only be excited in TM polarization.
The fact that the SPhPs are formed by such a coupling of phonons with electromagnetic field causes a comparatively large spatial coherence length of this mode. Indeed, it has been demonstrated in Greffet, Carminati, Joulain, Mulet, Mainguy, and Chen (2002) that by fabricating a diffraction grating on the surface of such a polar material, one can observe a directive diffraction of thermal radiation due to the grating. However it has been only observed in a very narrow frequency region where the SPhPs can be excited. This effect is discussed in details in the chapter 5.
Another interesting property of SPhPs is that all the energy density of these modes increases close to the interface and increases exponentially close to the interface. Also note that for modes close to the transverse optical phonon resonance the local density of states is very large. Figure 1.2 demonstrates energy density above a SiO_2 plane heated up to $T = 300$ K and vacuum at $T = 0$ K as reported in Joulain, Mulet, Marquier, Carminati, and Greffet (2005). When the energy density is considered far above the plane (the distance from the plane is greater than the wavelength) for distances around 100 μm, the spectral energy density profile is given by the Planck's law. When going close the interface, the Planck's law is not longer valid as it assumes far-field radiation only and the energy density at a distance 100 nm close to the surface exhibits a strong peak in the thermal energy density spectrum. Hence, the near-field thermal radiation can be considered as monochromatic in this case.
Not all materials supporting surface waves exhibit strong peaks in their near-field thermal energy density spectrum. For example, metals exhibit Surface Plasmon Polariton in the UV or visible range but do not exhibit strong peak in their thermal energy density spectrum in the near field.

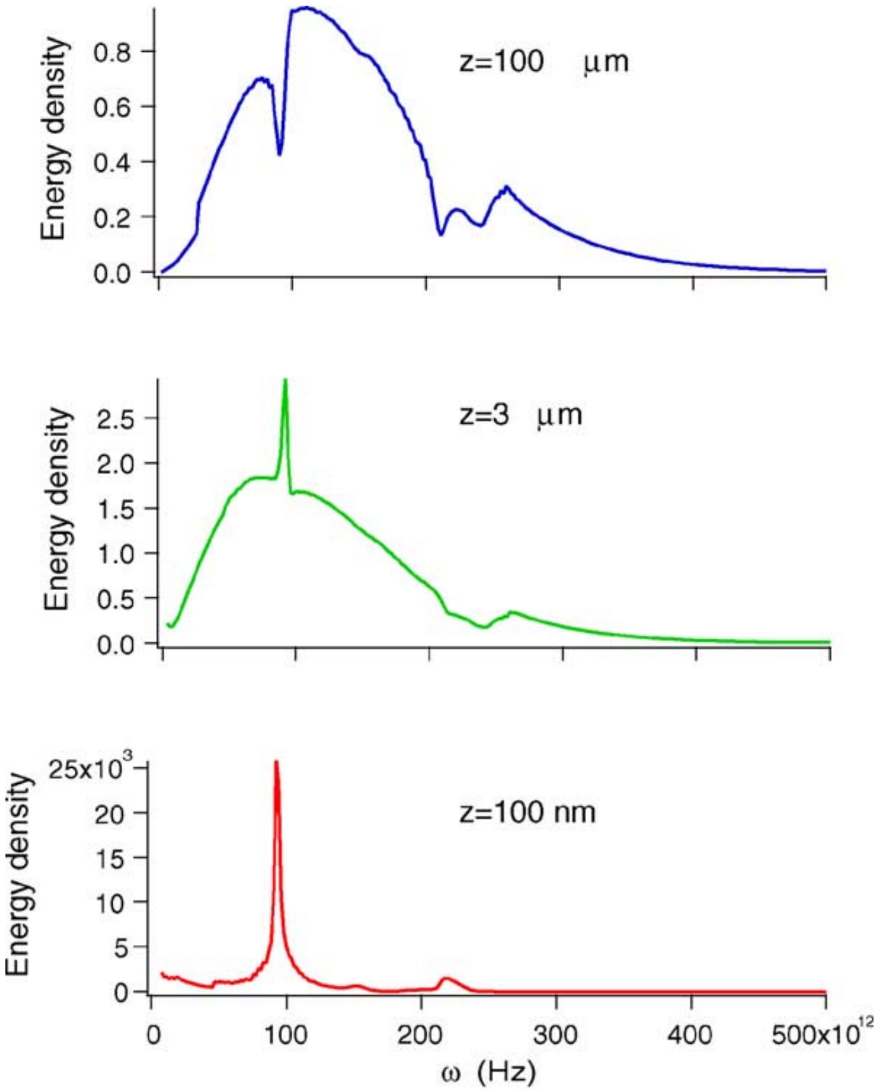

Figure 1.2: *Electromagnetic energy density above a plane interface separating glass at $T = 300$ K from vacuum at $T = 0$ K for different distances above the plane. The figure is reported by Joulain, Mulet, Marquier, Carminati, and Greffet (2005).*

This interesting property of near-field polar dielectric thermal radiation has attracted a lot of attention due to its potential applications in photovoltaics Fan (2014). Figure 1.3 shows a schematic illustration of a thermophotovoltaic device which uses a monochromatic near-field radiation of high energy density to efficiently convert solar radiation into electrical energy. Such kind of devices seems to be a very promising way to increase the efficiency and to lower the cost of solar cells. However there are technological difficulties in creating such thin gaps of few hundreds of nanometers for large systems as well as there is a problem of overheating of these devices.

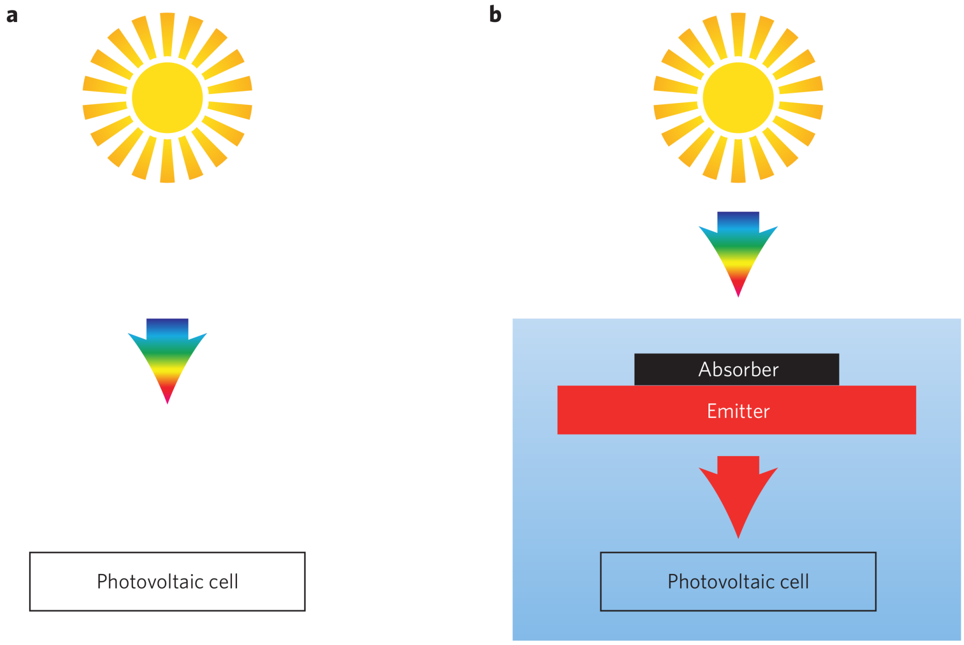

Figure 1.3: *Working principle of a solar thermophotovoltaic system. (a) A standard photovoltaic cell directly exposed to sunlight. (b) In an thermophotovoltaic system, an intermediate material is placed between the sun and the photovoltaic cell. The intermediate material absorbs the sunlight, heats up and generates a thermal radiation that is emitted towards the photovoltaic cell. Fan (2014).*

Another interesting device based on SPhPs was proposed in Rephaeli, Raman, and Fan (2013) and consists of multiple layers of nanostructured materials supporting SPhPs as shown on figure 1.4(a). The purpose of this device is to passively cool objects by tuning the spectral emissivity of the surface of the object. For example, such a device can be installed on the roofs of the buildings to lower the temperature inside. Normalized solar spectrum and spectral transmittance of the atmosphere are shown on figure 1.4(b). The idea of the device is based on the fact that the spectral emissivity can be tuned in such a way that the device behaves as a mirror for the frequencies of the solar spectrum and as an absorber for the frequencies where the atmosphere is transparent. Thus, such a device should reflect most of the solar energy and emit thermal radiation into 'cold' space through the atmospheric window. This process should cause the drop of the device temperature and can be potentially used as a radiative passive cooler. This is a very important finding as such devices can significantly lower building cooling energy consumption.

The idea of modifying the spectral emissivity was first proposed in Greffet, Carminati, Joulain, Mulet, Mainguy, and Chen (2002). We discuss it in details in the chapter 5. The efficiency and the frequency range of such devices are usually limited by the short spatial coherence length and the narrow frequency range of SPhPs existence. In the chapter 6, we experimentally demonstrate that such systems can be significantly improved and demonstrate a broadband thermal source of coherent radiation using long-range thermally excited surface waves.

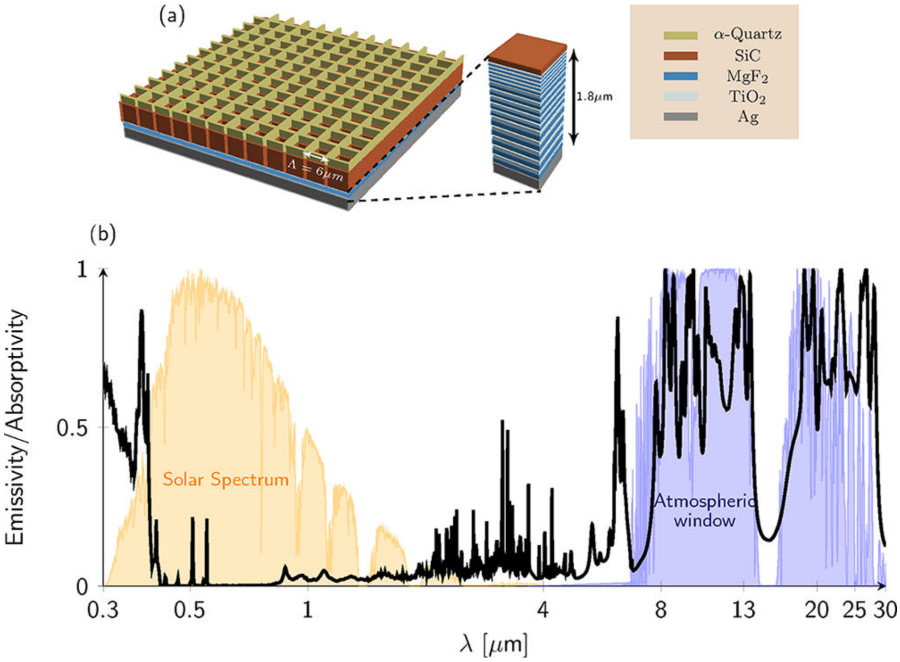

Figure 1.4: *(a) Optimized daytime radiative cooler design that consists of two thermally emitting photonic crystal layers composed of SiC and quartz, below which lies a broadband solar reflector. The reflector consists of three sets of five bilayers made of MgF_2 and TiO_2 with varying periods on a silver substrate. (b) Emissivity of the optimized daytime radiative cooler at normal incidence (black) with the solar spectrum (yellow) and atmospheric transmittance (blue) plotted for reference. The structure has minimal absorption throughout the solar spectrum and has very strongly selective emission in the atmospheric transparency window, as is desirable and necessary for a high-performance daytime radiative cooler Rephaeli, Raman, and Fan (2013).*

Another interesting application of SPhPs is IR energy focusing demonstrated in Huber, Deutsch, Novotny, and Hillenbrand (2008) . They used a gold arc deposited on SiC surface to demonstrate concentration of SPhPs by using the tip of a scattering-type near-field optical microscope shown on figure 1.5. This effect can be used in near-field infrared microscopy and for heat extraction devices due to the unique properties of SPhPs. However, SPhPs receive small attention comparatively to SPPs and some other focusing systems should be studied that allows for efficient concentration of SPhPs. We discuss such structures in details in the chapters 2 and 3.

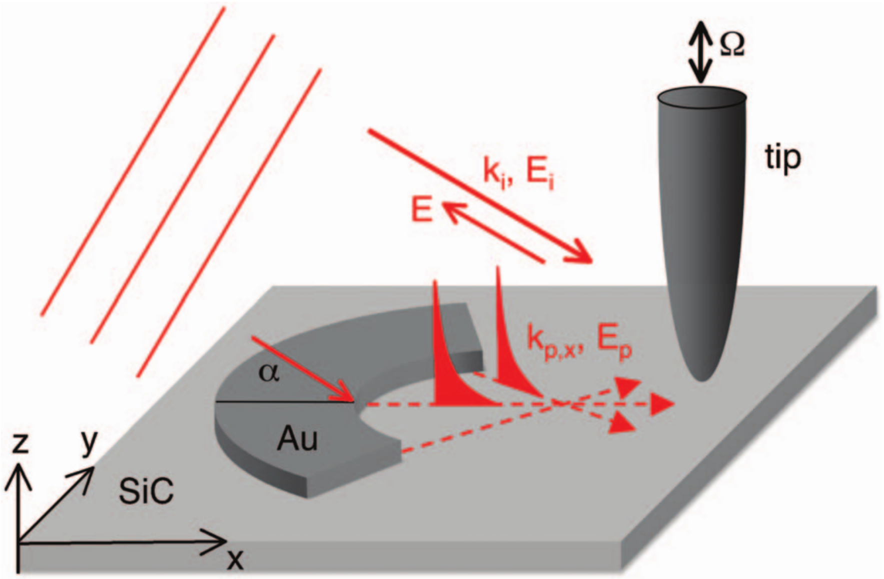

Figure 1.5: *Experimental setup for demonstrating SPhP focusing. A circular Au structure excites and focuses surface phonon polaritons on a SiC crystal when illuminated by a plane wave with* $\lambda = 10.85\ \mu m$. *The tip of a scattering-type near-field optical microscope scans the sample surface in order to map the local field Rephaeli, Raman, and Fan (2013).*

It has been also proposed in Chen, Narayanaswamy, and Chen (2005) and in Ordonez-Miranda, Tranchant, Tokunaga, Kim, Palpant, Chalopin, Antoni, and Volz (2013) that SPhPs should provide an alternative channel of heat transport at nanoscale due to their phonon-photon nature. We discuss this effect in details in the chapters 5 and 6. We believe that not only SPhPs contribute to the heat transport but also other long-range surface modes that can be thermally excited in such materials.

1.2 Objective of this work

The objective of this work is to develop new applications of SPhPs such as focusing of IR energy with conical and wedge structures, using SPhPs for decreasing the diffraction angles of sub-wavelength apertures, and increasing the thermal conductivity of nanoscale objects. We also want to demonstrate that not only SPhPs should be considered for such applications but also Zenneck and TM-guided long-range surface modes. By using these long-range thermally excited surface waves, we demonstrate coherent thermal source for a significantly broader frequency range that was originally demonstrated in the literature. We also estimated the thermal conductivity contribution due to these modes of thin

membranes to be one order of magnitude larger than the one due to SPhPs.
Aside from these works on SPhPs, and as a part of the collaboration project, we develop an infrared spectral microscopy mapping of reflectivity for incidence angles close to zero and use this methodology to perform an experimental mapping and an optical characterization of highly selective infrared mirrors for a new tunable Quantum Cascade Laser.
We believe that our work is original and should be useful for a wide range of researches related both on fundamental aspects of infrared optics and radiative nanoscale heat transfer as well as for those in connection with industrial applications.

Part II

Focusing of Thermal Radiation

Chapter 2

Focusing with Conical Glass Structures

In this chapter, we demonstrate the possibility of thermal energy focusing using the concept of surface phonon-polariton concentration with a conical tip fabricated from amorphous glass. We study this system theoretically based on Maxwell's equations and optimize the focusing efficiency by adjusting the geometrical parameters of the structure. Such a structure could potentially be applied for heat extraction from nano-scale objects, microscopy, and thermal emission. These results have been reported in our article Gluchko, Ordonez-Miranda, Tranchant, Antoni, and Volz (2015).

2.1 Introduction

Surface phonon-polaritons (SPhPs) are evanescent electromagnetic surface waves generated by the phonon-photon coupling and that propagate along the interface of a polar medium (such as SiO_2 and SiC) and a dielectric one as shown on Figure 2.1. Taking into account the high surface-to-volume ratio of nanomaterials, SPhPs are expected to be powerful energy carriers, with the potential to provide an additional pathway to the one of phonons for the energy transport along polar nanomaterials and therefore to enhance significantly their thermal conductance. Based on this key feature of SPhPs, different research groups have proposed that SPhPs could be applied to improve the stability and thermal performance of nanoscale devices in electronics Mills (1975) Kume, Kitagawa, Hayashi, and Yamamoto (1998) Mulet, Joulain, Carminati, and Greffet (2001) Chen, Narayanaswamy, and Chen (2005), in thermal emission Wilde, Formanek, Carminati, Gralak, Lemoine, Joulain, Mulet, Chen, and Greffet (2006) Greffet, Carminati, Joulain, Mulet, Mainguy, and Chen (2002) and in microscopy Wilde, Formanek, Carminati, Gralak, Lemoine, Joulain, Mulet, Chen, and Greffet (2006) Wilde, Formanek, Carminati, Gralak, Lemoine, Joulain, Mulet, Chen, and Greffet (2006). Controlling, guiding, and focusing of polaritons in metals (surface plasmon-polaritons) have been intensively studied at near-infrared and visible wavelengths, both theoretically and experimentally Bouhelier, Huser, Tamaru, Guntherodt, Pohl, Baida, and Labeke (2001) Vernon, Gramotnev, and Pile (2007). However, comparatively less attention has been given to their propagation in polar media (surface phonon-polaritons). Ordonez-Miranda *et al.* have determined the SPhP thermal conductivity in thin films Ordonez-Miranda, Tranchant, Tokunaga, Kim, Palpant, Chalopin, Antoni, and Volz (2013) and the SPhP thermal conductance in nanowires Ordonez-Miranda, Tranchant, Kim, Chalopin, Antoni, and Volz (2014b), and they showed that the SPhP energy contribution can be as high as the one of phonons. Furthermore, the transmission and reflection of SPhPs across dielectric interfaces were analytically described and the SPhP energy distribution at those interfaces was also determined Ordonez-Miranda, Tranchant, Gluchko, Antoni, and Volz (2014).

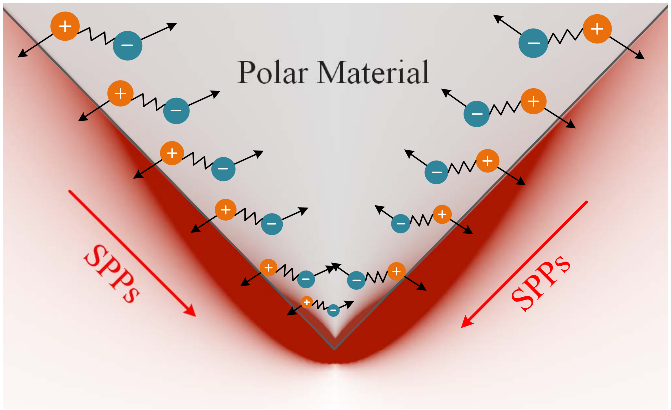

Figure 2.1: *Scheme of the generation of SPhPs by the fluctuation of electrical dipoles in a conical structure. The color density stands for the typical intensity of the SPhP field.*

Focusing of SPhPs could be essential for many applications that require highly localized infrared fields such as photodetectors, thermal emitters Wilde, Formanek, Carminati, Gralak, Lemoine, Joulain, Mulet, Chen, and Greffet (2006)Greffet, Carminati, Joulain, Mulet, Mainguy, and Chen (2002) or energy extractors at nanoscales Huber, Deutsch, Novotny, and Hillenbrand (2008). Based on the scanning near-field infrared microscopy, Huber *et al.* conducted the first experiments for 2D focusing of SPhPs in a SiC crystal, and detected a remarkable enhancement of the intensity of the electrical field, due to the presence of SPhPs. The excitation of surface plasmons in a 3D metallic conical structure was also achieved by inscribing a grating onto its surface, which allows to convert light into plasmons propagating towards the cone tip Ropers, Neacsu, Elsaesser, Albrecht, Raschke, and Lienau (2007). The theoretical description of the surface plasmon-polariton focusing along slender cones and wedges was addressed by Babadjanyan *et al.* Babadjanyan, Margaryan, and Nerkararyan (2000) and Nerkararyan Nerkararyan (1997), respectively; and they showed that as the surface plasmon-polaritons approach the tip of these structures, their wavelength reduces to zero and the intensity of the electrical field increases without limit. The results of these works are valid for cones and wedges with only sharp tips and small aperture angles, and they were reported without considering any particular material. More recently and based on the method of quasi-separation of variables, Kurihara *et al.* Kurihara, Otomo, Syouji, Takahara, Suzuki, and Yokoyama (2007) Kurihara, Yamamoto, Takahara, and Otomo (2008) extended these previous results,Babadjanyan, Margaryan, and Nerkararyan (2000) Nerkararyan (1997) for conical and wedge metallic structures of arbitrary aperture angle. Even though these two latter works reported the dispersion relations of surface plasmon-polaritons propagating along both of these structures, they did not present their analysis neither in the full range of possible excitation frequencies nor as a function of the aperture angle.

In this chapter, we study the SPhP focusing along SiO_2 cones, in the whole range of possible excitation frequencies and aperture angles. Based on the analytic solutions of Maxwell's equations, the SPhP dispersion relation is obtained. The set of optimal apertures angles and critical frequencies that maximize the SPhP focusing are also determined and compared. It is shown that the cone is an efficient structure for focusing the SPhP energy density. Taking into account the conservation of energy and the reduction of the cross-section area of the cone as the SPhPs travel towards its tip, the Poynting vector is expected to diverge at the cone tip, as shown below.

2.2 Maxwell's equations analysis for spherical geometry

Our research is based on Maxwell's formalism. We use a nonmagnetic material with a complex dielectric function. One of the most common choices for the materials that could be used to fabricate an interface for SPhPs existence and propagation are combinations of silicon dioxide or silicon carbide with air. The first two materials have frequency depending permittivities (dispersive materials) and both of them are lossy. That means that the permittivity of such materials could be written as a complex number using following formalism:

$$\epsilon = \epsilon_r - i\epsilon_i. \tag{2.1}$$

The value of the imaginary part of the permittivity, ϵ_i, corresponds to lossy properties of dielectric media and cannot be negative.

In order to build a mathematical model of electromagnetic waves one needs to analyze Maxwell's equations, using variables $\epsilon = \epsilon_0 \epsilon_\mathrm{m}$ and $\mu = \mu_0 \mu_\mathrm{m}$ Jackson

(1998) and the formalism proposed in the Equation 2.1. Where ϵ_{m} and μ_{m} are the relative permittivity and relative permeability of the material respectively.

$$\begin{aligned} \boldsymbol{\nabla}\cdot\mathbf{B} =& 0 && (2.2)\\ \boldsymbol{\nabla}\cdot\mathbf{D} =& 0 && (2.3)\\ \boldsymbol{\nabla}\times\mathbf{H}-\frac{\partial\mathbf{D}}{\partial t} =& \mathbf{0} && (2.4)\\ \boldsymbol{\nabla}\times\mathbf{E}+\frac{\partial\mathbf{B}}{\partial t} =& \mathbf{0}. && (2.5) \end{aligned}$$

In absence of sources the following expressions for the fields are valid:

$$\begin{aligned} \mathbf{E}(\mathbf{r},t) &= \mathbf{E}(\mathbf{r})e^{i\omega t} && (2.6)\\ \mathbf{H}(\mathbf{r},t) &= \mathbf{H}(\mathbf{r})e^{i\omega t}. && (2.7) \end{aligned}$$

Using this assumption, Equations 2.2-2.5 yield:

$$\begin{aligned} \boldsymbol{\nabla}\times\mathbf{E}+i\mu\omega\mathbf{H} =& \mathbf{0} && (2.8)\\ \boldsymbol{\nabla}\times\mathbf{H}-i\epsilon\omega\mathbf{E} =& \mathbf{0}. && (2.9) \end{aligned}$$

Applying rotor to both Equations 2.8 and 2.9:

$$\begin{aligned} \left(\boldsymbol{\nabla}^2+\mu\epsilon\omega^2\right)\mathbf{E} =& \mathbf{0} && (2.10)\\ \left(\boldsymbol{\nabla}^2+\mu\epsilon\omega^2\right)\mathbf{H} =& \mathbf{0}. && (2.11) \end{aligned}$$

These equations are obtained for any coordinate system for any uniform material without sources Jackson (1998).
A new variable $k_0 = \sqrt{\epsilon_0\mu_0}\omega$ is used to switch from ϵ and μ to ϵ_{m} and μ_{m} which describe properties of the materials. From now on, to simplify the writing we will note ϵ_{m} and μ_{m} as ϵ and μ respectively. In this case Equation 2.8 and Equation 2.9 should be written as:

$$\begin{aligned} \left(\boldsymbol{\nabla}^2+\mu\epsilon {k_0}^2\right)\mathbf{E} =& \mathbf{0} && (2.12)\\ \left(\boldsymbol{\nabla}^2+\mu\epsilon {k_0}^2\right)\mathbf{H} =& \mathbf{0}. && (2.13) \end{aligned}$$

2.2.1 Spherical coordinates

Focusing of SPhPs energy means increasing the surface to volume fraction in a direction of SPhPs propagation. The most elegant way to do so is to use a tip effect. It means that one needs to fabricate a cone of SiO_2 in air with a very sharp tip. The SPhPs could be excited by heating the wide part of the cone. The excited electro-magnetic waves propagate from the heated wide part of the cone towards the tip, causing focusing of the electro-magnetic field close to the tip as shown on Figure 2.2.

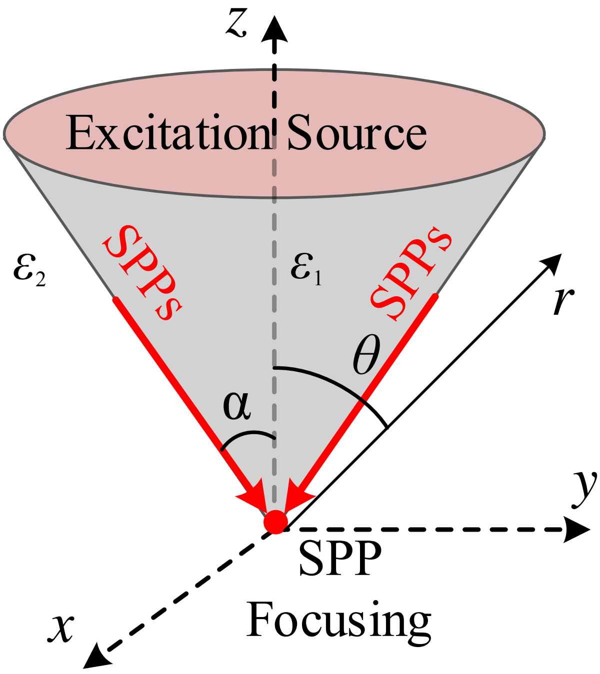

Figure 2.2: *Schematic illustration of the conical SiO_2 structure in air. The red arrows indicate the direction of SPhP focusing.*

The best way to describe such a system is to use standard spherical coordinates shown on Figure 2.3:

$$r = \sqrt{x^2 + y^2 + z^2} \tag{2.14}$$

$$\theta = \cos^{-1}\left(\frac{z}{\sqrt{x^2 + y^2 + z^2}}\right) \tag{2.15}$$

$$\varphi = \tan^{-1}\left(\frac{y}{x}\right). \tag{2.16}$$

To simplify the calculations, let us consider the heat source to be uniform in φ. It means that due to the symmetry of the system, the electrical and magnetic field components are independent of φ:

$$\mathbf{E} = \mathbf{E}(r,\theta) \tag{2.17}$$

$$\mathbf{H} = \mathbf{H}(r,\theta). \tag{2.18}$$

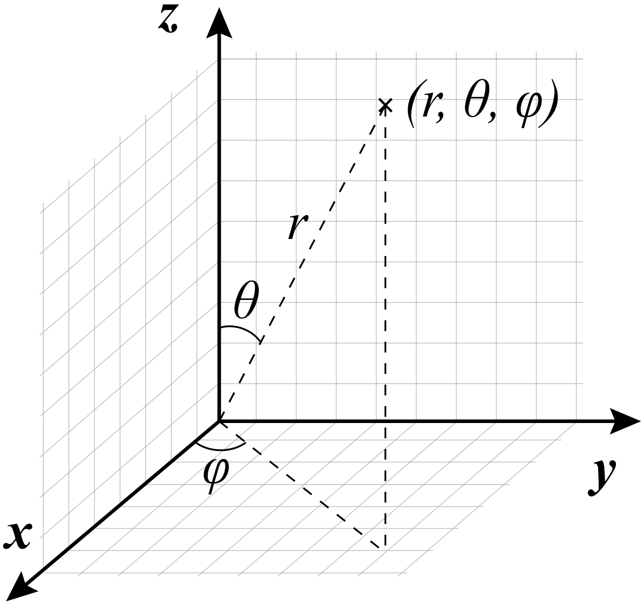

Figure 2.3: *The spherical coordinates used to build the theoretical model of SPhP focusing in conical structure.*

Taking into account that the fields are independent of φ $\left(\frac{\partial \mathbf{E}}{\partial \varphi} = \frac{\partial \mathbf{H}}{\partial \varphi} = 0\right)$ and using the form of the curl operator, Equation 2.8 and 2.9 could be rewritten for each component in the following way:

$$i\mu\omega H_r = -\frac{1}{r\sin(\theta)}\frac{\partial(E_\varphi \sin(\theta))}{\partial\theta} \tag{2.19}$$

$$i\mu\omega H_\theta = \frac{1}{r}\frac{\partial(rE_\varphi)}{\partial r} \tag{2.20}$$

$$i\mu\omega H_\varphi = -\frac{1}{r}\left(\frac{\partial(rE_\theta)}{\partial r} - \frac{\partial E_r}{\partial\theta}\right) \tag{2.21}$$

$$i\epsilon\omega E_r = \frac{1}{r\sin(\theta)}\frac{\partial(H_\varphi \sin(\theta))}{\partial\theta} \tag{2.22}$$

$$i\epsilon\omega E_\theta = -\frac{1}{r}\frac{\partial(rH_\varphi)}{\partial r} \tag{2.23}$$

$$i\epsilon\omega E_\varphi = -\frac{1}{r}\left(\frac{\partial(rH_\theta)}{\partial r} - \frac{\partial H_r}{\partial\theta}\right). \tag{2.24}$$

2.2.2 TM-polarization in spherical coordinates

To simplify the problem, the system could be analyzed for TM and TE polarizations separately. The mathematical approach for these two types of polarizations is the same so let us assume that the wave is polarized in such a way that the radial component of the magnetic field is zero everywhere $H_r = 0$ (TM polarized). For TE polarization, one needs to assume the radial component of the electrical field to be zero. After applying the assumption of the TM polarization, the system of Equations 2.19 - 2.24 simplifies:

$$H_r = 0 \tag{2.25}$$

$$H_\theta = 0 \tag{2.26}$$

$$i\mu\omega H_\varphi = \frac{1}{r}\frac{\partial E_r}{\partial \theta} \tag{2.27}$$

$$i\epsilon\omega E_r = \frac{1}{r\sin(\theta)}\frac{\partial (H_\varphi \sin(\theta))}{\partial \theta} \tag{2.28}$$

$$i\epsilon\omega E_\theta = -\frac{1}{r}\frac{\partial (rH_\varphi)}{\partial r} \tag{2.29}$$

$$E_\varphi = 0. \tag{2.30}$$

Applying the same derivation to the TE polarization, one can get the following equations:

$$i\mu\omega H_r = -\frac{1}{r\sin(\theta)}\frac{\partial (E_\varphi \sin(\theta))}{\partial \theta} \tag{2.31}$$

$$i\mu\omega H_\theta = \frac{1}{r}\frac{\partial (rE_\varphi)}{\partial r} \tag{2.32}$$

$$H_\varphi = 0 \tag{2.33}$$

$$E_r = 0 \tag{2.34}$$

$$E_\theta = 0 \tag{2.35}$$

$$i\epsilon\omega E_\varphi = -\frac{1}{r}\left(\frac{\partial (rH_\theta)}{\partial r} - \frac{\partial H_r}{\partial \theta}\right). \tag{2.36}$$

It could be shown that there is no SPhP travelling towards to the tip for TE polarization using the same approach that will be done for the TM polarization (solving Maxwell's equations under proper boundary conditions). The fact that TE polarization does not support SPhP is also discussed in Ordonez-Miranda, Tranchant, Kim, Chalopin, Antoni, and Volz (2014b) Agranovich and Mills (1982). The question of TE polarization will not be discussed in this work anymore and all the calculations will be done for TM-polarized electro-magnetic field.

The most convenient way to solve Maxwell's equations is first to solve Equation 2.13 for the H_φ component of the field and then apply the system Equation 2.25 - Equation 2.30 to find all the components of the fields. Equation 2.13 can be rewritten in the following form:

$$(\boldsymbol{\nabla}^2\mathbf{H}_\varphi) + \mu\epsilon {k_0}^2 H_\varphi = 0. \tag{2.37}$$

Using a new variable $\lambda = \mu\epsilon {k_0}^2$, the vector formula for the Laplace operator in spherical coordinates reported in Moon and Spencer (1988), Equation 2.29 and Equation 2.30, and the assumption of uniform heat source, the Equation 2.37 can be written as:

$$\frac{1}{r^2}\frac{\partial}{\partial r}\left(r^2\frac{\partial H_\varphi}{\partial r}\right) + \frac{1}{r^2\sin(\theta)}\frac{\partial}{\partial\theta}\left(\sin(\theta)\frac{\partial H_\varphi}{\partial\theta}\right) - \frac{H_\varphi}{r^2\sin^2(\theta)} + \lambda^2 H_\varphi = 0. \tag{2.38}$$

Equation 2.37 can be solved using new variables $\rho = \lambda r$ and $x = \cos(\theta)$ based on the Fourier method Arfken and Weber (2001). When applying this method the following assumption on the H_φ is done:

$$H_\varphi(r,\theta) = R(r)T(\theta) \tag{2.39}$$

After using the Fourier method, Equation 2.38 can be written as a system of Equation 2.40 and Equation 2.41, where $\alpha^2 = -\eta(\eta+1)$ is a separation constant.

$$\rho^2 R''(\rho) + 2\rho R'(\rho) + \left(\rho^2 + \alpha^2\right) R(\rho) = 0 \tag{2.40}$$

$$(1-x^2)T''(x) - 2xT'(x) + \left(-\alpha^2 - \frac{1}{1-x^2}\right) = 0 \tag{2.41}$$

The primes indicate the derivatives with respect to the only one dependent variables ρ and x for Equation 2.40 and 2.41 respectively. Equation 2.40 is a Spherical Bessel equation Olver, Lozier, Boisvert, and Clark (2010) which has a general solution in the form of:

$$R(\rho) = c_1 j_\eta(\rho) + c_2 y_\eta(\rho) \tag{2.42}$$

Where $j_\eta(\rho)$ and $y_\eta(\rho)$ are spherical Bessel functions of first and second kind respectively. Equation 2.41 is a General Legendre equation Olver, Lozier, Boisvert, and Clark (2010) which has a general solution in form of:

$$T(x) = C_1 P_\eta^{(1)}(x) + C_2 P_\eta^{(1)}(-x) \tag{2.43}$$

Where $P_{\eta}^{(1)}(x)$ is a Legendre function of the first order.
Switching back from the variables ρ and x to the spherical coordinates r and θ and using Equation 2.39 the magnetic field component H_{φ} can be written as follows:

$$H_{\varphi}(r,\theta) = \left[C_1 P_{\eta}^{(1)}(\cos(\theta)) + C_2 P_{\eta}^{(1)}(-\cos(\theta))\right] \left[c_1 j_{\eta}(\lambda r) + c_2 y_{\eta}(\lambda r)\right]. \tag{2.44}$$

The other components of the electro-magnetic field can be easily found by substituting Equation 2.44 into the Equation 2.30 - Equation 2.34.

2.3 Dispersion Relation of the surface modes for the cone

2.3.1 TM-polarized field in the cone

When applying Equation 2.44 to the conical geometry the electromagnetic fields components should not be infinite for $\theta = 0$ and $\theta = \pi$. Hence, the constants C_1 should be zero outside the cone and $C_2 = 0$ inside the cone due to the properties of the Legendre functions of first order reported in Olver, Lozier, Boisvert, and Clark (2010). The constant c_2 is chosen to be zero taking into account the fact that spherical Bessel functions of second kind cannot contribute to the fields when going closer to the tip. It should also be noticed that η is a complex number due to the fact that we are working with a complex permittivity and can be written using the same formalism as in Equation 2.1:

$$\eta = \eta_r - i\eta_i \tag{2.45}$$

Equation 2.44 after simplifications could be written for the regions inside and outside the cone:

$$H_{\varphi}^{in}(r,\theta) = C_1 c_1 P_{\eta}^{(1)}(\cos(\theta)) j_{\eta}(\lambda^{in} r) \tag{2.46}$$

$$H_{\varphi}^{out}(r,\theta) = C_2 c_1 P_{\eta}^{(1)}(-\cos(\theta)) j_{\eta}(\lambda^{out} r) \tag{2.47}$$

The fact that the region of interest is the tip of the cone makes possible to apply a first order approximation to the spherical Bessel functions of a first kind reported in Olver, Lozier, Boisvert, and Clark (2010) $j_{\eta}(\lambda r) \sim (\lambda r)^{\eta}$. Finally, Equation 2.46 and Equation 2.47 could be written for the regions inside and outside the cone for small radius as:

$$H_{\varphi}^{in}(r,\theta) = A(\eta) P_{\eta}^{(1)}(\cos(\theta)) r^{\eta} \tag{2.48}$$

$$H_{\varphi}^{out}(r,\theta) = B(\eta) P_{\eta}^{(1)}(-\cos(\theta)) r^{\eta} \tag{2.49}$$

Substituting Equation 2.48 and 2.49 into Equation 2.30 - 2.34 all the components of the electro-magnetic field can be easily found inside the cone:

$$H_r^{in} = 0 \tag{2.50}$$

$$H_\theta^{in} = 0 \tag{2.51}$$

$$H_\varphi^{in} = A(\eta) P_\eta^{(1)}(\cos(\theta)) r^\eta \tag{2.52}$$

$$E_r^{in} = \frac{A(\eta)}{i\epsilon_1 \omega \sin(\theta)} r^{\eta-1} \left[\cos(\theta) P_\eta^{(1)}(\cos(\theta)) - \sin^2\theta \frac{\partial P_\eta^{(1)}(\cos(\theta))}{\partial \cos(\theta)} \right] \tag{2.53}$$

$$E_\theta^{in} = \frac{A(\eta)(\eta+1)}{i\epsilon_1 \omega} r^{\eta-1} P_\eta^{(1)}(\cos(\theta)) \tag{2.54}$$

$$E_\varphi^{in} = 0 \tag{2.55}$$

And outside the cone:

$$H_r^{out} = 0 \tag{2.56}$$

$$H_\theta^{out} = 0 \tag{2.57}$$

$$H_\varphi^{out} = B(\eta) P_\eta^{(1)}(-\cos(\theta)) r^\eta \tag{2.58}$$

$$\begin{aligned} E_r^{out} = \frac{B(\eta)}{i\epsilon_2 \omega \sin(\theta)} r^{\eta-1} \Bigg[& \cos(\theta) P_\eta^{(1)}(-\cos(\theta)) - \\ & - \sin^2\theta \frac{\partial P_\eta^{(1)}(-\cos(\theta))}{\partial \cos(\theta)} \Bigg] \end{aligned} \tag{2.59}$$

$$E_\theta^{out} = \frac{B(\eta)(\eta+1)}{i\epsilon_2 \omega} r^{\eta-1} P_\eta^{(1)}(-\cos(\theta)) \tag{2.60}$$

$$E_\varphi^{out} = 0 \tag{2.61}$$

Where ϵ_1 and ϵ_2 are the relative permittivities of silicon dioxide and air respectively. $A(\eta)$, $B(\eta)$ are functions only of the propagation parameter η and the thermal source. The relative permeability of both materials is $\mu = 1$.

2.3.2 Boundary conditions for the conical interface

In order to find the electromagnetic field in the conical structure, the proper boundary conditions should be satisfied. For the interface between two dielectrics the tangential components of the fields should be the same at the interface Jackson (1998). The boundary conditions for the spherical coordinates are:

$$H_\varphi^{in}|_{\theta=\alpha} = H_\varphi^{out}|_{\theta=\alpha} \tag{2.62}$$
$$E_r^{in}|_{\theta=\alpha} = E_r^{out}|_{\theta=\alpha}, \tag{2.63}$$

Where α is the aperture angle of the cone.
Using Equations 2.52 - 2.61 one can obtain:

$$A(\eta)P_\eta^{(1)}(\cos(\alpha)) = B(\eta)P_\eta^{(1)}(-\cos(\alpha)) \tag{2.64}$$

$$\begin{gathered}\frac{A(\eta)}{i\epsilon_1\omega\sin(\alpha)}r^{\eta-1}\left[\cos(\alpha)P_\eta^{(1)}(\cos(\alpha)) - \sin^2\alpha\frac{\partial P_\eta^{(1)}(\cos(\alpha))}{\partial\cos(\alpha)}\right] = \\ = \frac{B(\eta)}{i\epsilon_2\omega\sin(\alpha)}r^{\eta-1}\left[\cos(\alpha)P_\eta^{(1)}(-\cos(\alpha)) - \sin^2\alpha\frac{\partial P_\eta^{(1)}(-\cos(\alpha))}{\partial\cos(\alpha)}\right].\end{gathered} \tag{2.65}$$

Using the boundary conditions for the H_φ component Equation 2.64 and by introducing a new constant γ, the electro-magnetic field can be written for the region inside the cone:

$$H_r^{in} = 0 \tag{2.66}$$
$$H_\theta^{in} = 0 \tag{2.67}$$
$$H_\varphi^{in} = \gamma P_\eta^{(1)}(-\cos(\alpha))P_\eta^{(1)}(\cos(\theta))r^\eta \tag{2.68}$$
$$\tag{2.69}$$

$$\begin{aligned}E_r^{in} = \frac{\gamma P_\eta^{(1)}(-\cos(\alpha))}{i\epsilon_1\omega\sin(\theta)}r^{\eta-1}&\left[\cos(\theta)P_\eta^{(1)}(\cos(\theta)) - \right.\\ &\left. - \sin^2\theta\frac{\partial P_\eta^{(1)}(\cos(\theta))}{\partial\cos(\theta)}\right]\end{aligned} \tag{2.70}$$

$$E_\theta^{in} = \frac{\gamma P_\eta^{(1)}(-\cos(\alpha))(\eta+1)}{i\epsilon_1\omega}r^{\eta-1}P_\eta^{(1)}(\cos(\theta)) \tag{2.71}$$
$$E_\varphi^{in} = 0 \tag{2.72}$$

Outside the cone:

$$H_r^{out} = 0 \tag{2.73}$$

$$H_\theta^{out} = 0 \tag{2.74}$$

$$H_\varphi^{out} = \gamma P_\eta^{(1)}(\cos(\alpha)) P_\eta^{(1)}(-\cos(\theta)) r^\eta \tag{2.75}$$

$$\tag{2.76}$$

$$\begin{aligned} E_r^{out} = & \frac{\gamma P_\eta^{(1)}(\cos(\alpha))}{i\epsilon_2 \omega \sin(\theta)} r^{\eta-1} \Bigg[\cos(\theta) P_\eta^{(1)}(-\cos(\theta)) - \\ & - \sin^2\theta \frac{\partial P_\eta^{(1)}(-\cos(\theta))}{\partial \cos(\theta)} \Bigg] \end{aligned} \tag{2.77}$$

$$E_\theta^{out} = \frac{\gamma P_\eta^{(1)}(\cos(\alpha))(\eta+1)}{i\epsilon_2 \omega} r^{\eta-1} P_\eta^{(1)}(-\cos(\theta)) \tag{2.78}$$

$$E_\varphi^{out} = 0 \tag{2.79}$$

2.3.3 Dispersion relations for the conical structure

Boundary conditions can be satisfied by a proper choice of the propagation parameter η. By introducing a new variable $\epsilon_{12} = \epsilon_1/\epsilon_2$, replacing $\cos(\alpha)$ by X and dividing Equation 2.64 by Equation 2.65, the following relation is obtained:

$$\frac{\partial P_\eta^{(1)}(X)}{\partial X} - \epsilon_{12} \frac{\partial P_\eta^{(1)}(-X)}{\partial X} = (1 - \epsilon_{12}) \frac{X P_\eta^{(1)}(X)}{1 - X^2} \tag{2.80}$$

The formula for the derivative of the Legendre function reported in Olver, Lozier, Boisvert, and Clark (2010) is:

$$\frac{\partial P_\eta^{(1)}(X)}{\partial X} = \frac{\eta P_{\eta+1}^{(1)}(X) - (1+\eta) X P_\eta^{(1)}(X)}{X^2 - 1} \tag{2.81}$$

Using the formula for the derivative of Legendre function Equation 2.81 and looking for nontrivial solutions of η, Equation 2.80 can be simplified:

$$X(\epsilon_{12} - 1) + \epsilon_{12} \frac{P_{\eta+1}^{(1)}(-X)}{P_\eta^{(1)}(-X)} + \frac{P_{\eta+1}^{(1)}(X)}{P_\eta^{(1)}(X)} = 0 \tag{2.82}$$

The equation (2.82) which has been obtained involves the frequency dependent permittivity of silicon dioxide and the propagation parameter η. The X is just a parameter of the cone geometry $X = \cos(\alpha)$, where α is the aperture angle of the cone. From now on, this Equation 2.82 is called the Dispersion Relation.

2.3.4 Limitations and meaning of the propagation parameter

Equation 2.82 has to be numerically solved in a complex domain for the propagation parameter η, provided that the permitivitties of the media and the aperture angle α of the cone, are known. The dispersion relation in Equation 2.82 generalizes the one derived by Babadjanyan *et al.* Babadjanyan, Margaryan, and Nerkararyan (2000) for cones of small aperture angle ($\sin(\alpha) \approx \alpha$). The physical meaning of the conical propagation parameter η can be easily understood by rewriting the magnetic field in Equation 2.68 with its harmonic oscillatory term, as follows

$$H_{\varphi}^{in}(r,\theta,t) = C(\theta) e^{\eta_i \ln(\sqrt{\epsilon_1} k_0 r)} e^{i(\omega t + \eta_r \ln(\sqrt{\epsilon_1} k_0 r))}, \tag{2.83}$$

where $C(\theta)$ stands for the term independent of the radius r. The phase velocity v_p of the field H_{φ}^{in} is defined by setting its phase to a constant, that is to say, $\omega t + \eta_r \ln(\sqrt{\epsilon_1} k_0 r) = constant$. Taking the time derivative of this expression and considering the time dependence of the SPhP position r, we obtain the following SPhP phase velocity

$$v_p = -\frac{\omega r}{\eta_r}, \tag{2.84}$$

which decreases as the SPhPs approach to the cone tip, and agrees with the results reported for the focusing of surface plasmon-polaritons Babadjanyan, Margaryan, and Nerkararyan (2000) Nerkararyan (1997) Kurihara, Otomo, Syouji, Takahara, Suzuki, and Yokoyama (2007) Kurihara, Yamamoto, Takahara, and Otomo (2008). Equation 2.84 establishes that the SPhP propagation towards the cone tip is guaranteed (phase velocity is negative), when the real part of η is positive:

$$\eta_r > 0. \tag{2.85}$$

Another constraint on the imaginary part of η can be found by considering the SPhP Poynting vector, defined by

$$\mathbf{S} = \frac{1}{2} \mathrm{Re}\left(\mathbf{E} \times \mathbf{H}^*\right), \tag{2.86}$$

where $\mathbf{H}^*$ is the complex conjugate of $\mathbf{H}$. Based on Equations 2.66-2.72 and 2.86, the radial component S_r^{in} of $\mathbf{S}$ inside the cone is found to be

$$S_r^{in} = \frac{1}{2} \mathrm{Re}\left(\frac{i\eta + 1}{i\epsilon_1 \omega}\right) \left| B P_{i\eta}^{(1)}(\cos(\theta)) \right|^2 r^{2\eta_i - 1}. \tag{2.87}$$

Equation (2.87) shows that the radial component of the SPhP Poynting vector increases as they approach towards the cone tip, provided that the imaginary part of η satisfies the following condition:

$$0 < \eta_i < 0.5, \tag{2.88}$$

where the upper bound is imposed to guarantee the finiteness of S_r^{in}, as r increases. Equations (2.87) and (2.88) indicate that the focusing of SPhP energy density can be maximized by minimizing the imaginary part η_i of the propagation parameter. This is the reason why from all possible solutions supported by the dispersion relation in Equation 2.82, for a given set of permittivities and aperture angles, only those with the smallest η_i satisfying Equation 2.88, are going to be considered in this work. Note that according to Equations 2.66-2.72, 2.87, and 2.88; the two components of the electrical field and the Poynting vector diverge at the cone tip. This behavior is reasonable due to the reduction of the cross-section area of the cone as the SPhPs travel towards its tip. The SPhP power P_c is defined by the integral of the Poynting vector over the cross section A of the cone, as follows: $P_c = \int S_r^{in} \cos(\theta) dA$, with $dA = r\sin(\theta) d\left(r\sin(\theta)\right) d\varphi$. The illustration of this integration is shown on Figure 2.4.

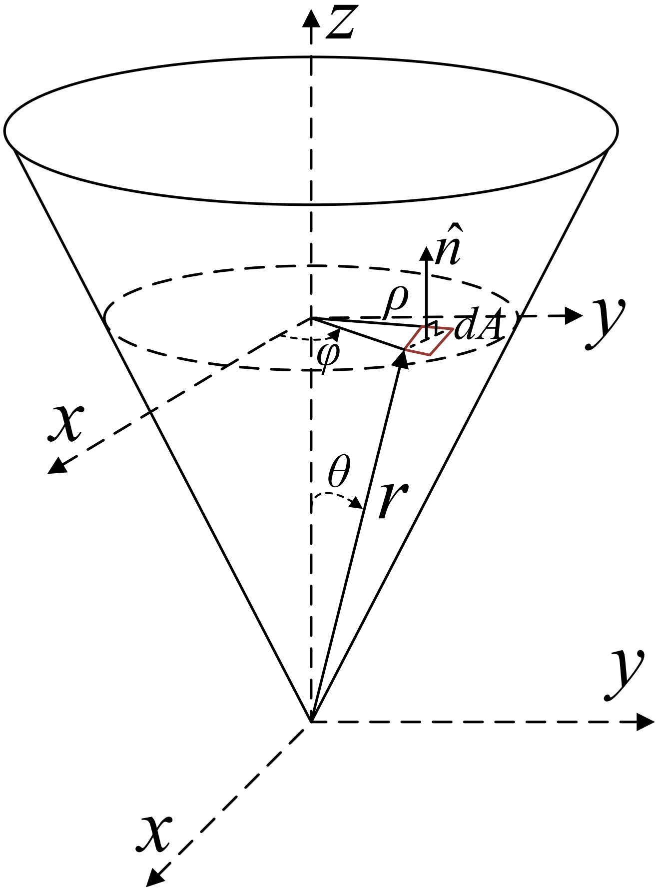

Figure 2.4: *Scheme of the cone illustrating the integration.*

The combination of this expression with Equation 2.87 yields

$$P_c \sim r^{2\eta_i}, \tag{2.89}$$

which establishes that the SPhP power transmitted through the cone, in contrast to the Poynting vector S_r^{in}, decreases as the SPhPs propagate towards its tip. This is expected due to the absorption of energy by the SiO_2 cone and it is in agreement with the principle of energy conservation. Given that real conical structures have a finite radius of curvature, $r > 0$ and therefore the SPhP power is always greater than zero at the cone tip.
The focusing efficiency can be characterized by introducing the Focusing Factor F_c as the ratio between the SPhP power and its own value at a certain fixed distance from the tip (e.g. $r_0 = 100$ nm)

$$F_C(r) = \frac{S_r(r)}{S_r(r_0)} = \left(\frac{r}{r_0}\right)^{2\eta_i - 1}. \tag{2.90}$$

This dimensionless factor, which is independent of the angular variable and of the excitation source, indicates that the relative enhancement of Poynting vector of the SPhPs propagating towards the cone tip is totally determined by the imaginary part η_i of the propagation parameter, for a given cone material and aperture angle.

2.4 Numerical solution of the amorphous glass cone Disperison Relation

2.4.1 Numerical methods

In this section, we analyze the SPhP propagation features predicted by the dispersion relations for the cone Equation 2.82. This relation is solved by means of the Newton's method in the complex plane, to find the complex values of the propagation parameters η, as a function of the excitation frequency and aperture angle of a SiO_2 structure surrounded by air ($\varepsilon_2 = 1$). The relative permittivity ε_1 of SiO_2 has been obtained from the values of the refractive index reported in the literature, Palik (1985) and its real and imaginary parts are shown on Figure 2.5. These values of the permittivity are expected to be valid in SiO_2 objects with sizes equal or greater than 5 nm Chalopin, Dammak, Hayoun, Besbes, and Greffet (2012). By implementing the routine of this method with the software Mathematica 9 and imposing the physical limitations on the real and imaginary parts of η according to Equations 2.85 and 2.88, the following range $0 < \eta_r < 3$, $0 < \eta_i < 3$ has been properly chosen to make sure that all the relevant roots for the parameter components η_r and η_i are contained within these intervals.

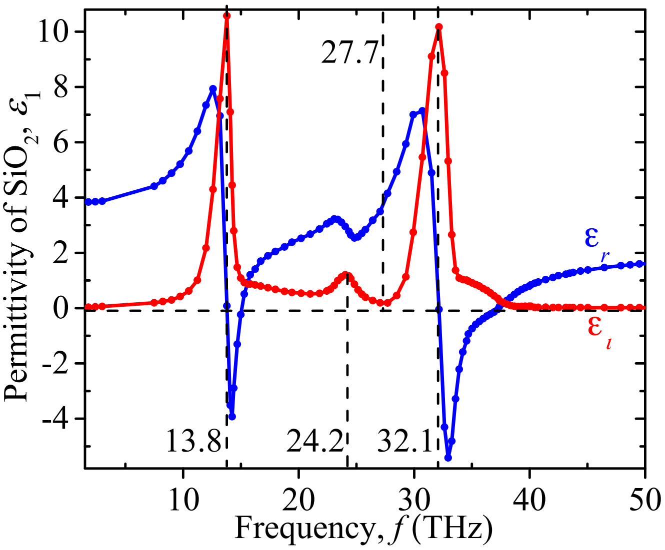

Figure 2.5: *Real and imaginary parts of the relative permittivity* $\epsilon(f) = \epsilon_r(f) - i\epsilon_i(f)$ *of* SiO_2*, as a function of frequency* $f = \omega/2\pi$*. The results are obtained from analyzing the experimental data reported by Palik Palik (1985).*

In each of these domains, 10^4 uniformly placed points have been taken to specify the first guess value for the Newton's method. Even though we cannot exclude the presence of additional roots in a wider interval, their contribution to the electrical and magnetic fields, as well as to the Poynting vector are going to be relatively small, as established by Equations 2.66-2.72, 2.87. Roots with smaller imaginary part provide higher fields. From the set of roots, the one with the smallest imaginary part of the propagation parameter η has been selected. This procedure allows us to account for the root with the most significant contribution to the focusing of the SPhP energy density.
Also note, that we use here frequency $f = \omega/2\pi$ in THz units in order to make our results clear for both theoreticians and experimentators.

2.4.2 Results

The real and imaginary parts of the conical propagation parameter $\eta = \eta_r - i\eta_i$, as a function of the excitation frequency, are shown in Fig. 2.6, for two different aperture angles of the cone. While η_r takes positive values in all the frequency range, the imaginary part η_i satisfies the condition in Equation 2.88 only in two frequency ranges. Note that η_i takes its smaller values in the interval from 32.1 THz to 33.9 THz. Within this frequency range, the real part ϵ_r of the SiO_2 permittivity takes its larger negative values as shown on Figure 2.5, and the material is able to effectively support the propagation of SPhPs Ordonez-Miranda, Tranchant, Tokunaga, Kim, Palpant, Chalopin, Antoni, and Volz (2013) Ordonez-Miranda, Tranchant, Kim, Chalopin, Antoni, and Volz (2014a)

Ordonez-Miranda, Tranchant, Kim, Chalopin, Antoni, and Volz (2014b). For both angles, η_i reaches its minimum value of about $\eta_i = 0.036$, at the critical frequency $f_{\text{cr}} = 33.6$ THz, which corresponds to the strongest SPhP focusing.

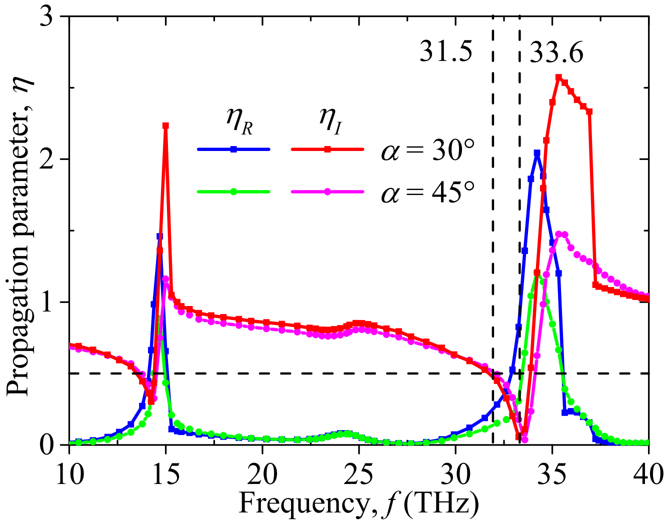

Figure 2.6: *Real and imaginary parts of the SPhP propagation parameter* $\eta = \eta_r - i\eta_i$ *along a cone, as a function of excitation frequency and for two aperture angles* α. *The SPhP focusing occurs within the frequency ranges in which* $\eta_i < 0.5$.

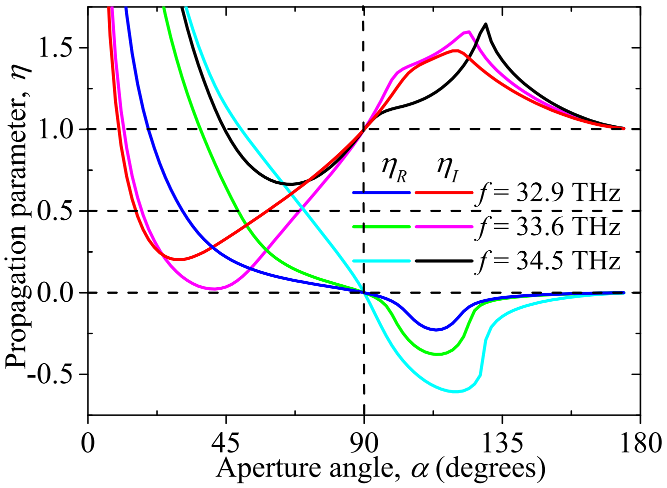

Figure 2.7: *Real and imaginary parts of the SPhP propagation parameter* $\eta = \eta_r - i\eta_i$ *for the cone, as a function of aperture angle and for three excitation frequencies* $f = \omega/2\pi$. *The SPhP focusing occurs within the angle ranges in which* $\eta_i < 0.5$.

Figure 2.7 shows the behavior of the two components of the propagation parameter η, as a function of the aperture angle α of the cone. Note that the minima of η_i depends drastically on the excitation frequency and it takes its absolute minimum at the critical frequency $f_{\mathrm{cr}} = 33.6$ THz and an aperture angle around $\alpha_{\mathrm{opt}} = 45°$, which agrees with Fig. 2.6. This angle represents the optimal configuration for maximizing the SPP focusing in a $\mathrm{SiO_2}$ cone. The conical structure can also support the SPhP focusing for other aperture angles within the interval of 18° to 68°, in which the focusing conditions in Equations 2.85 and 2.88 are fulfilled. The interval of 90° to 180° corresponds to the reverse case, where the air cone embedded in $\mathrm{SiO_2}$ is considered. For this interval of aperture angles, there are no propagation parameters η satisfying the focusing conditions in Equations 2.85 and 2.88, which means that the focusing of SPhPs with an air cone embedded in $\mathrm{SiO_2}$ is not possible.

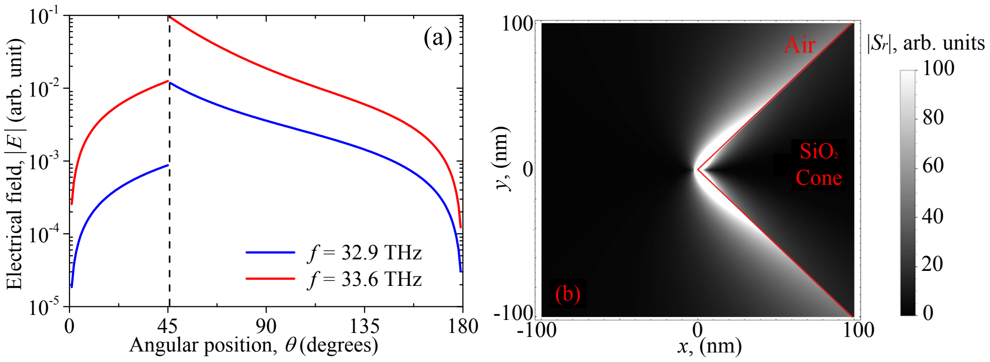

Figure 2.8: *(a) Total electrical field at $r_0 = 100$ nm and (b) Poynting vector map in the conical structure. Calculations were performed for the critical frequency $f_{cr} = 33.6$ THz and the optimum aperture angle of $\alpha_{opt} = 45°$ approximately. Brighter regions correspond to larger values of the Poynting vector.*

The magnitude of the electrical field obtained with the values of the propagation parameter η shown in Figures 2.6 and 2.7, is shown on Figure 2.8(a). The jump at the cone interface $\theta = 45°$ is due to the discontinuity of the component E_θ of the electrical field, and its intensity is higher outside the cone, due to the absence of absorption in the surrounding air. Furthermore, the field intensity decreases as it travels away from the interface and it becomes negligible at the axes of symmetry $\theta = 0°$ (inside the cone) and $\theta = 180°$ (outside the cone). This indicates the presence of SPhPs traveling along the interface of the cone and it is confirmed by the distribution of the Poynting vector shown on Figure 2.8(b). The energy flux propagates in the air just outside the cone interface, it increases as it approaches to the cone tip, and therefore it supports the focusing of SPhPs traveling towards the tip.

Figure 2.9 shows the angular dependence of the SPP focusing factor (F_c) of the cone, for three excitation frequencies and at $r = 5$ nm from the tip. The focusing of the SPP energy density occurs only for $F_c > 1$. For the optimum aperture angle around $\alpha_{\mathrm{opt}} = 45°$ and the critical excitation frequency $f_{\mathrm{cr}} = 33.6$ THz, the largest value of F_c is 12. This indicates that when the SPhPs travels from $r = 100$ nm to $r = 5$ nm, their Poynting vector increases by a factor of 12.

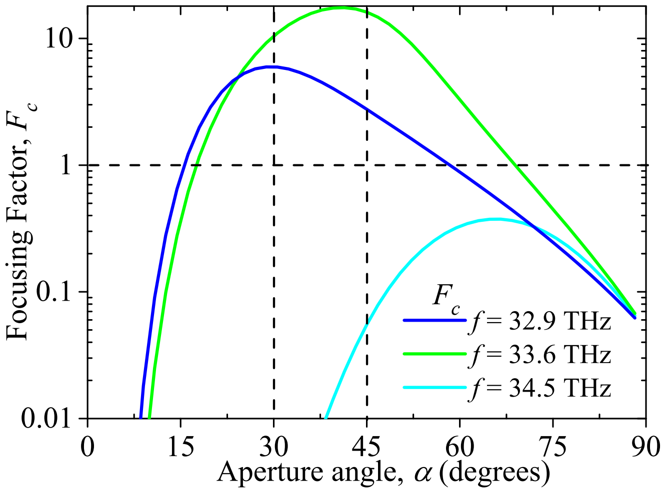

Figure 2.9: *Focusing factor of the conical structure as a function of its aperture angle* α*, for three excitation frequencies* f*. Calculations were done for* $r = 5$ *nm and* $r_0 = 100$ *nm.*

2.5 Conclusions

The focusing of surface phonon-polaritons (SPhPs) along a SiO_2 cone has been analyzed. Based on Maxwell's equations, explicit expressions for the dispersion relation has been determined and solved numerically for a propagation parameter that controls the propagation of SPhPs. For conical structures of SiO_2, it has been shown that: the cone supports the SPhP focusing only for aperture angles in the interval 18° - 68°, and within the range of excitation frequencies from 32.1 THz to 33.9 THz. This is a an interesting finding as the optimization of the geometry should be done in order to find the optimum aperture angles of the cone of a certain material. The SPhP focusing efficiency of the cone reaches its maximum values at the critical frequency $f_{\text{cr}} = 33.6$ THz and different aperture angles of about $\alpha_{\text{opt}} = 45°$. When the SPhPs travel from 100 nm to 5 nm toward the tip of the cone with this optimum angle, their Poynting vector increases by a factor of twelve, which should provide an efficient way of focusing of thermal energy. Our results on the cone represent an upper estimation of the SPhP focusing, due to the ideal sharp tip. The finite radius of curvature of the tip of real cones is expected to avoid the divergent behavior of the electrical fields and to decrease the obtained focusing efficiency. We believe that these results can have a significant impact on improving near-field infrared microscopy, efficient heat extraction from nanodevices, and near-field radiation.

Chapter 3

Focusing with Wedge Glass Structures

In this chapter, we demonstrate the possibility of thermal energy focusing using the concept of surface phonon-polariton concentration with a 2D structure based on wedge geometry. We used amorphous glass as a material for our theoretical study in order to compare the efficiency of focusing with conical glass structure considered in the previous chapter. These results have been reported in our article Gluchko, Ordonez-Miranda, Tranchant, Antoni, and Volz (2015).

3.1 Introduction

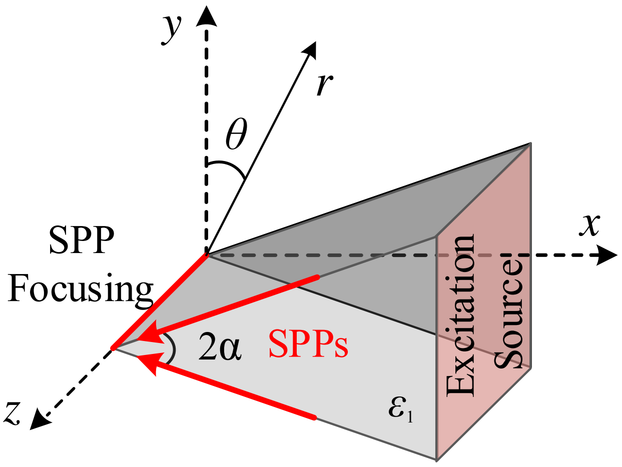

Figure 3.1: *Cylindrical coordinates used to build the theoretical model of SPhP focusing in conical structures.*

The concept of heat focusing using surface phonon-polariton concentration with tip effect can be translated into a two dimensional topology by considering a

wedge, with infinite size in the lateral z axis direction as shown on Figure 3.1. The idea of SPhP concentration with wedge structures is very similar to the one described in the Chapter 2 when we considered a glass conical structure. By heating a cross section of the wedge (see pink area on Figure 3.1), the thermal energy is coupled with the hybrid electromagnetic surface modes (SPhPs) and propagates along the interfaces of the wedge, and concentrates on its edge. One should notice that the focusing of thermal energy should be observed along the line of the wedge edge while the conical structure concentrates energy at one point. Such a significant topological difference between these two structures is an important signature that wedge geometry should support less efficient SPhP concentration due to the dispersion of the same flux over a larger surface area. However, modern applications often requires 2D concentration of thermal energy especially in nano- and micro-electronics and heat management.
In this chapter we use the results obtained in the Chapter 2 and skip certain mathematical derivations.

3.2 Dispersion relation of the wedge structure

Here we work again in the conventions where the relative dielectric constant of the material is complex:

$$\epsilon = \epsilon_r - i\epsilon_i. \tag{3.1}$$

The wavevector is also complex and the frequency is real.

3.2.1 TM-polarization in cylindrical coordinates

Similarly to section 2.2.2, we will only consider TM-polarization of the field but in the cylindrical coordinates as shown on Figure 3.1. The choice of the cylindrical coordinates is convenient due to the symmetry of the wedge geometry.

$$r = \sqrt{x^2 + y^2} \tag{3.2}$$

$$\theta = \arctan\left(\frac{x}{y}\right) \tag{3.3}$$

$$z = z. \tag{3.4}$$

The TE polarization should not contribute to the surface modes energy transport due to the symmetry of the geometry. We also consider the excitation of the cross section area of the wedge to be uniform in z direction:

$$\mathbf{E} = \mathbf{E}(r, \theta) \tag{3.5}$$

$$\mathbf{H} = \mathbf{H}(r, \theta). \tag{3.6}$$

In this case Equations

$$\left(\boldsymbol{\nabla}^2 + \mu\epsilon {k_0}^2\right)\mathbf{E} = \mathbf{0} \tag{3.7}$$
$$\left(\boldsymbol{\nabla}^2 + \mu\epsilon {k_0}^2\right)\mathbf{H} = \mathbf{0} \tag{3.8}$$

should be written as follows:

$$\left(\nabla^2 + \mu\epsilon {k_0}^2\right) H_z = 0, \tag{3.9a}$$
$$i\epsilon\omega E_r = \frac{1}{r}\frac{\partial H_z}{\partial \theta}, \tag{3.9b}$$
$$i\epsilon\omega E_\theta = -\frac{\partial H_z}{\partial r}. \tag{3.9c}$$

By applying the standard assumption that the magnetic field H_z can be considered as the product of two components each depending only of one variable:

$$H_z(r,\theta) = R(r)T(\theta) \tag{3.10}$$

one can use the method of separation of variables to end up with explicit equations for all the components of the electromagnetic field inside the wedge:

$$H_z^{in} = a(\lambda)r^{i\lambda}\cosh(\lambda(\theta-\alpha)), \tag{3.11a}$$
$$E_r^{in} = \frac{a(\lambda)r^{i\lambda-1}}{i\epsilon_1\omega}\sinh(\lambda(\theta-\alpha)), \tag{3.11b}$$
$$E_\theta^{in} = \frac{-a(\lambda)r^{i\lambda-1}}{i\epsilon_1\omega}\cosh(\lambda(\theta-\alpha)), \tag{3.11c}$$

and outside the wedge:

$$H_z^{out} = b(\lambda)r^{i\lambda}\cosh(\lambda(\theta-\alpha-\pi)), \tag{3.12a}$$
$$E_r^{out} = \frac{b(\lambda)r^{i\lambda-1}}{i\epsilon_2\omega}\sinh(\lambda(\theta-\alpha-\pi)), \tag{3.12b}$$
$$E_\theta^{out} = \frac{-b(\lambda)r^{i\lambda-1}}{i\epsilon_2\omega}\cosh(\lambda(\theta-\alpha-\pi)), \tag{3.12c}$$

where a and b are constants that depend on the boundary conditions, $\lambda = \lambda_r - i\lambda_i$ is the SPhP propagation parameter of the wedge (similar to the one of the cone in the previous chapter), and α is the half-aperture angle of the wedge. The direct application of the standard boundary conditions at the wedge interfaces (for $\theta = \pm\alpha$)

$$H_z^{in} = H_z^{out}, \tag{3.13a}$$
$$E_r^{in} = E_r^{out}, \tag{3.13b}$$

yields the following dispersion relation for the propagation of SPhPs towards the wedge edge

$$\tanh(\lambda(\pi - \alpha)) - \epsilon_{12}\tanh(\lambda\alpha) = 0, \tag{3.14}$$

where $\epsilon_{12} = \epsilon_1/\epsilon_2$. Equation (3.14) generalizes the dispersion relation derived by Nerkararyan *et al.* Nerkararyan (1997) for wedges of small aperture angle ($\alpha \ll \pi$ rad) and is valid for any half-aperture angle of the wedge α.

3.2.2 Limitations and meaning of the wedge propagation parameter

The dispersion relation of the wedge in Equation 3.14 links the complex propagation parameter of the cone λ with the complex dielectric function of the wedge which itself depends on frequency. In order to understand the meaning of the propagation parameter, the explicit equation of the magnetic field provided by the Equation 3.11a should be rewritten with its harmonic oscillatory term in the following form:

$$H_z^{in}(r,\theta,t) = C(\theta)e^{\lambda_i \ln(\sqrt{\epsilon_1}k_0 r)}e^{i(\omega t + \lambda_r \ln(\sqrt{\epsilon_1}k_0 r))}, \tag{3.15}$$

where $C(\theta)$ stands for the term independent of the radius r. The phase velocity v_p of the field H_{in} is defined by setting its phase to a constant, that is to say, $\omega t + \lambda_r \ln(\sqrt{\epsilon_1}k_0 r) = constant$. Taking the time derivative of this expression and considering the time dependence of the SPhP position r, we obtain the following SPhP phase velocity

$$v_p = -\frac{\omega r}{\lambda_r}, \tag{3.16}$$

which decreases as the SPhPs approach the wedge edge. Equation 3.16 establishes that the SPhP propagation towards the cone tip is guaranteed (phase velocity is negative), when the real part of λ is positive:

$$\lambda_r > 0. \tag{3.17}$$

Another constraint on the imaginary part of λ can be found by considering the SPhP Poynting vector, defined by

$$\mathbf{S} = \frac{1}{2}\mathrm{Re}\left(\mathbf{E} \times \mathbf{H}^*\right), \tag{3.18}$$

where $\mathbf{H}^*$ is the complex conjugate of $\mathbf{H}$. Based on Equations 3.11a-3.11c and Equation 3.18, one can calculate the power SPhP power P_w propagating along the radial direction of the wedge per unit of edge length L defined as integral integral of the Poynting vector over its cross section:

$$\frac{P_w}{L} = \frac{1}{L}\int \mathbf{S}^{in} \cdot \mathbf{n} dA = r \int S_r^{in}(r,\theta)\cos(\theta) d\theta \sim r^{2\lambda_i}. \tag{3.19}$$

The integration procedure is demonstrated on Figure 3.2.
Equation 3.19 shows that the radial components of the SPhP Poynting vector increases as they approach towards the wedge edge, provided that the imaginary part of λ satisfies the following condition:

$$0 < \lambda_i < 0.5, \tag{3.20}$$

where the upper bound is imposed to guarantee a finite S_r^{in}, as r increases. Equations 3.19 and 3.20 indicate that the focusing of SPhP energy density can be maximized by minimizing the imaginary part λ_i of the propagation parameter. This is the reason why from all possible solutions supported by the dispersion relation in Equation 3.14, for a given set of permittivities and aperture angles, only those with the smallest λ_i satisfying Equation 3.20, are going to be considered in this work. Note that according to Equations 3.11a-3.11c, 3.19, and 3.20, the two components of the electrical field and the Poynting vector diverge at the wedge edge. This behavior is reasonable due to the reduction of the cross-section area of the cone as the SPhPs travel towards its edge.

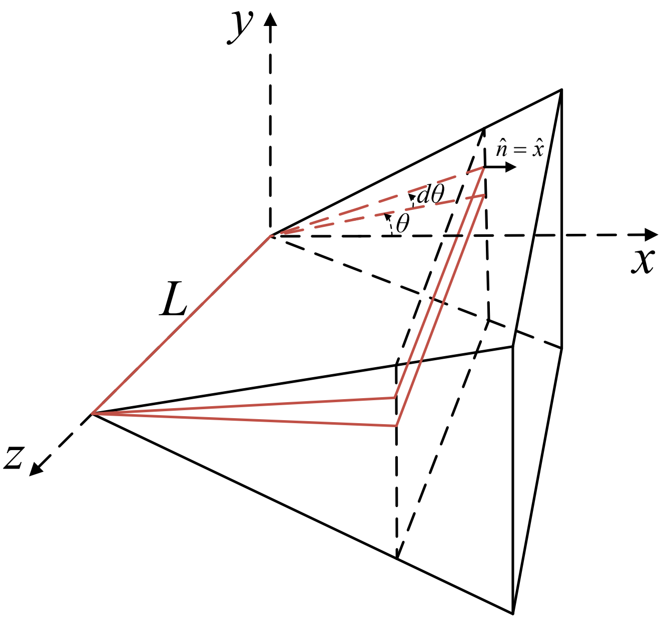

Figure 3.2: *Scheme illustrating the integration in the wedge structure.*

Note that, for the wedge structure, the real part λ_r of the propagation parameter is inversely proportional to the phase velocity, while the imaginary part

λ_i controls the focusing of the field. Furthermore, the mode with the smallest imaginary part λ_i has the strongest contribution to the total Poynting vector of SPhPs traveling towards the wedge edge.
By analogy with the conical structure and for purposes of comparison, we define the wedge Focusing Factor as follows:

$$F_w(r) = \frac{S_r(r,\theta)}{S_r(r_0,\theta)} = \left(\frac{r}{r_0}\right)^{2\lambda_i - 1}, \tag{3.21}$$

which depends only on the imaginary part of the propagation parameter and allows us to compare the focusing efficiency of the wedge with that of the cone. In the case of the wedge, the normalization for the focusing factor is chosen in exactly the same way as for the cone in the Chapter 2, such as $r_0 = 5$ nm. The structure with larger focusing factor is able to concentrate a higher energy density flux.

3.3 Numerical solution of the amorphous glass wedge Dispersion Relation

3.3.1 Numerical methods

In this section, we analyze the SPhP propagation features predicted by the dispersion relations for the wedge Equation 3.14. This relation is solved by means of the Newton's method in the complex plane, to find the complex values of the propagation parameters λ, as a function of the excitation frequency and aperture angle of a SiO_2 structure surrounded by air ($\varepsilon_2 = 1$) similar to the one used for the conical geometry. The relative permittivity ε_1 of SiO_2 has been obtained from the values of the refractive index reported in the literature, Palik (1985). By implementing the routine of this method with the software Mathematica 9 and imposing the physical limitations on the real and imaginary parts of λ according to Equations 3.17 and 3.20, the following range $0 < \lambda_r < 3$, $0 < \lambda_i < 3$ has been properly chosen to make sure that all the relevant roots for the parameter components λ_r and λ_i are contained within these intervals.
In each of these domains, 10^4 uniformly placed points have been taken to specify the first guess value for the Newton's method. Even though we cannot exclude the presence of additional roots in a wider interval, their contribution to the electrical and magnetic fields, as well as to the Poynting vector are going to be relatively small, as established by Equations 3.11a-3.11c. Roots with smaller imaginary part provide higher fields. From the set of roots, the one with the smallest imaginary part of the propagation parameter λ has been selected. This procedure allows us to account for the roots, with the most significant contribution to the focusing of the SPhP energy density.

3.3.2 Results

Figures 3.3(a) and 3.3(b) show the numerical solutions of the SPhP dispersion relation for the propagation parameter λ, as a function of the excitation frequency and aperture angle of the wedge, respectively. Similar to the case of the cone, we can see that the SPhP focusing conditions in Equations 3.17 and 3.20 are satisfied only in the frequency range from 32.9 THz to 33.9 THz and aperture angles between 21° and 51°. The imaginary part of the propagation parameter takes its minimal value $\lambda_i = 0.31$, at the critical frequency $f_{cr} = 33.6$ THz and optimum aperture angle $\alpha_{\text{opt}} = 30°$, which is smaller than the corresponding one for the cone. For this frequency and aperture angle, the SPhP focusing is optimal. Note also that there is no SPhP focusing along an air wedge embedded in SiO_2, due to the fact that conditions in Equations 3.17 and 3.20 are not satisfied for aperture angles larger than 90° or frequencies higher than 33.9 THz (such as $f = 34.5$ THz).

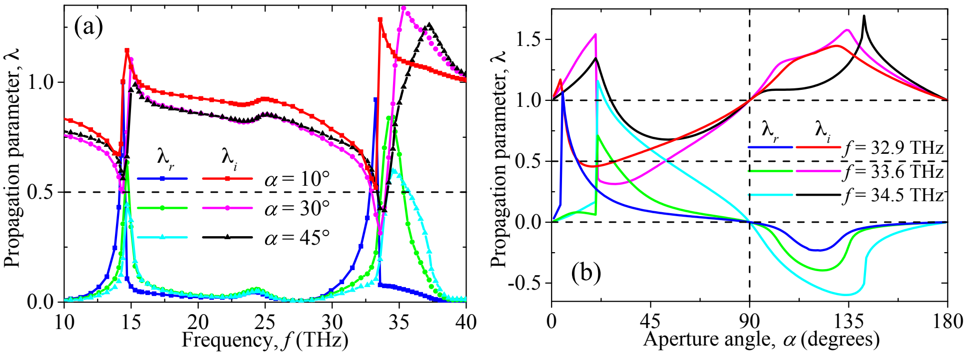

Figure 3.3: *Real and imaginary parts of the SPhP propagation parameter* $\lambda = \lambda_r - i\lambda_i$ *of the wedge, as a function of the (a) excitation frequency* $f = \omega/2\pi$ *and (b) aperture angle* α. *The SPhP focusing occurs for frequencies and angles in which* $\lambda_i < 0.5$.

The magnitude of the electrical field along with the density map of the Poynting vector in the wedge are shown in Figures 3.4(a) and 3.4(b), respectively. Both the electrical field and the Poynting vector are concentrated at the outer border of the wedge-air interface close to the wedge tip, as expected. The behavior becomes particularly strong at the critical frequency $f_{\text{cr}} = 33.6$ THz and optimum aperture angle $\alpha_{\text{opt}} = 30°$, which is consistent with Figures 3.3(a) and 3.3(b) and it indicates that the Poynting vector of SPhPs can be maximized with this set of physical parameters. The SPhP focusing factor F_w of this Poynting vector is shown in Figure 3.5. This focusing efficiency of the wedge takes its larger values at the critical frequency and the optimum aperture angle, such that $F_w = 3$ at the distance $r = 5$ nm. This value of F_w is about four times smaller than that of the cone, showing that the SPhP focusing efficiency of the cone is significantly higher than the one of the wedge.

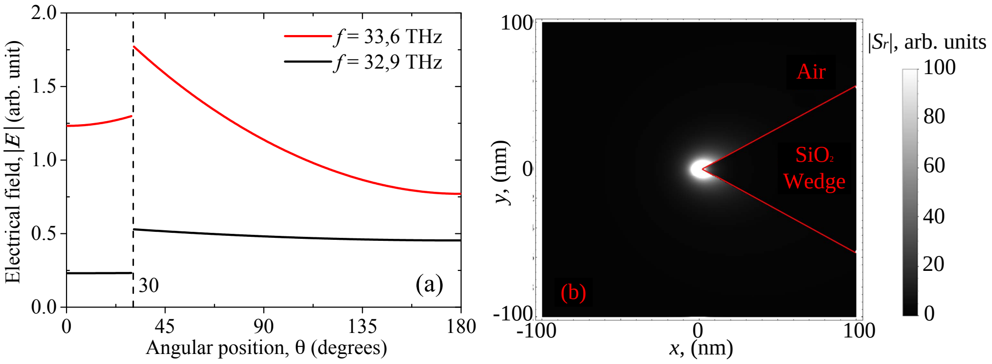

Figure 3.4: *(a) Total electrical field at* $r_0 = 100$ *nm and (b) Poynting vector density map in the wedge structure. Calculations were performed for the critical frequency* $f_{cr} = 33.6$ *THz and optimum aperture angle* $\alpha_{opt} = 30°$*. Brighter regions correspond to larger values of the Poynting vector.*

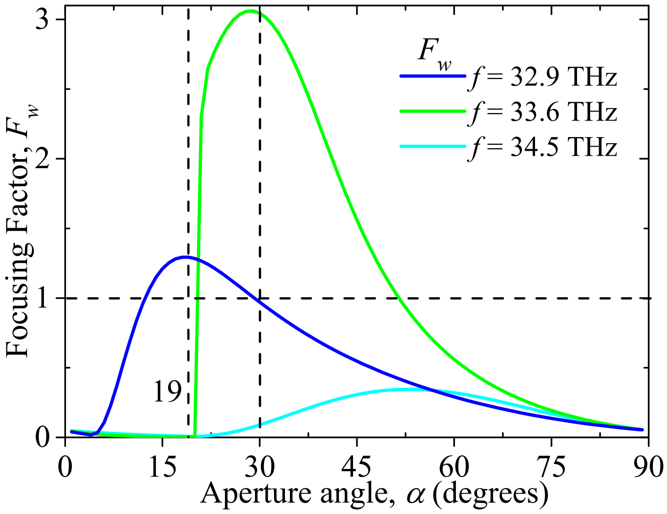

Figure 3.5: *Focusing factor of the wedge as a function of its aperture angle* α*, for three excitation frequencies* f*. Calculations were done for* $r = 5$ *nm and* $r_0 = 100$ *nm.*

3.4 Conclusions

The focusing of surface phonon-polaritons (SPhPs) along a wedge has been analyzed. Based on Maxwell's equations, explicit expressions for the dispersion relation have been determined and solved numerically for a propagation parameter that controls the propagation of SPhPs. For wedge structure of SiO_2, it has been shown that: it supports the SPhP focusing only for aperture angles in the interval 21° - 51°, and within the range of excitation frequencies from 31.5 THz to 33.9 THz. The SPhP focusing efficiency of wedge reaches its maximum values at the critical frequency $f_{\mathrm{cr}} = 33.6$ THz and aperture angles of about

$\alpha_{\text{opt}} = 30°$. When the SPhPs travel from 100 nm to 5 nm toward the edge of the wedge with this optimum angle, their Poynting vector increases by a factor of three, which is about four times smaller than the corresponding one provided by the conical glass structure. Our results for the wedge represent an upper estimation of the SPhP focusing, due to its ideal sharp edge. The finite radius of curvature of the edge of real wedges is expected to avoid the divergent behavior of the electrical fields and to decrease the obtained focusing efficiency. The fact that the wedge is a less efficient focusing structure than cone is intuitively clear. However, we have demonstrated this theoretically and introduced the Focusing Factor which gives a clear numerical comparison of different focusing structures. Our approach is general and can be used for any material and geometry.

Chapter 4

Superfocalisation of Infrared Electromagnetic Radiation in Far Field

In this chapter, we demonstrate that electromagnetic long range surface modes (including surface phonon-polaritons) can be used to significantly decrease the diffraction angles of the infrared radiation on a rectangular or a circular sub-wavelength aperture. We used a structure that was formed of two thin dielectric membranes (e.g. amorphous glass) to demonstrate significantly smaller diffraction angles than in the case of an infinite slit. The results are obtained by means of Finite-Difference Time-Domain numerical simulations performed for different parameters of the system.

4.1 Introduction to Diffraction Problem

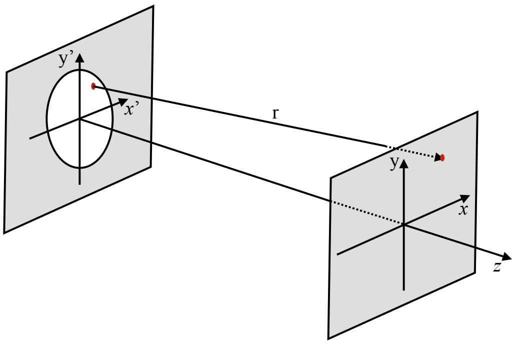

Figure 4.1: *Illustration of aperture plane and the diffraction pattern plane.*

Here we want to define the diffraction pattern produced as a result of the diffraction of a monochromatic plane wave by an aperture. So, let us consider

an aperture in the plane (x', y') at $z = 0$ and the diffraction pattern at certain distance far from the aperture in the (x, y) plane. The illustration of the system is shown on Figure 4.1.
This is a common physical problem that appears in various applications and is discussed in details in textbooks. For example, it can be found in the book by Max and Emil (2002). The diffracted electrical field E at a point (x, y, z) is given in the form of:

$$E(x,y,z) = \frac{1}{i\lambda} \iint E(x',y',0) \frac{e^{ikr}}{r}\, dx'\, dy', \tag{4.1}$$

where r is defined as:

$$r = \sqrt{(x-x')^2 + (y-y')^2 + z^2}, \tag{4.2}$$

In principle, Equation 4.1 should provide a solution for any shape of the aperture at any distances from the screen. However, this integral cannot be calculated analytically due to the term given by Equation 4.2 and approximations should be used in order to obtain analytical expressions for the diffracted field. Let us introduce the quantity:

$$\rho^2 = \left(x-x'\right)^2 + \left(y-y'\right)^2, \tag{4.3}$$

substituting it into Equation 4.2 we obtain

$$r = z\sqrt{1 + \frac{\rho^2}{z^2}}. \tag{4.4}$$

Now we can apply Taylor series expansion:

$$r = z + \frac{\rho^2}{2z} - \frac{\rho^4}{8z^3} + ... \tag{4.5}$$

Considering only the first two terms, we can end up with the Fresnel approximation of the diffraction:

$$r \approx z + \frac{\rho^2}{2z} = z + \frac{(x-x')^2 + (y-y')^2}{2z}, \tag{4.6}$$

and the Equation 4.1 for the Fresnel diffraction should be written as follows:

$$E(x,y,z) = \frac{e^{ikz}}{i\lambda z} \iint E(x',y',0) e^{\frac{ik\left[(x-x')^2 + (y-y')^2\right]}{2z}}\, dx'\, dy'. \tag{4.7}$$

The equation above is valid as long as

$$\frac{\rho}{z} \sim 1. \tag{4.8}$$

We can of course neglect the second term in Equation 4.5, assuming that

$$\frac{d^2}{z\lambda} \ll 1, \tag{4.9}$$

where d is a typical size of the diffraction object, and λ is the wavelength of the light. This approximation is known as the Fraunhofer integral of diffraction and is given as follows:

$$E(x, y, z) = \frac{1}{i\lambda} \iint E(x', y', 0) \frac{e^{ikz}}{z}\, dx'\, dy'. \tag{4.10}$$

4.1.1 Fraunhofer diffraction by a rectangular aperture

Applying the formalism demonstrated above, we can solve analytically the problem of a diffraction pattern of a plane monochromatic wave emitted by a rectangular aperture with a width b and a height d as shown on Figure 4.2.

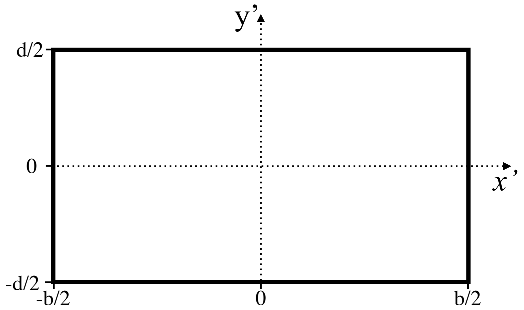

Figure 4.2: *Illustration of a rectangular aperture used for the calculation of the diffraction pattern.*

We use a Cartesian coordinate system with the origin at the center of the aperture. In this case, applying Equation 4.10, Fraunhofer diffraction can be calculated as:

$$E(x, y, z) = C \int_{-b/2}^{b/2} e^{-ikxx'}\, dx' \int_{-d/2}^{d/2} e^{-ikyy'}\, dy', \tag{4.11}$$

where C is a constant that can be later defined. The integral in Equation 4.11 can be calculated as follows:

$$\int_{-b/2}^{b/2} e^{-ikxx'}\, dx' = -\frac{1}{ikx}\left[e^{-ikx0.5b} - e^{ikx0.5b}\right] = 2\frac{\sin 0.5kbx}{kx}. \tag{4.12}$$

The intensity of the electromagnetic field is given by:

$$I(x,y,z) = \left|E(x,y,z)^2\right| = I_0 \left(\frac{\sin 0.5kbx}{0.5kbx}\right)^2 \left(\frac{\sin 0.5kdy}{0.5kdy}\right)^2, \tag{4.13}$$

where we introduced a new constant $I_0 = E_{\text{inc}}bd/\lambda^2$ being the intensity in the middle of the diffraction pattern, where E_{inc} is the total incident energy upon the aperture.

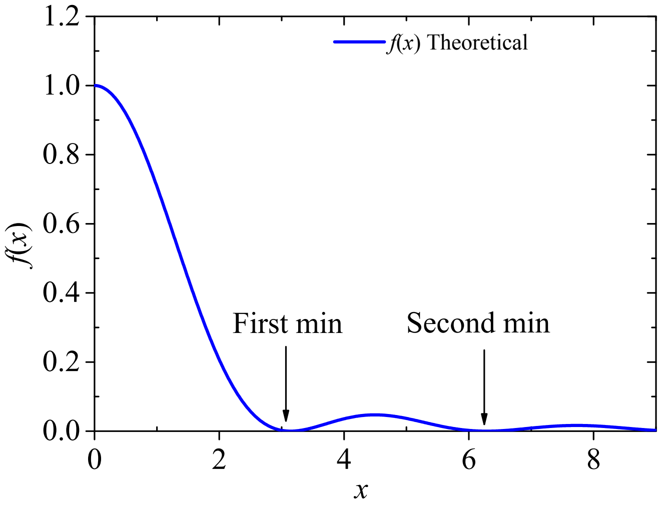

Figure 4.3: *Theoretically calculated plot of a function $f(x) = (sinx/x)^2$. It represents a typical intensity profile of the diffraction pattern from a rectangular aperture. Black arrows indicate the first and second minima of the function.*

Figure 4.3 shows the profile of the function $f(x) = (\sin x/x)^2$. This is the typical intensity profile provided by a diffraction of a plane wave on an infinite slit (one dimensional rectangular aperture). We should always observe a maximum in the middle of the pattern. The intensity decreases while going to the side from the center and reaches its minimum when $x = \pi$. Usually the angle between the central maximum and the first minimum is defined as the diffraction angle. In the case of a one-dimensional slit of width d the diffraction angle α can be calculated as:

$$\alpha = \frac{\lambda}{d}. \tag{4.14}$$

For example, the angle between central maximum and first minimum of diffraction pattern provided by a slit of $d = 21$ μm width for a plane monochromatic wave with wavelength of $\lambda = 10.9$ μm is $\alpha = 29.7°$. We will use these theoretical results later to compare with numerical simulations.

4.1.2 Fraunhofer diffraction by a circular aperture

In fact, in most of the applications that we need to consider the diffraction on circular apertures. Let us now calculate the Fraunhofer diffraction of a plane monochromatic wave on a circular aperture of radius a. In the case of a circular aperture, it is convenient to use cylindrical coordinates (ρ', θ', z) such that z is normal to the plane of the aperture. ρ' and θ' are in the plane of the aperture, while ρ and θ are in the diffraction pattern plane similar to the planes of (x', y') and (x, y) for a rectangular aperture discussed above. In this case the Fraunhofer diffraction integral should be written as follows:

$$E(\rho,\theta,z) = C\int_0^a\int_0^{2\pi}\rho' e^{-ik\rho\rho'\cos(\theta'-\theta)}\,d\rho'\,d\theta'. \tag{4.15}$$

Now we can take into account a well known expression for the Bessel functions reported in textbook Olver, Lozier, Boisvert, and Clark (2010):

$$J_n(x) = \frac{i^{-n}}{2\pi}\int_0^{2\pi} e^{-ix\cos\phi}e^{in\phi}\,d\phi', \tag{4.16}$$

and Equation 4.14 can be reduced to

$$E(\rho,\theta,z) = 2\pi C\int_0^a J_0(k\rho'\rho)\rho'\,d\rho'. \tag{4.17}$$

We can now use the recurrence relation of the Bessel functions reported in Olver, Lozier, Boisvert, and Clark (2010)

$$\frac{d}{dx}\left[x^{n+1}J_{n+1}(x)\right] = x^{n+1}J_n(x), \tag{4.18}$$

which integration for $n=0$ gives

$$\int_0^x zJ_0(z)\,dz = xJ_1(x). \tag{4.19}$$

In this case Equation 4.17 can be written as follows:

$$E(\rho) = C\pi a^2\frac{2J_1(ka\rho)}{ka\rho}. \tag{4.20}$$

We are interested in the intensity of the diffraction pattern and in this case the intensity should be written as

$$I(\rho) = \left|E(\rho)^2\right| = I_0\left(\frac{2J_1(ka\rho)}{ka\rho}\right)^2, \tag{4.21}$$

where the constant I_0 can be found by satisfying the energy conversation condition. This result is a more general form of the expression derived by Airy.

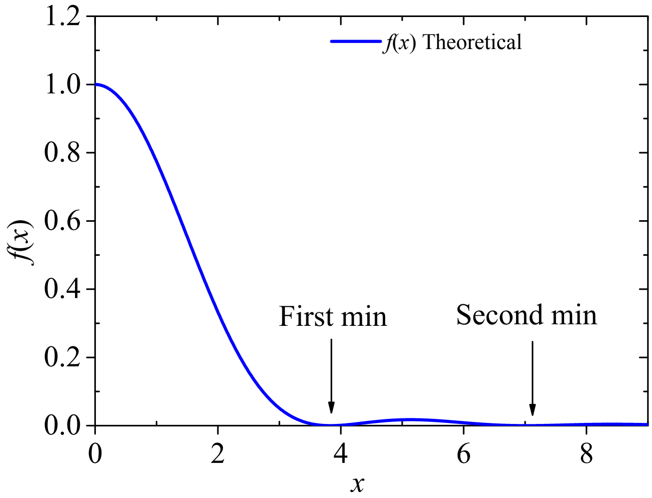

Figure 4.4: *Theoretically calculated plot of a function* $f(x) = (2J_1(x)/x)^2$. *It represents a typical intensity profile of the diffraction pattern from a circular aperture. Black arrows indicate the first and second minima of the function.*

The typical intensity distribution given by Equation 4.21 is shown on Figure 4.4. It is similar to the result obtained by a rectangular aperture in the previous section. The intensity is maximum in the middle of the diffraction pattern and decreases when going far from the center. The first dark ring can be observed for the distances when the function $f(x) = (2J_1(x)/x)^2$ reaches its first minimum. The central bright disk of the image is known as the Airy disk Max and Emil (2002), and the diffraction angle is usually defined as the angle between the central maximum of the intensity and the first dark ring, that is to say given by the following expression:

$$\alpha \approx \frac{1.22\lambda}{2a}. \tag{4.22}$$

This is an important physical property that significantly limits the ability of an imaging system to resolve closely placed objects, limits the applications of lasers and is usually considered as the minimum diffraction angle that one can obtain for an optical system.

4.2 Introduction to FDTD

In the previous section, we have demonstrated that the diffraction provided by various types of apertures can be studied analytically by various approximations of the integral given by Equation 4.1. However, if we want to consider more exotic cases of the electromagnetic field diffracted on apertures with some optically active materials added to the system, the theoretical solution cannot be simply derived for complex geometries. There was a large amount of work done in the development of numerical methods for solving the wave equations since the beginning of the $20th$ century Taflove (2013). We are particularly interested in grid-based differential numerical methods that allows to find approximate solutions of Maxwell's equations. Such a method based on central-difference approximations to the space and time derivatives is the well known Finite-Difference Time-Domain (FDTD) or Yee's method.

The advantage of FDTD method is that it is a time-domain method, and when a broadband pulse is used as the source, the response of the system can be obtained with a single simulation over a wide range of frequencies. This is an useful feature for accelerating the computation time of a system and to find some resonance frequencies of the systems when they are not known exactly. We used this feature in chapter 5 to analyze spectral reflectivity of dispersive materials. Another important feature of FDTD methods is that they provide an evolution of both electric and magnetic fields both in time and space that allows to display animations and insure that the model works correctly. With FDTD methods, we can define any dispersive material at any point of space by using either Drude or Lorentzian models. We hence take into account the dependence of the dielectric properties of the materials as a function of the frequency of the electromagnetic field. Most importantly, in FDTD methods we are not making any other approximations except the ones on central-difference when computing the derivatives. It thus allows us to obtain any kind of aperture or shielding effects directly.

There are of course certain weaknesses of FDTD methods. Since FDTD is a grid based method, the grid in both space and time should be chosen to be small enough to guarantee smooth variations of the field components and the convergence of the solution. For some systems, large computation cell is needed and it might lead to very long computational time. There is also no way to determine the unique values of the materials at the interfaces of different materials and usually the intermediate layers of materials are used to model the interface. Space and time steps should satisfy the stability condition which leads to an increase of computational complexity when the step in space decreases.

There are various both commercially and free distributed packages available. We used the one developed at MIT named *MEEP* Oskooi, Roundy, Ibanescu, Bermel, Joannopoulos, and Johnson (2010). The advantage of this package is that it allows us to use almost any features of FDTD, it is well supported by the scientific and engineering communities and it is not a so called "black box", but all the features can be accessed and modified by the users. This software is available as python and C++ libraries as well as a package using its own language but with limited functionality.

We also used the concept of Perfectly Matched Layer (PML) for all our simulations. This is simply an artificial absorbing layer for the electromagnetic field, commonly used to cut computational regions in numerical methods to simulate problems with open boundaries. The main difference between ordinary absorbing material and PML is that it is designed so that waves incident upon the PML from a non-PML medium do not reflect at the interface. This is a very important feature that allows for avoiding the influence of the boundaries of the cell on the simulated electromagnetic field.

For most of our simulations, we used dispersive materials and there are various databases for materials that can be accessed trough MEEP. However, we are working with amorphous glass and its dielectric function can differ depending on the composition of the material. For this reason, we used our own model for glass, based on the experimental values of the dielectric properties of pure amorphous SiO_2 reported by Palik Palik (1985) and shown on Figure 4.5. We used three Lorentzian fit for the experimental data in order to obtain a continuous dependence of the dielectric function.

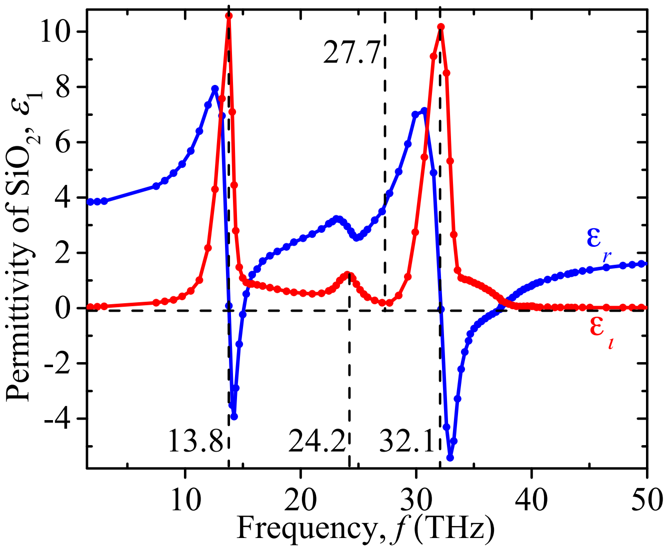

Figure 4.5: *Real and imaginary parts of the relative permittivity $\epsilon(f) = \epsilon_r(f) - i\epsilon_i(f)$ of SiO_2, as a function of frequency $f = \omega/2\pi$. The results are obtained from analyzing the experimental data reported by Palik Palik (1985).*

4.3 Diffraction by an aperture

In this section, we demonstrate the FDTD method using a basic 2D example. Here we want to simulate the diffraction of a monochromatic plane wave with wavelength λ on an infinite slit of width d. We have demonstrated in the beginning of this chapter that the Fraunhofer diffraction pattern in this case should have a maximum intensity in the center and the first minimum defines the diffraction angle. We have chosen the wavelength of the plane wave $\lambda =$

10.9 μm which corresponds to the frequency $f = 27.5$ THz (Zenneck surface modes), and the slit width $d = 21$ μm.

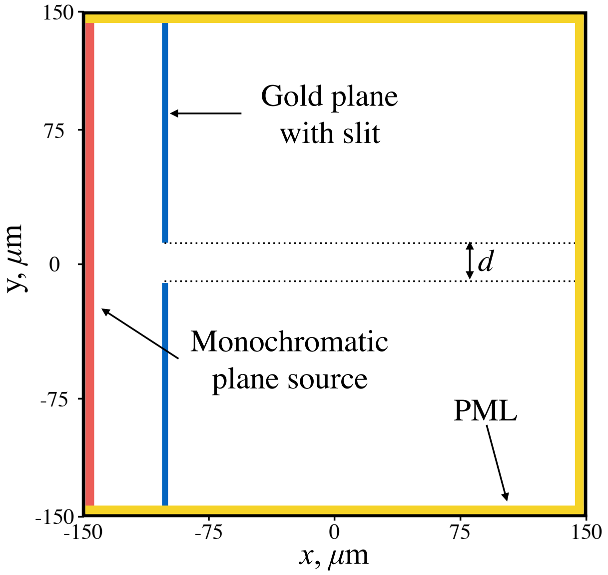

Figure 4.6: *Illustration of the computational cell for a diffraction of a plane wave on an infinite slit of width d.*

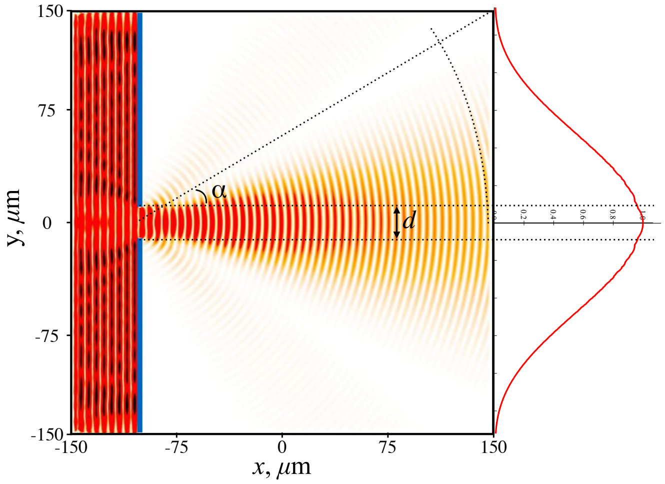

Figure 4.7: *Intensity of diffraction of an electromagnetic monochromatic plane wave of wavelength $\lambda = 10.9$ μm which corresponds to the frequency $f = 27.5$ THz, and a slit width $d = 21$ μm. Red color stands for larger values of the intensity. The angle of diffraction $\alpha = 30°$ is defined by the first dark zone. The blue line shows the metallic plane with an aperture. The right side of the image displays the intensity of the electromagnetic field along the wavefront far from the aperture. The result is obtained by FDTD simulations.*

In order to obtain a diffracted electromagnetic field, we need to initialize the computational cell and the excitation source. Figure 4.6 shows the cell, the position of a continuous excitation monochromatic plane source, the position of the PML and the geometry. In this case, we just use a metallic plane with a slit in the center of the cell. We choose the size of the cell to be 300 μm in width and height and a resolution of 10 points per micron. This resolution guarantees that all the details should be taken into account as there are more than 100 points mesh per electromagnetic field wavelength.
We let the field propagate until the system reaches the steady state regime (the amount of energy emitted by the excitation source is equal to the amount of energy absorbed by the system) and analyze the intensity of the field shown on Figure 4.7. The width of the aperture is comparable to the wavelength and the diffraction angle α can be obtained as the angle between the central maximum and the first minimum observed from the aperture as shown on Figure 4.7.

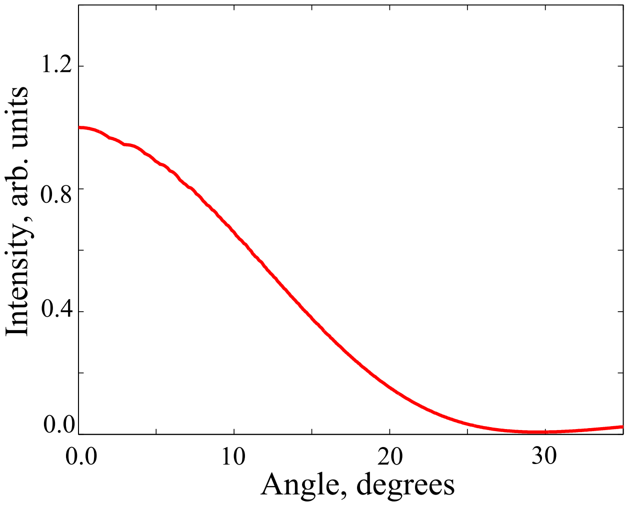

Figure 4.8: *Intensity of diffraction of an electromagnetic monochromatic plane wave of wavelength $\lambda = 10.9$ μm which corresponds to the frequency $f = 27.5$ THz, and the slit width $d = 21$ μm as a function of the observation angle. The angle of diffraction $\alpha = 29.7°$ is defined as the angle of the first dark zone. The result is obtained by post-treatment of FDTD simulations.*

In order to measure this angle precisely, we have developed a post-treatment algorithm that outputs the intensity along the wavefront as a function of the observation angle at a certain distance from the aperture. Figure 4.8 shows the angular profile of the intensity along the wavefromt at a distance of 250 μm far from the aperture. We can now define the angular position of the first minimum of this function corresponding to the diffraction angle $\alpha = 29.7°$. This result repeats the one obtained analytically in the section 4.1.1 by Equation 4.14

where we used Fraunhofer approximation to calculate the diffraction integral. Indeed, the Fraunhofer approximation is about to be valid as Equations 4.23 and 4.24 are satisfied as follows:

$$\frac{\rho}{z} \approx 1.155 \sim 1, \tag{4.23}$$

and

$$\frac{d^2}{z\lambda} = \frac{21^2}{250 \cdot 10.9} \approx 0.162 \ll 1. \tag{4.24}$$

Similar analysis can be preformed for significantly smaller apertures. For example, a slit of width $d = 7$ μm diffracts a plane monochromatic wave with of wavelength $\lambda = 10.9$ μm in all directions as shown on Figure 4.9 and as predicted by Equation 4.14. In this case, there is no first minimum of the diffraction pattern as the aperture is smaller than the wavelength and numerical model should be used in order to obtain the distribution of the electromagnetic field intensity.

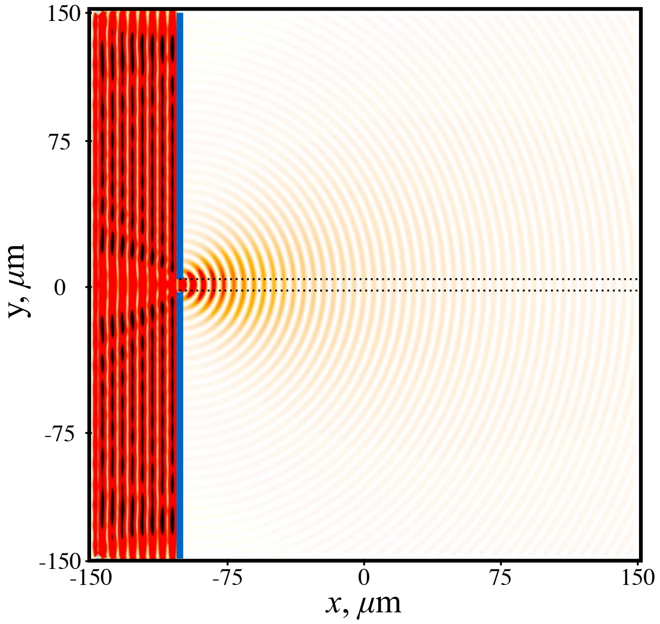

Figure 4.9: *Intensity of diffraction of an electromagnetic monochromatic plane wave of wavelength $\lambda = 10.9$ μm which corresponds to the frequency $f = 27.5$ THz, for a slit width $d = 7$ μm. Red color stands for larger values of the intensity. The blue line shows the metallic plane with an aperture. The result is obtained by FDTD simulations.*

4.4 Diffraction by glass membranes

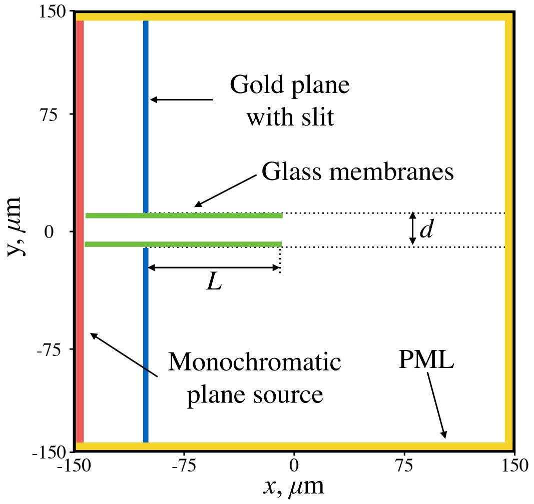

Figure 4.10: *Illustration of the computational cell for the diffraction of a plane wave on an infinite slit of width d with two glass membranes embedded into the slit.*

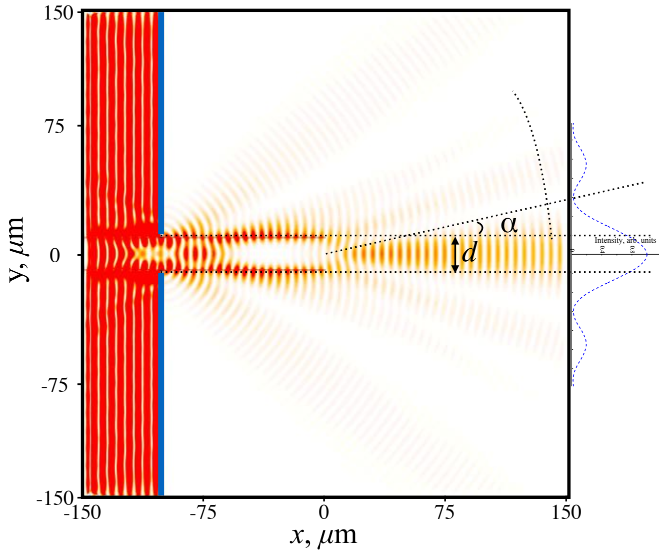

Figure 4.11: *Intensity of diffraction of an electromagnetic monochromatic plane wave of wavelength $\lambda = 10.9$ μm which corresponds to the frequency $f = 27.5$ THz, and the slit width $d = 21$ μm, with glass suspended membranes embedded. The thickness of the membranes is $h = 1$ μm, the suspension length $L = 100$ μm. Red color stands for larger values of the intensity. The blue line shows the metallic plane with an aperture. The right side blue dashed curve demonstrates the intensity profile along the wavefront. The result is obtained by FDTD simulations.*

In this section, we analyze the case where the diffraction angle can be significantly reduced by using a material supporting long-range surface waves. The long-range surface waves (including Zenneck wave, Surface Phonon Polaritons, and guided waves) that can be supported by thin membranes are discussed in details in chapter 5. Here we want to use the feature of surface waves to carry electromagnetic energy outside of the material close to the interfaces. This region is typically about the wavelength in size. This part of the electromagnetic energy carried by the evanescent part of the mode outside of the material can significantly increase the effective width of the aperture and lead to a significantly smaller diffraction angles than in the case of regular apertures. To test this hypothesis, we now consider a system similar to the infinite slit studied in the section above, but with two glass thin membranes embedded into the slit as shown on Figure 4.10.

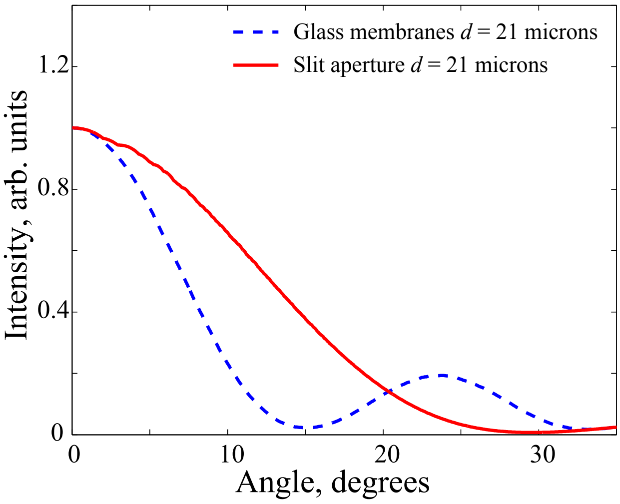

Figure 4.12: *Comparison of field intensity along the front at a distance of 250 μm from the aperture for just an aperture (red curve) and for an aperture with glass suspended membranes embedded (dashed blue curve). The thickness of the membranes is $h = 1$ μm, and the suspension length $L = 100$ μm. The excitation wavelength $\lambda = 10.9$ μm, the slit width $d = 21$ μm for both cases. The results are obtained by FDTD simulations.*

We used 1 μm glass membranes to support long-range surface modes in a broad frequency range as shown in chapter 5. The membranes are attached close to the metallic edge of the aperture and suspended by a distance L far from the metallic plane. We used exactly the same parameters of the FDTD simulations as in the case of a simple slit studied in the previous section and shown on Figure 4.7. The excitation source was used to provide a monochromatic plane wave of wavelength $\lambda = 10.9$ μm which corresponds to the frequency $f = 27.5$ THz, the slit width is $d = 21$ μm, the cell size is 300 μm in both directions with a resolution of 10 points per micron, and the membranes are suspended over a distance $L = 100$ μm far from the aperture. The corresponding intensity map in a steady state regime is shown on Figure 4.11. The angle of diffraction α can be then defined similarly to the case of just an aperture as the angle between the central maximum of the intensity and the first minimum as shown on Figure 4.11.

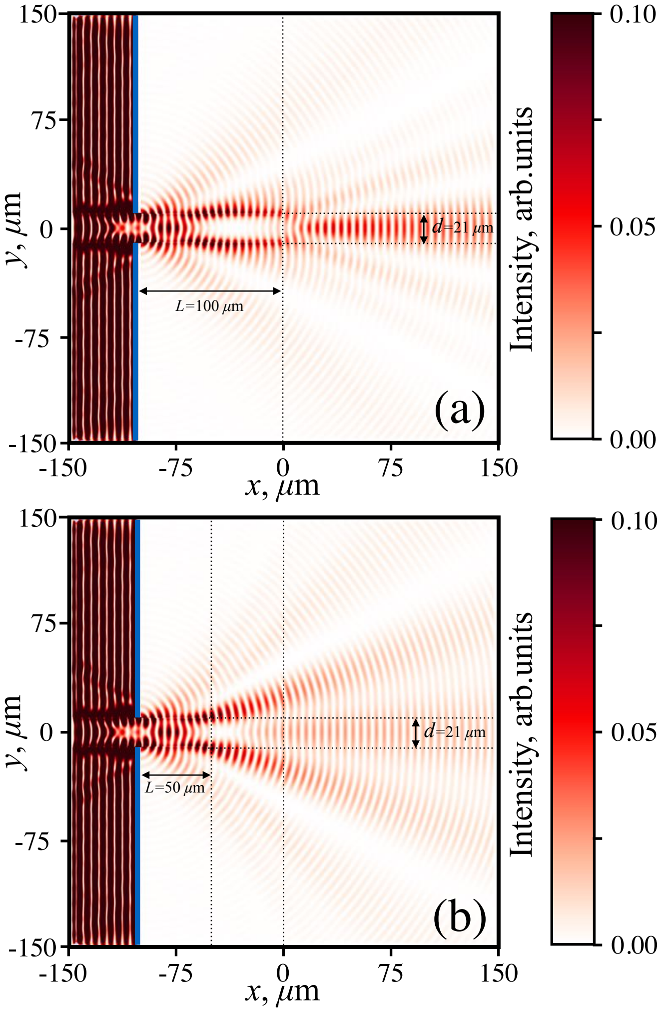

Figure 4.13: *Intensity of diffraction of an electromagnetic monochromatic plane wave of wavelength* $\lambda = 10.9$ *μm which corresponds to the frequency* $f = 27.5$ *THz, and a slit width* $d = 21$ *μm, with glass suspended membranes embedded with a suspension length* $L = 100$ *μm (a) and* $L = 50$ *μm (b). The thickness of the membranes in both cases is* $h = 1$ *μm. The scale is the same on both figures. In the case of short suspension length L the surface modes are not yet formed. The results are obtained by FDTD simulations.*

Figure 4.12 shows the comparison of the electromagnetic field intensity of a simple slit diffraction and a slit with embedded glass membranes embedded diffraction along the wavefront for exactly the same set of parameters. In the case of glass membranes, the diffraction angle $\alpha = 14.8°$ is almost twice smaller than in the case of the slit. This is a very interesting result which demonstrates that surface waves can significantly decrease the diffraction angle of the slit. Note, that the efficiency of diffraction is not the same as the intensities are normalized and it is normally smaller for the case of glass membranes. Indeed, a part of light is also diffracted in the region were the glass membranes are connected to the aperture and only the part of light coupled to the long-range surface modes considered at the end of the membranes contributes to the reduction of the diffraction.

In order to understand the influence of the length of the suspended part of the membranes L, we have analyzed the case where L is twice smaller and the surface mode has not yet formed. The comparison of long suspended membranes $L = 100$ μm with twice shorter suspended membranes $L = 50$ μm is shown on Figure 4.13(a) and Figure 4.13(b) respectively.

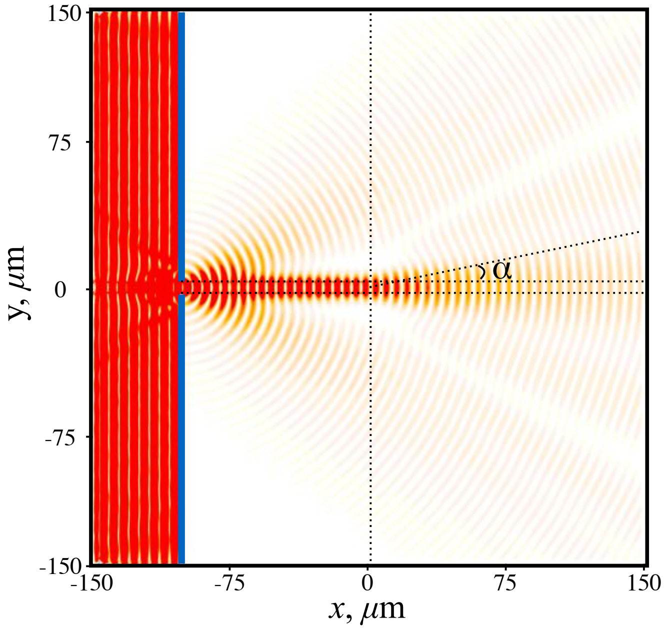

Figure 4.14: *Intensity of diffraction of an electromagnetic monochromatic plane wave of wavelength $\lambda = 10.9$ μm which corresponds to the frequency $f = 27.5$ THz, and a slit width $d = 7$ μm, with glass suspended membranes embedded. The thickness of the membranes is $h = 1$ μm, the suspension length $L = 100$ μm. Red color stands for larger values of the intensity. The blue line shows the metallic plane with an aperture. The result is obtained by FDTD simulations.*

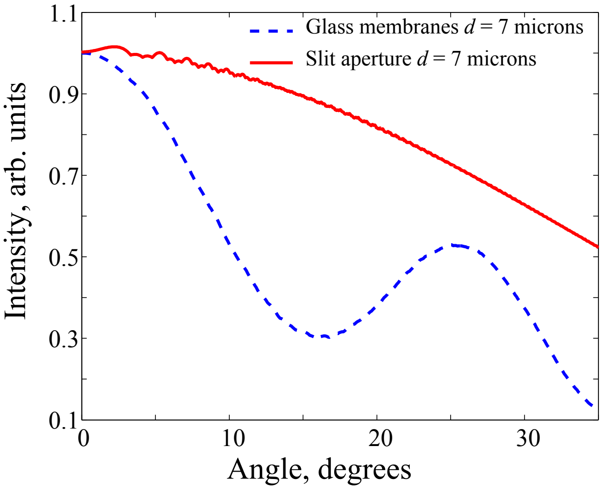

Figure 4.15: *Comparison of field intensity along the wave front at a distance 250 μm from the aperture for just an aperture (red curve) and for an aperture with glass suspended membranes embedded (dashed blue curve). The thickness of the membranes is $h = 1$ μm, the suspension length $L = 100$ μm. The excitation wavelength $\lambda = 10.9$ μm, the slit width $d = 7$ μm for both cases. The results are obtained by FDTD simulations.*

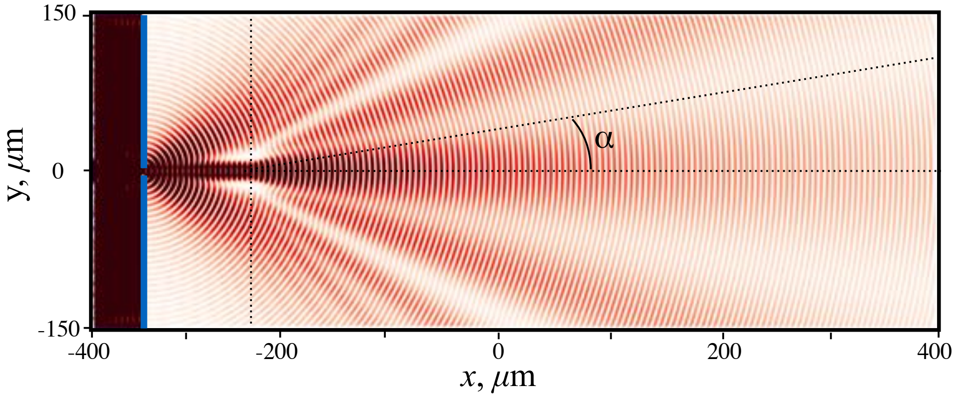

Figure 4.16: *Intensity of diffraction of an electromagnetic monochromatic plane wave of wavelength $\lambda = 10.9$ μm which corresponds to the frequency $f = 27.5$ THz, and a slit of width $d = 7$ μm, with glass suspended membranes embedded. The thickness of the membranes is $h = 1$ μm, the suspension length $L = 100$ μm. Red color stands for larger values of the intensity. The blue line shows the metallic plane with an aperture. The result is obtained by FDTD simulations in a large computation cell.*

In fact, the longer is the suspension, the higher is the possibility of surface modes to be formed, resulting in significantly smaller diffraction angles. However, if the suspended part is too long (longer than the propagation length of the surface mode) there will be no energy delivered to the edge of the membrane and as a result the diffraction efficiency should be negligible. So, for each set of parameters of the system, there should be an optimum suspension length L providing the smallest diffraction angle together with the highest efficiency of diffraction.

We can also study a system where the membranes are placed closer together. This should result in a strong coupling of the surface modes of both membranes. Figure 4.14 shows the case of a slit of width $d = 7$ μm with two glass membranes embedded. The suspension length is $L = 100$ μm, the thickness of the membranes $h = 1$ μm, the excitation wavelength of the source $\lambda = 10.9$ μm. The corresponding intensity profile along the wavefront obtained at 250 μm far from the aperture together with the one of a $d = 7$ μm slit without glass membranes is shown on Figure 4.15.

For membranes system, the intensity takes its local minimum value for an angle $\alpha = 16.3°$ and it reaches its zero for an angle $\alpha = 36.1°$. In the case of the slit, we cannot define the diffraction angle as the energy is diffracted in all directions and does not reach its minimum. In addition, our theoretical estimations of the diffraction angle cannot be applied as the Equations 4.23 and 4.24 are no longer satisfied for such small apertures.

This is a very interesting finding. The fact that the glass membrane system can provide directed radiation even when the size of the structure is less than the wavelength of excitation can be explained by the effective size of the electromagnetic field region where the energy is carried.

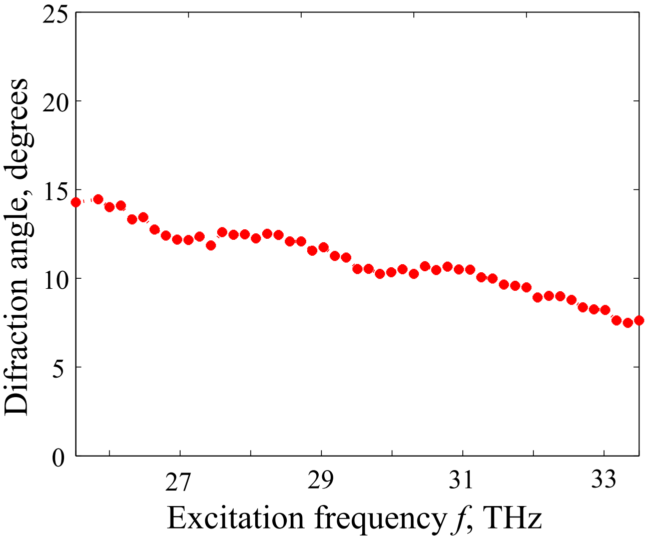

Figure 4.17: *FDTD diffraction angle analysis provided for a slit of width $d = 7$ μm, with 1 μm thick glass membranes embedded for different excitation frequencies. In this frequency range, 1 μm thick glass membranes support long-range surface modes.*

In order to verify that this is still valid for far-field regimes, we perform a simulation in a significantly larger computational cell for the same system ($d^2/z/\lambda \approx 0.007 \ll 1$). Figure 4.16 shows the results for a cell being more than two times larger. In fact, it is a lot more time consuming to use such a cell for all the simulations as the complexity grows rapidly when increasing the size. And there is almost no difference of the intensity profile at longer distances.

In order to check the spectral dependence we can run the simulations for different excitation frequencies and extract the diffraction angle by analyzing the intensity profile at a certain distance from the aperture. The dependence of the diffraction angle as a function of excitation frequency of the source is shown on Figure 4.17. We use the same geometrical parameters of the system with a slit of width $d = 7$ μm, membranes thickness $h = 1$ μm, and membrane suspension length $L = 100$ μm. The result seems to be dependent only on frequency to geometry ratio for this range of frequencies. This can be easily understood by the fact that the dispersion relation of the surface modes in this frequency range is almost flat (the detailed analysis for 1 μm thick membrane is performed in chapter 5).

If the glass membrane does not support a long-range surface mode for a certain frequency (the propagation is smaller than the wavelength), the diffraction is not possible as shown on Figure 4.18, where the excitation frequency is chosen to be 39 Hz. In this case the electromagnetic energy cannot propagate along the tube membranes and they are simply act as an absorber of the field.

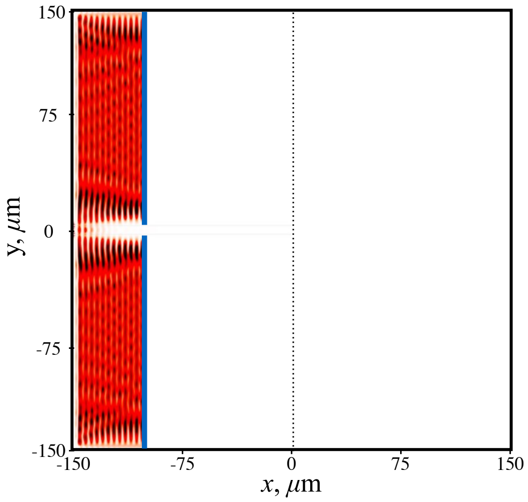

Figure 4.18: *Intensity of diffraction of an electromagnetic monochromatic plane wave of wavelength $\lambda = 7.69$ μm which corresponds to the frequency $f = 39.0$ THz, and a slit of width $d = 7$ μm, with glass suspended membranes embedded. The thickness of the membranes is $h = 1$ μm, the suspension length $L = 100$ μm. Red color stands for larger values of the intensity. The blue line shows the metallic plane with an aperture. The result is obtained by FDTD simulations.*

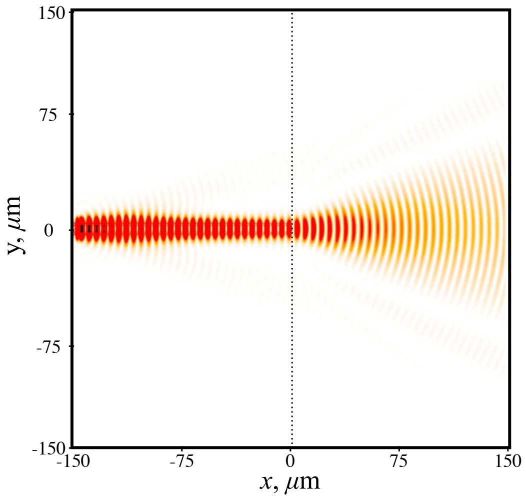

Figure 4.19: *Intensity of diffraction of an electromagnetic monochromatic plane wave of wavelength* $\lambda = 10.9$ *μm which corresponds to the frequency* $f = 27.5$ *THz, by 1 μm thick glass suspended membranes separated by a 5 μm air gap. The Gaussian excitation profile of the source is placed in the middle of the left* y *axis. The width of the source is 10 μm. Red color stands for larger values of the intensity. The result is obtained by FDTD simulations.*

Note that all the analysis of the diffraction angle related to the slit with glass membranes embedded is done for comparison purpose and, in principle, the diffraction angle should be the same when there is no metallic plane with a slit. In this case, we need to use a Gaussian excitation source instead of a plane wave. The result of diffraction by such a source is shown on Figure 4.19. Such a system can be considered for various applications as it provides nearly the same diffraction angle as the one with the slit.

4.5 Conclusions

We have demonstrated that when a plane wave is diffracted by an infinite slit of width comparable to the wavelength, the diffraction angle can be significantly reduced by using two thin embedded parallel membranes. The effect can be observed for frequencies where these membranes support long-range surface modes (e.g. Zenneck modes, Surface Phonon Polaritons or Surface Plasmon Polaritons). For example, a 21 μm width slit with two 1 μm thick glass membranes embedded for an excitation wavelength $\lambda = 10.9$ μm can provide a diffraction angle $\alpha = 14.8°$, while just a slit without membranes provide a diffraction angle of 29.7°. We have also shown that even for apertures sizes smaller than the wavelength, one can obtain directive propagation of diffracted waves. We have also studied the impact of different geometrical parameters of the system on the diffraction angle, such as distance between the membranes, suspension length and size-to-wavelength ratio. Similar approach can be applied to circular shape of the apertures (in this case one needs to use a tube instead of membranes) significantly decreasing the diffraction angles in sub-wavelength optical apertures as in micro-lasers and microscopy applications, for example.

Part III

Thermally excited surface modes in thin membranes

Chapter 5

Formulation and theoretical representation of the problem

In this chapter, we demonstrate the importance of a correct understanding of the assumptions used in the derivations of the electromagnetic surface waves in semi-infinite and symmetrical thin film geometries. Based on Maxwell's formalism we derive the dispersion relations for all types of Transverse Magnetic surface mode guided by these geometries and analyzing their real and imaginary in-plane wave vectors.

5.1 Historical introduction

Since the beginning of the 20*th* Century, physicists were interested in exciting the surface waves at a plane interface between two dielectrics (e.g. water-air interface) for radio frequencies where the real parts of the dielectric functions are positive and one of the material has non-zero absorption. Such a problem was particularly interesting for radio waves propagation close to the surface of the ocean with low losses, as well as for some military radar applications. This type of surface wave was first proposed in 1907 when Zenneck authored a theoretical paper Zenneck (1907) showing the possibility of a wave guided by the interface between the atmosphere and a large body of water. He studied radio waves, a region of the electromagnetic spectrum in which we are not particularly interested when nanomaterials are to be used to guide surface waves. Nonetheless, the principles involved are the same, owing to the scale invariance of the Maxwell's postulates. Although the Zenneck wave, as it is now called Hill and Wait (1980); John Polo (2013), was further investigated, also theoretically, by Sommerfeld Sommerfeld (1909) and Bouwkamp Bouwkamp (1950), its practical existence remains controversial Datsko and Kopylov (2008); Kukushkin (2009).

With the rapid development of nanotechnologies, soon after unsuccessful attempts of excitation and detection of Zenneck waves, the physical community

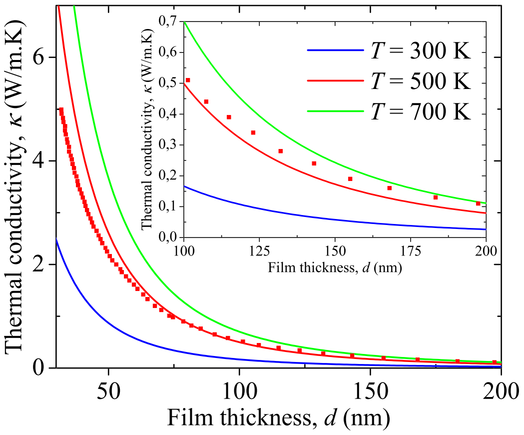

Figure 5.1: *Thermal conductivity as a function of the thickness of a thin film of glass surrounded by air calculated in the work of J. Ordonez-Miranda et al. Ordonez-Miranda, Tranchant, Tokunaga, Kim, Palpant, Chalopin, Antoni, and Volz (2013). The dots correspond to the numerical results reported by G. Chen et al. Chen, Narayanaswamy, and Chen (2005) for temperature* $T = 500$ *K.*

started to work intensively on polaritonic electromagnetic surface waves such as surface plasmon polaritons and later on surface phonon polaritons both existing at the interface of two materials where one has a negative real part in its dielectric function. As it has been discussed in chapter 1, polaritons are widely used for various applications from far-infrared to ultraviolet and their frequencies are usually limited by the materials themselves, drastically restricting their possible effectiveness for certain applications.

One of the typical examples of SPhP performance being limited to a narrow frequency range can be understood by analyzing the work of J. Ordonez-Miranda *et al.* Ordonez-Miranda, Tranchant, Tokunaga, Kim, Palpant, Chalopin, Antoni, and Volz (2013) where he is considering an in-plane thermal conductivity increase due to SPhPs in thin glass membranes. Similar work has been done by the group of G. Chen Chen, Narayanaswamy, and Chen (2005) applying different methods. Both works report the in-plane thermal conductivity of a thin amorphous glass film being several times larger than the one due to phonons as a result of the coupling of SPhP electromagnetic waves with phonons in the membrane, significantly increasing the heat transport along the interface. They are both using the similar equations to compute the in-plane thermal conductivity which can be written as follows:

$$\kappa_{\text{sphp}} = \frac{1}{4\pi d} \int_{\omega_b}^{\omega_t} \hbar\omega\Lambda\beta_R \frac{\partial f_0}{\partial T} d\omega, \tag{5.1}$$

where κ_{sphp} is the in-plane thermal conductivity due to the SPhPs, f_0 is the Bose-Einstein distribution function, T is the temperature of the thin film, β_R is the real part of the wave vector along the z axis, Λ is the propagation length

(mean free path) of the SPhPs, $\hbar$ is the Planck's constant divided by 2π, and ω_b and ω_t are bottom ant top cutoff frequencies of the SPhPs respectively associated with the frequency region where the real part of the glass dielectric function is negative (usually from $\omega_b/(2\pi c) = 1072$ cm^{-1} to $\omega_t/(2\pi c) = 1156$ cm^{-1}). For example, for $T = 500$ K and $d = 100$ nm both reports the value κ_{sphp} being around 0.5 $W/(m.K)$ which is in the range of the bulk value of the usual (due to the phonons) thermal conductivity of amorphous glass. Note that the value of course increases when temperature increases and membrane thickness decreases as shown on Fig. 5.1.
Another remarkable work has been done by J-J. Greffet *et al.* Greffet, Carminati, Joulain, Mulet, Mainguy, and Chen (2002) where they are demonstrating a coherent thermal emission by diffraction of the SPhPs from a grating etched at a SiC-air interface shown on Fig. 5.2.

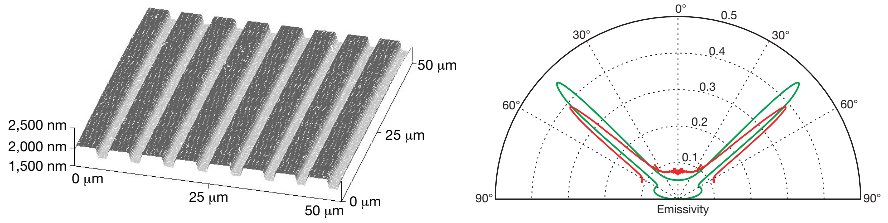

Figure 5.2: *Image of the grating used by J-J. Greffet et al. demonstrating a coherent thermal source and its polar plot of emissivity. Red line, experimental data; green line, theoretical calculation. The measurements were taken by detecting the intensity emitted by the sample in the far field as a function of the emission angle. Greffet, Carminati, Joulain, Mulet, Mainguy, and Chen (2002)*

Their approach of constructing a coherent thermal source based on Surface Phonon-Polaritons is in principle valid for any frequency region where these polaritons are supported by the material and is usually limited by the dielectric material of the substrate. We actually believe that any thermally excited surface mode with long enough propagation length can be used to create such a thermal source for a designed frequency by considering thin membranes. All the long-range surface modes that can exist in a thin sub-wavelength membranes are theoretically studied by F. Yang *et al.* Yang, Sambles, and Bradberry (1991). They have derived the dispersion relation and the propagation length for all the surface modes that can be supported by thin films. They based their theoretical work on Maxwell's equation solution and considered all possible cases for various combinations of dielectric functions of the materials. The solution provided includes polaritons, Zenneck modes, and transverse magnetic (TM) guiding modes.

5.2 Surface electromagnetic modes supported by a single interface

Here, we study the surface electromagnetic waves that can be supported by a planar single interface formed by two semi-infinite media, 1 and 2. To simplify the derivations, we will consider the first media to be nonmagnetic (the relative permeability is equal to zero) and having no absorption (the imaginary part of the dielectric function is zero). The coordinate axis are chosen in such a way that z and y are along the interface, x is perpendicular to the interface as shown on Fig. 5.3. Such a system is standard and similar derivations can be found in any textbook of electromagnetism and waveguiding John Polo (2013) Yang, Sambles, and Bradberry (1991).

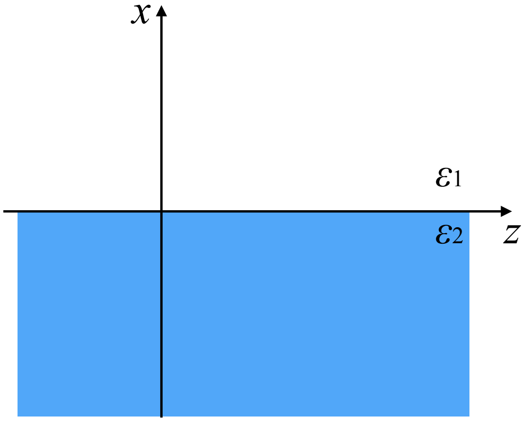

Figure 5.3: *Single interface formed by two semi-infinite media of diectric functions* ϵ_1 *and* ϵ_2. *Medium 1 is a pure non-absorbing dielectric and medium 2 is an optically active material with a dielectric function in the form of* $\epsilon_2 = \epsilon_{2r} - i\epsilon_{2i}$, $\epsilon_{2i} > 0$.

For isotropic media, Transverse Electric (TE) components cannot be excited due to the boundary conditions and the symmetry of the system. The only possible solution of surface wave should be written in the Transverse Magnetic (TM) form and is best described by considering its one non-zero magnetic field component which lies in the plane of the interface in the y direction and has the form:

$$\boldsymbol{H} = \boldsymbol{H}_0 f(x) \exp(i\omega t - kz) = \boldsymbol{H}_y, \tag{5.2}$$

were $\boldsymbol{H}_0$ is a normalization vector, the in-plane wave vector is complex and written in the form of $k = k_r - ik_i$ and the function $f(x)$ describes the field evolution in the direction perpendicular to the distance away from the interface in the x direction. Using Maxwell's equations, the electric field components can be calculated as

$$\boldsymbol{E}_z = \frac{i}{\omega\epsilon}\frac{\partial \boldsymbol{H}_y}{\partial x}, \tag{5.3}$$

$$\boldsymbol{E}_x = -\frac{k}{\omega\epsilon}\boldsymbol{H}_y. \tag{5.4}$$

We write the $f(x)$ function for the first and second media in the following form

$$f(x) = \exp{(-\alpha_1 x)}, \text{ for } x > 0, \tag{5.5}$$

$$f(x) = \exp{(\alpha_2 x)}, \text{ for } x < 0, \tag{5.6}$$

with the transverse wave vectors $\alpha_1 = k^2 - k_0^2\epsilon_1$ and $\alpha_2 = k^2 - k_0^2\epsilon_2$, where k is the wave vector along the interface and $k_0 = \omega/c$ is the wave vector in the vacuum with ω and c being the excitation angular frequency and speed of light in the vacuum respectively.

The continuity of the tangential electrical field component at the interface ($x = 0$) leads to the following dispersion relation

$$\epsilon_1\alpha_2 = -\epsilon_2\alpha_1. \tag{5.7}$$

5.2.1 Non-realistic case of non-absorbing metal, $\epsilon_{2r} < 0$, $\epsilon_{2i} = 0$, Fano modes

In the field of Surface Phonon Polaritons many physicists assume the absorption of the second media to be negligible $\epsilon_{2i} = 0$, which is never the case in reality. Rewriting the dispersion relation Eq. 5.7 in the form where all the relative permittivities are real

$$k_r = k_0\left[\frac{\epsilon_1\epsilon_{2r}}{\epsilon_{2r} + \epsilon_1}\right]^{1/2}, \text{ for } \epsilon_{2r} < 0,\ \epsilon_{2r} < -\epsilon_1. \tag{5.8}$$

Eq. 5.8 is a very commonly used dispersion relation in the community of radiative heat transfer and it describes Fano modes dispersion relation which corresponds to a very idealistic case. The condition on the dielectric function in Eq. 5.8 gives a limitation on the frequency range where the material can support surface modes and in principle is incorrect for any real material. We believe that this misunderstanding of the limitations of this dispersion relation leads to significant mistakes of the theoretical treatment of electromagnetic surface waves in modern physics.

5.2.2 Realistic case of absorbing material, $\epsilon_{2i} \neq 0$, Plasmon-, Phonon- and Exciton-polaritons, Zenneck modes

Instead we need to consider the realistic case for any real material when the absorption is not zero ($\epsilon_{2i} \neq 0$). In this case, ϵ_2, k, α_1 and α_2 are all complex and Eq. 5.7 leads to the following solution

$$k_r = k_0 \left[\frac{\epsilon_1}{(\epsilon_{2r}+\epsilon_1)^2+\epsilon_{2i}^2}\right]^{1/2} \left[\frac{\epsilon_e^2+(\epsilon_e^4+\epsilon_1^2\epsilon_{2i}^2)^{1/2}}{2}\right]^{1/2}, \tag{5.9}$$

$$k_i = k_0 \left[\frac{\epsilon_1}{(\epsilon_{2r}+\epsilon_1)^2+\epsilon_{2i}^2}\right]^{1/2} \frac{\epsilon_{2i}\epsilon_1}{\left[2(\epsilon_e^2+(\epsilon_e^4+\epsilon_1^2\epsilon_{2i}^2)^{1/2})\right]^{1/2}}, \tag{5.10}$$

where

$$\epsilon_e^2 = \epsilon_{2r}^2+\epsilon_{2i}^2+\epsilon_1\epsilon_{2r}. \tag{5.11}$$

Now we will examine specific cases of Eqs. 5.9-5.10. If $\epsilon_{2r} < 0$, $-\epsilon_{2r} >> \epsilon_{2i}$ and $-\epsilon_{2r} > \epsilon_1$, then from Eqs. 5.9-5.10 we can find

$$k_r \simeq k_0 \left[\frac{\epsilon_{2r}\epsilon_1}{\epsilon_{2r}+\epsilon_1}\right]^{1/2} > k_0\epsilon_1^{1/2}, \tag{5.12}$$

$$k_i \simeq k_0 \frac{\epsilon_{2i}\epsilon_1}{2(-\epsilon_{2r}-\epsilon_1)} \left[\frac{\epsilon_1}{-\epsilon_2 r(-\epsilon_{2r}-\epsilon_1)}\right]^{1/2}. \tag{5.13}$$

Those equations describe a realistic case of surface plasmon- or phonon-polaritons with a real part of the in-plane wave vector being greater than the one of light ($k_r > k_0\epsilon_1^{1/2}$) and with an imaginary in-plane wave vector k_i being proportional to the absorption of the second medium.

Now let us consider the case when $\epsilon_{2r} = 0$. In this case,

$$k_r = k_0 \left[\frac{\epsilon_{2i}\epsilon_1\left(\epsilon_{2i}+\left[\epsilon_{2i}^2+\epsilon_1^2\right]^{1/2}\right)}{2\left(\epsilon_{2i}^2+\epsilon_1^2\right)}\right]^{1/2} < k_0\epsilon_1^{1/2}, \tag{5.14}$$

$$k_i = k_0 \left[\frac{\epsilon_{2i}\epsilon_1^3}{2\left(\epsilon_{2i}^2+\epsilon_1\right)\left[\epsilon_{2i}+\left(\epsilon_1^2+\epsilon_{2i}^2\right)^{1/2}\right]}\right]^{1/2}. \tag{5.15}$$

This new dispersion represents a surface exciton-polariton. For this case, $\epsilon_{2i} >> \epsilon_1$, which is true close to the transverse exciton frequency of an optically active semiconductor.

These results lead to the fact that the dielectric function of the material does not limit the surface modes existence and, in principle, they can be excited at the interface of any material even when the real part of the dielectric constant is positive. The usual understanding of the dispersion relation is that the light line

($k = k_0\epsilon_1^{1/2}$) separates the radiating and non-radiating modes of the dispersion curve. But this is only valid for Fano modes when there is no absorption ($\epsilon_{2i} = 0$). It is also clear that when the absorption is small ($\epsilon_{2i} \approx 0$) and the real part of the dielectric function of the second medium is positive ($\epsilon_{2r} > 0$) modes should exist as predicted by Zenneck. Usually, for Zenneck modes, the propagation length is smaller than the wavelength and the detection remains complicated.

Please note that the results discussed here are already well established and can be found in the various contents of the literature and has been already summarized, for example, by F. Yang *et al.* Yang, Sambles, and Bradberry (1991).

5.3 Long-range surface modes in thin symmetrically surrounded membranes

In the previous section, we have demonstrated that there are different surface modes supported by an interface between two semi-infinite media. Among them are Zenneck modes. Unfortunately, they have a very short propagation length and cannot be detected so easily. For this reason we are looking for a system which can significantly increase the propagation length by lowering the effective absorption of the guiding channel. This can be done by the coupling of two modes at two parallel interfaces which can be practically realized by creating a thin membrane. Thus, we here consider a thin membrane of thickness d with a dielectric function in the form of $\epsilon_2 = \epsilon_{2r} - i\epsilon_{2i}$ surrounded by semi-infinite media specified by ϵ_1 and ϵ_3 as shown on Fig. 5.4.

Similar to the derivation of the dispersion relation for an interface of two infinite materials described in the textbooks of electromagnetism John Polo (2013) one can solve Maxwell's equations under proper boundary conditions and end up with a dispersion relation for a thin membrane as follows:

$$\tanh(\alpha_2 d) = -\frac{\epsilon_2\alpha_2(\epsilon_1\alpha_3 + \epsilon_3\alpha_1)}{\epsilon_1\epsilon_3\alpha_2^2 + \epsilon_2^2\alpha_1\alpha_3}, \tag{5.16}$$

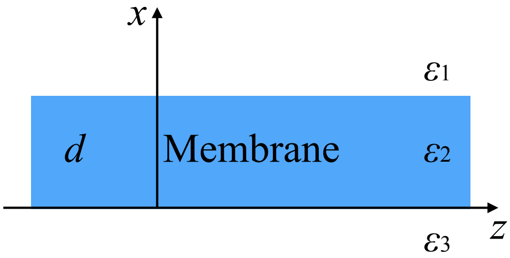

Figure 5.4: *Thin membrane of thickness d and dielectric function $\epsilon_2 = \epsilon_{2r} - i\epsilon_{2i}$ surrounded by semi-infinite media specified by ϵ_1 and ϵ_3.*

where α_j the transverse wave vectors are given by

$$\alpha_j^2 = k^2 - k_0^2\epsilon_j, \tag{5.17}$$

with $j = 1, 2, 3$ and $k_0 = \omega/c$, where ω is the excitation angular frequency and c is the speed of light in the vacuum. For surface waves being bounded to the interfaces of the membrane, we require both real parts of the transverse wave vectors outside of the membranes to be positive $\mathrm{Re}(\alpha_1) > 0$ and $\mathrm{Re}(\alpha_3) > 0$ and we need to remind that the field in the region $j = 3$ is in the form of $f(x) = \exp(\alpha_3 x)$ for $x < 0$. Assuming that the membrane is surrounded by air ($\epsilon_1 = \epsilon_3 = \epsilon_{\mathrm{air}} = 1$), Eq. 5.16 is split into two different branches. The dispersion relation of the anti-symmetric mode in H_y can be written as

$$\tanh\left(\frac{d\alpha_2}{2}\right) = -\frac{\epsilon_1\alpha_2}{\epsilon_2\alpha_1} \tag{5.18}$$

and dispersion relation of the symmetric mode in H_y, which has the form

$$\tanh\left(\frac{d\alpha_2}{2}\right) = -\frac{\epsilon_2\alpha_1}{\epsilon_1\alpha_2}. \tag{5.19}$$

Usually, long-range surface modes are obtained for the symmetric branch of the dispersion relation given by Eq. 5.19 John Polo (2013) Yang, Sambles, and Bradberry (1991) Ordonez-Miranda, Tranchant, Tokunaga, Kim, Palpant, Chalopin, Antoni, and Volz (2013), which when $d \to 0$ has the solution $\alpha_1 \to 0$, standing for a long-range surface mode. Considering that the thickness of the membrane d is small enough $|\alpha_2| << 2/d$, Eq. 5.19 can be expanded up to first order as

$$\frac{d\alpha_2}{2} \simeq -\frac{\epsilon_2\alpha_1}{\epsilon_1\alpha_2} \tag{5.20}$$

and the real part of the in-plane wave vector can be written as

$$k_r \simeq k_0\epsilon_1^{1/2}\left[1 + \frac{\epsilon_1}{2}\left(\frac{\pi d}{\lambda_0}\right)^2 \frac{(\epsilon_{2r}^2 + \epsilon_{2i}^2 - \epsilon_1\epsilon_{2r})^2 - \epsilon_1^2\epsilon_{2i}^2}{(\epsilon_{2r}^2 + \epsilon_{2i}^2)^2}\right] \tag{5.21}$$

and the imaginary part as

$$k_i \simeq k_0\epsilon_1^{3/2}\left(\frac{\pi d}{\lambda_0}\right)^2 \frac{\epsilon_{2i}(\epsilon_{2r}^2 + \epsilon_{2i}^2 - \epsilon_1\epsilon_{2r})}{(\epsilon_{2r}^2 + \epsilon_{2i}^2)^2}, \tag{5.22}$$

where $\lambda_0 = 2\pi/k_0$ is the vacuum wavelength.

5.3.1 Symmetrically surrounded non-absorbing dielectric, $\epsilon_{2r} > 0$, $\epsilon_{2i} = 0$

If $\epsilon_{2r} > 0$ and $\epsilon_{2i} = 0$ then Eqs. 5.21- 5.22 can be simplified as follows

$$k_r \simeq k_0 \epsilon_1^{1/2} \left(1 + \frac{\epsilon_1}{2} \left[\frac{\pi d}{\lambda_0} \right]^2 \frac{(\epsilon_{2r} - \epsilon_1)}{\epsilon_{2r}^2} \right) > k_0 \epsilon_1^{1/2} \tag{5.23}$$

and

$$k_i \simeq 0. \tag{5.24}$$

This is the case when ϵ_{2r} has to be greater than ϵ_1 so that a bounded mode can be supported by a membrane. This is a well-known case of a TM guided mode and it is simply formed by the coupling of the fields at the two interfaces of the membrane. This is of course a non-realistic case since there should be some absorption limiting the propagation length of this mode. But in general this is a mode with infinite propagation.

5.3.2 Symmetrically surrounding excitonic absorber, $\epsilon_{2r} = 0$, $\epsilon_{2i} > 0$

Similar to a semi-infinite system, we should also consider a mode corresponding to the case when $\epsilon_{2r} = 0$ in an absorbing material called excitonic mode in semiconductors. It can be observed near the excitonic transverse resonance where the absorption is significant and the real part of the relative permittivity is changing its sign by going through zero. In this case, Eqs. 5.21- 5.22 should be written as follows:

$$k_r \simeq k_0 \epsilon_1^{1/2} \left(1 + \frac{\epsilon_1}{2} \left[\frac{\pi d}{\lambda_0} \right]^2 \frac{(\epsilon_{2i}^2 - \epsilon_1^2)}{\epsilon_{2i}^2} \right) > k_0 \epsilon_1^{1/2} \tag{5.25}$$

and

$$k_i \simeq k_0 \epsilon_1^{3/2} \left[\frac{\pi d}{\lambda_0} \right]^2 \frac{1}{\epsilon_{2i}}. \tag{5.26}$$

Note that for this mode the stronger is the absorption the longer is the propagation length of the mode as follows from Eq. 5.26.

5.3.3 Symmetrically surrounded metal, $\epsilon_{2r} < 0$, $\epsilon_{2i} > 0$

If $\epsilon_{2r} < 0$ then Eqs. 5.21- 5.22 are written as follows

$$k_r \simeq k_0 \epsilon_1^{1/2} \left(1 + \frac{\epsilon_1}{2} \left[\frac{\pi d}{\lambda_0} \right]^2 \frac{(|\epsilon_{2r}| + \epsilon_1)^2}{\epsilon_{2r}^2} \right) > k_0 \epsilon_1^{1/2} \tag{5.27}$$

and

$$k_i \simeq k_0 \epsilon_1^{3/2} \left[\frac{\pi d}{\lambda_0}\right]^2 \frac{|\epsilon_{2r}| + \epsilon_1}{\epsilon_{2r}^3} \epsilon_{2i}. \tag{5.28}$$

This is the case of surface plasmon- and phonon-polaritons appearing in thin films under the limit $\alpha_2 << 2/d$. Note, that k_i is proportional to ϵ_{2i}.

5.3.4 Symmetrically surrounded absorbing dielectric, $\epsilon_{2r} > 0$, $\epsilon_{2i} > 0$

In the case of two Zenneck modes being coupled together at the interfaces of the membrane, we need to use Eqs. 5.21-5.22 and it is clear that we should have a regime similar to TM guided modes described in the section 5.3.1 but with more absorption.

5.4 Calculation of the dispersion relation and propagation length in amorphous glass

The results discussed in sections 5.3.3-5.3.4 can be demonstrated by considering a real material with a complex spectral dielectric function.

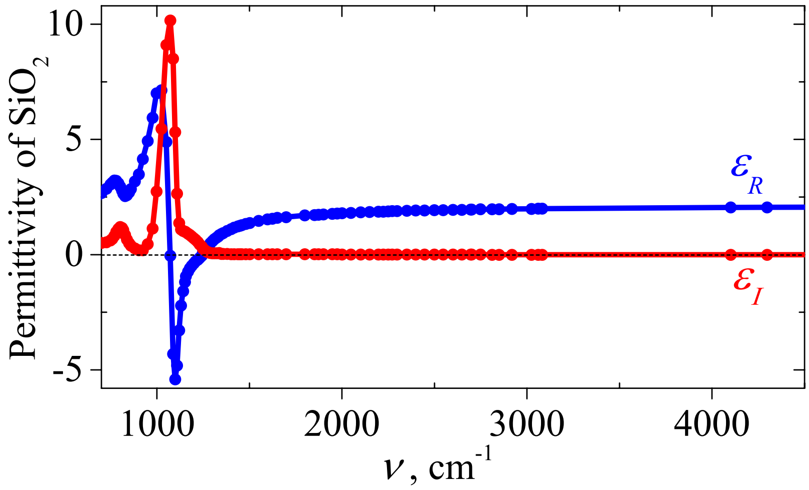

Figure 5.5: *Real (blue line) and imaginary (red line) parts of the relative permittivity of SiO_2. The data is obtained from the analysis of experimental measurements reported in the literature Palik (1985).*

We will consider polar dielectrics (e.g. amorphous SiO_2) with a strong resonance of the dielectric function around $\nu = 1000$ cm^{-1} due to optical phonons. The experimental measurements of the dielectric function of pure amorphous silica are reported in the literature and we use the one reported by E. D. Palik

Palik (1985). The experimental values can be slightly different from one type of deposition to another depending on the micro structure of the samples.
On Fig 5.5, we plot the real and the imaginary parts of the relative permittivity of pure amorphous SiO_2 for a broad frequency range. There are different frequency regions corresponding to different behaviours of the real and imaginary relative permittivities. We will now apply the formalism developed earlier in this chapter to calculate the dispersion relations of long-range surface electromagnetic modes in the single interface geometry and in the thin film geometry.

5.4.1 Single SiO_2-air interface geometry

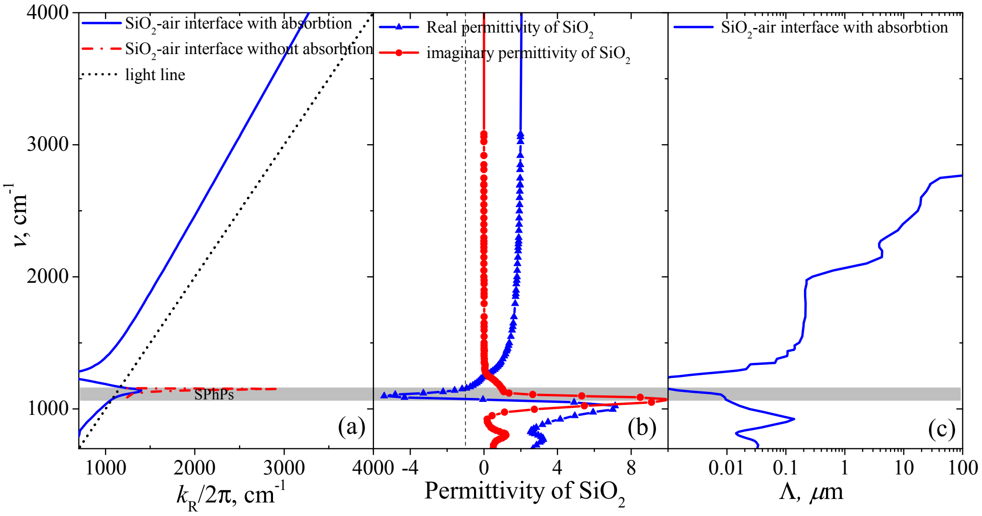

Figure 5.6: *(a) Comparison of dispersion relations of SiO_2-air interfaces obtained by considering the absorption (blue line) and by neglecting the absorption (red dashed-dot curve); (b)Real (blue line) and imaginary (red line) parts of the relative permittivity of SiO_2; (c) Propagation length of symmetric surface modes at a SiO_2-air interface obtained by considering the absorption inside SiO_2. The gray region indicates the frequency range where the Fano modes condition on the real part of the relative permittivity of SiO_2 ($\epsilon_r < -\epsilon_{air} = -1$) is satisfied.*

Applying the formalism shown in section 5.3.3, we can analytically obtain the dispersion relation and propagation length of electromagnetic surface modes and compare them with the ones commonly used to describe SPhPs by neglecting the absorption (Fano modes).
Figure 5.6(a) and (c) shows this comparison for the dispersion relations and propagation length respectively. As it is shown on these two figures, the formalism of Fano modes (non-realistic case with zero absorption) cannot provide any information about the propagation of surface modes in the frequency regions outside the one where the real part of the relative permittivity of silica is smaller than the minus real part of surrounding air ($\epsilon_r < -\epsilon_{air} = -1$) and we

should of course consider absorption in order to get the propagation length of these modes. In fact, one can switch to the formalism where the wave vector is real and the frequency is complex. This is an alternative way of describing the surface modes with absorption and the lifetime of the modes can be obtained by considering the imaginary part of the excitation frequency. In our work, we are using the formalism where the frequency is real and the wave vector is complex. In this formalism the propagation length can be calculated by considering the imaginary part of the in-plane wavevector. Also note that the dispersion curve crosses the light line only for the frequencies where the dielectric function satisfies the Fano mode condition ($\epsilon_r < -\epsilon_{air} = -1$). The propagation length is usually less than the wavelength for the case of a single interface. This short propagation length significantly limits certain applications of these modes for single interface geometry and originates from the high absorption of the material at these frequencies.

5.4.2 Thin SiO_2 film symmetrically surrounded by air

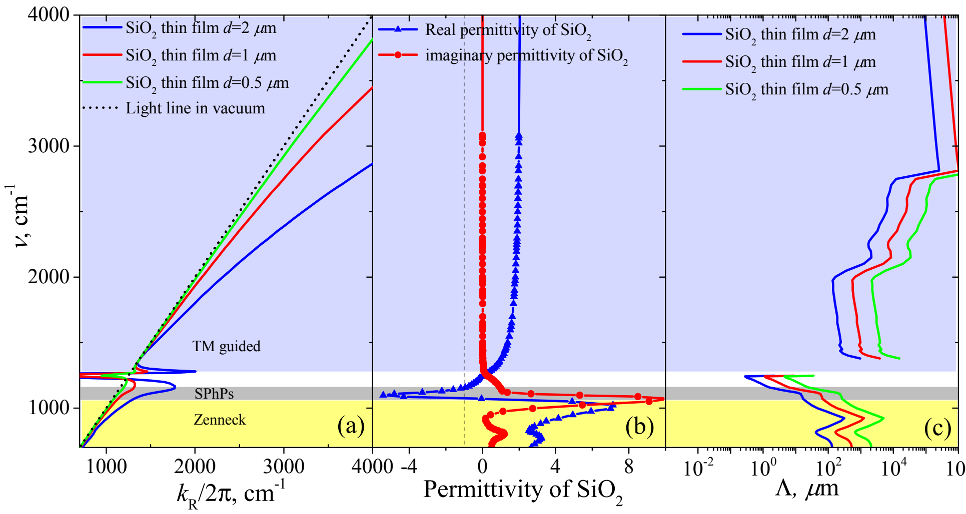

Figure 5.7: *(a) Comparison of dispersion relations of a suspended SiO_2 thin films for different film thicknesses d obtained by considering the absorption of the material; (b) Real (blue line) and imaginary (red line) parts of the relative permittivity of SiO_2; (c) Propagation length of symmetric surface modes in thin SiO_2 membranes symmetrically surrounded by air obtained by considering the absorption inside SiO_2. The gray region indicates the frequency range where the Fano mode condition on the real part of the relative permittivity of SiO_2 ($\epsilon_r < -\epsilon_{air} = -1$) is satisfied. The yellow and blue regions indicate Zenneck modes and TM guided modes respectively.*

Applying the formalism shown in section 5.3.4, we can analytically obtain the dispersion relation and propagation length of electromagnetic surface modes for a thin membrane of SiO_2 suspended in the air. Figures 5.7(a) and (c) show this comparison for the dispersion relation and propagation length comparison respectively for three different thicknesses of membrane. Note that the thin layer approximation has been introduced in order to obtain analytic solution of the dispersion relation for this geometry and the layers with thicknesses more than $d = 2$ μm should be considered by solving the dispersion relation numerically. In the case of a symmetrically surrounded thin glass membrane, the dispersion relation lies beneath the light line almost over the entire frequency range and the dispersion relation approaches the light line when the thickness of the membrane is reduced as expected since the influence of the material decreases. This important feature allows for the photon-like behaviour of the dispersion relation and leads to a significantly higher propagation length of these modes. Indeed, the propagation length of $d = 1$ μm thick membrane for Zenneck modes reaches almost several hundreds times their wavelength and is almost four orders of magnitude larger than in the case of a single interface. Another important feature of a symmetrically surrounded membrane is that it acts as a TM waveguide for frequencies higher than the SPhP resonance. The absorption in this case is very low and the propagation length of the mode is large.

5.5 Conclusions

The results discussed above lead to the fact that surface electromagnetic waves can be excited in a significantly broader frequency range than they are traditionally assumed by applying a non-realistic approximation of Fano modes for zero-absorption materials. When dealing with real optically active dielectrics (such as SiO_2, SiC, SiN, VO, BN etc.), we need to consider their absorption and, as a result, we need to take into account all the types of surface modes including Zenneck modes. Another important fact is that by tuning the thickness of a symmetrically surrounded membrane we can tune the propagation length of these modes. It means that even for Zenneck modes, we can achieve several wavelengths propagation length by considering a 1 micron thickness membrane of ordinary amorphous glass when for a single interface their propagation length is less than their wavelength. This finding provides a possibility to experimentally detect Zenneck modes by using a diffraction grating etched on a surface of a polar dielectric membrane and experimentally detect their far-field thermal emission. This experimental detection is discussed in the chapter 6.

Chapter 6

Numerical simulations and experimental detection of broadband thermally excited surface waves

In this chapter, we create an electromagnetically equivalent system to a thin membrane by using a metallic mirror and run electromagnetic numerical simulations to verify this assumption. The results from these numerical simulations are then used to design a nanostructured sample to experimentally detect these long-range thermally excited surface waves with their dispersion relations and propagation length by means of emission Fourier Transform Infrared (FTIR) spectroscopy. We believe that these hybrid surface modes should significantly increase the in-plane thermal conductivity of nanolayered structures, and can be used to produce coherent thermal sources and change the vision of infrared nanophotonics. These results are reported in our article Gluchko, Palpant, Volz, Braive, and Antoni (2017).

6.1 Finite-Difference Time-Domain numerical simulations of a thin glass layer deposited on aluminum

We want to experimentally prove that a thin suspended SiO_2 membrane can support long-range electromagnetic surface waves in a significantly broader frequency range than in the case of a single interface geometry according to theoretical results demonstrated in the previous chapter. We are particularly interested in thermally excited electromagnetic surface waves due to their potential impact on the improvement of the in-plane thermal conductivity of these membranes and the creation of coherent broadband thermal sources. The existence of broadband thermally excited electromagnetic surface waves can be demonstrated by diffracting their near-field thermal emission with a diffraction grating etched on the surface of the membrane into far-field. Unfortunately, to precisely detect the corresponding far-field diffraction, we need to fabricate a grating with a lateral size being larger than the propagation length of these modes. For a $d = 1$ μm thick membrane the maximum propagation length can exceed 1 millimeter as demonstrated in the section 7.4.2 and the fabrication of such a large suspended SiO_2 membrane remains technologically challenging.

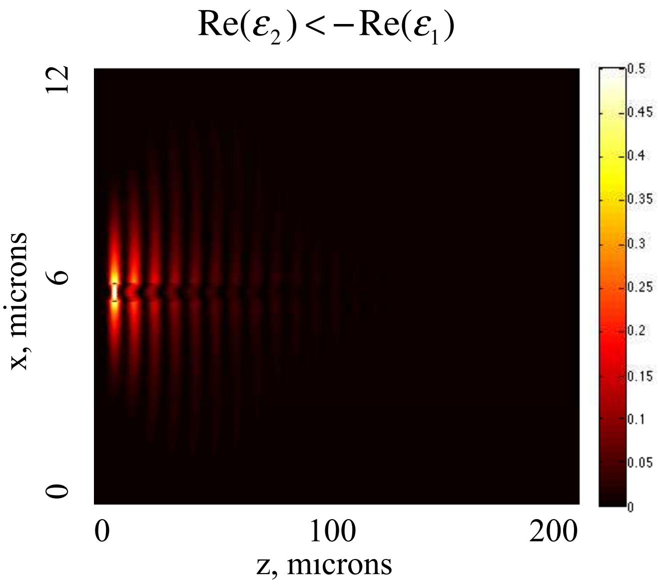

Figure 6.1: *Energy density plot of a SPhP mode bounded to the interfaces of a 1 μm thick suspended SiO_2 membrane. The result is obtained by FDTD numerical simulations by using the excitation frequency $\nu = 1050$ cm^{-1} where the relative permittivity of SiO_2 satisfies the SPhP condition ($\epsilon_r < -\epsilon_{air} = -1$). The color scale is in arbitrary units.*

This technology limitation can however be simply circumvented by considering an electromagnetically equivalent system. As far as electromagnetism is concerned, a sample consisting of a twice thinner layer of SiO_2 deposited over a metallic film - the role of which is to optically isolate the dielectric thin layer from the substrate - is a strictly equivalent structure. To prove this equivalence, we calculate dispersion curves of surface waves on a 1 μm thick suspended SiO_2 membrane and on a 0.5 μm thick SiO_2 thin film deposited on an aluminum layer obtained by means of FDTD simulations. We use the MEEP code Oskooi, Roundy, Ibanescu, Bermel, Joannopoulos, and Johnson (2010) the one discussed in details in the chapter 4. We performed a simulation for each frequency by using a spatial Gaussian profile monochromatic continuous electromagnetic source placed on the left side of the membrane (see Figure 6.1) and let the field propagate bounded to the interface of the membrane. We then developed a post treatment algorithm that defines the spatial frequency and the propagation length of the bounded mode for a specific excitation frequency by fitting the numerical data.

6.1.1 FDTD numerical results for a suspended 1 μm thick SiO$_2$ membrane

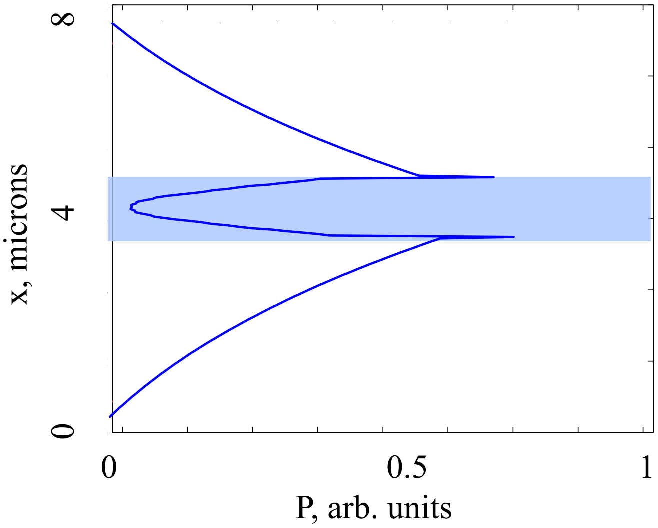

Figure 6.2: *Energy density profile of a SPhP mode bounded to the interfaces of a 1 μm thick suspended SiO$_2$ membrane. The result is obtained by FDTD numerical simulations by using the excitation frequency $\nu = 1050$ cm^{-1} where the relative permittivity of SiO$_2$ satisfies the SPhP condition ($\epsilon_r < -\epsilon_{air} = -1$). The blue rectangle indicates the position of the SiO$_2$ membrane.*

We have tested the algorithm on a 1 μm thick suspended SiO$_2$ membrane and compared the FDTD predictions to the theoretical results obtained for this membrane in the section 7.4.2. The energy density distribution for the typical SPhP frequency $\nu = 1050$ cm^{-1} where the permittivity condition $\epsilon_r < -\epsilon_{air} = -1$ is satisfied is shown on the Figure 6.1. The size of the computational cell has been chosen to be large enough to avoid any interaction of the bounded mode with the Perfectly Matched Layer (PML) and to exceed the propagation length of the mode. In this case, the cell is chosen to be 40 μm by 200 μm in thickness and width, respectively, and the thickness of the Gaussian excitation source is chosen to be $\sigma = 5$ μm centered in the middle of the membrane. The spatial size of the excitation source has been chosen to be small enough to avoid the excitation of the far-field modes but large enough to limit a self diffraction. The plotting area is of course chosen to be smaller than the computation cell to avoid plotting PML. The minimum computational spatial resolution was set to be at least 10 points per 1 μm increasing up to 20 points for higher

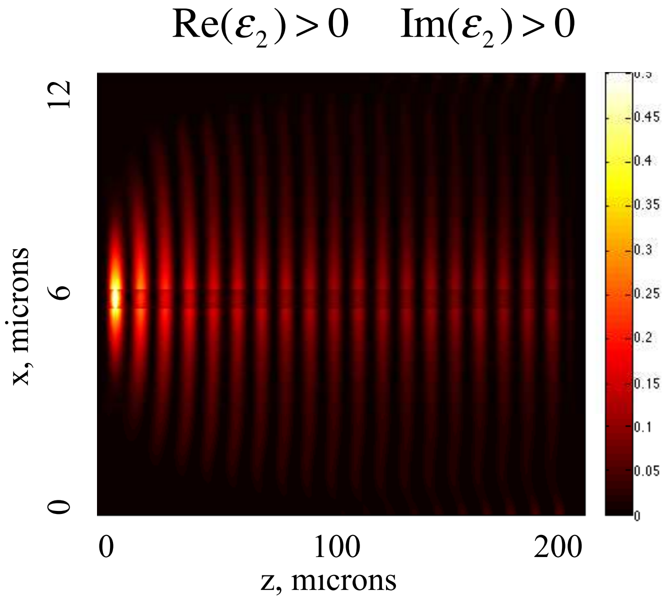

Figure 6.3: *Energy density plot of a Zenneck mode bounded to the interfaces of 1 μm thick suspended SiO$_2$ membrane. The result is obtain by FDTD numerical simulations by using the excitation frequency $\nu = 900$ cm^{-1} where the relative permittivity of SiO$_2$ satisfies Zenneck mode condition ($\epsilon_r > 0$ and $\epsilon_i > 0$).*

excitation frequencies. We can also analyze the profile of this mode by plotting the absolute value of its Poynting vector along the x axis as shown on the Figure 6.2. The energy is concentrated near the interface of the membrane and exponentially decaying in both directions away from the interface. Note that such a behaviour is typical for any polariton and it guarantees that the mode is bounded to the interfaces of the membrane. It should also be mentioned that the field almost completely vanishes at distances about one wavelength far from the interfaces.

Similar analysis can also be done for frequencies being out of the SPhP region: for Zenneck and TM guided regions where the dielectric function of SiO$_2$ satisfies the conditions ($\epsilon_r > 0$ and $\epsilon_i > 0$) and ($\epsilon_r > 0$ and $\epsilon_i \approx 0$) respectively. The energy density plots for Zenneck and TM guided regions are shown on Figure 6.3 and Figure 6.4 respectively by changing the excitation source frequency in numerical simulations to $\nu = 900$ cm^{-1} and $\nu = 2500$ cm^{-1} respectively.

The energy density of Zenneck modes in 1 μm thick suspended SiO$_2$ membrane shown on Figure 6.3 demonstrates significantly larger propagation along the membrane. The electromagnetic field of course penetrates inside the membrane and this fact together with a comparatively large absorption of SiO$_2$ for this frequency is the main limitation factor of propagation of this mode. With the decrease of the membrane thickness, the ratio of the absorbed energy to the energy propagating along the interface should be lower leading to the increase of the propagation of the mode along the membrane as predicted by the theory in the chapter 5. At the same time, the absorption of SiO_2 is caused by the strong interaction of the electromagnetic field with optical phonons inside the lattice. This feature is important for using such materials for various thermal applications such as the in-plane thermal conductivity increase. It can also be noticed that the energy density of this mode drops down significantly in the direction perpendicular to the membrane similarly to the case of polaritons. This ensures that the mode is not radiated but bounded to the interfaces of the membrane.

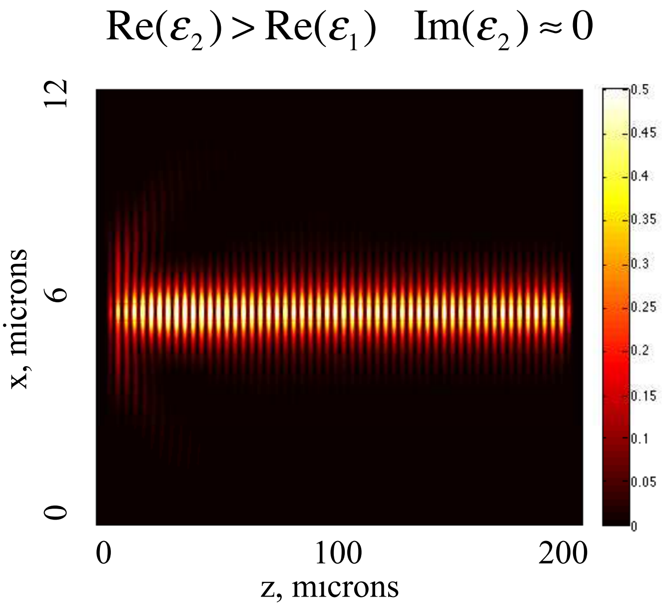

Figure 6.4: *Energy density plot of a TM guided mode bounded to the interfaces of a 1 μm thick suspended SiO_2 membrane. The result is obtained by FDTD numerical simulations by using the excitation frequency $\nu = 2500$ cm^{-1} where the relative permittivity of SiO_2 satisfies TM guided mode conditions ($\epsilon_r > 0$ and $\epsilon_i \approx 0$). The scale is in arbitrary units.*

In the case of very low absorption and positive real part of the relative permittivity of SiO_2 (TM guided mode) the mode propagates almost without losses as is shown on Figure 6.4. The fact that this mode has such a long propagation is a very interesting feature. Simultaneously, there is almost no absorption inside the membrane due to the fact that there are no optical phonons which can absorb electromagnetic radiation in this particular dielectric. And because of Kirchhoff's law of thermal radiation, spectral emission and absorption are equal. Hence, those modes cannot be excited thermally. However, it can be done by adding an emissive material to the system. Also note that this TM guided mode is well bounded to the membrane and the energy is mostly concentrated inside the membrane contrary the case of the polaritonic mode where most of the energy is propagating close to the interface outside of the membrane.

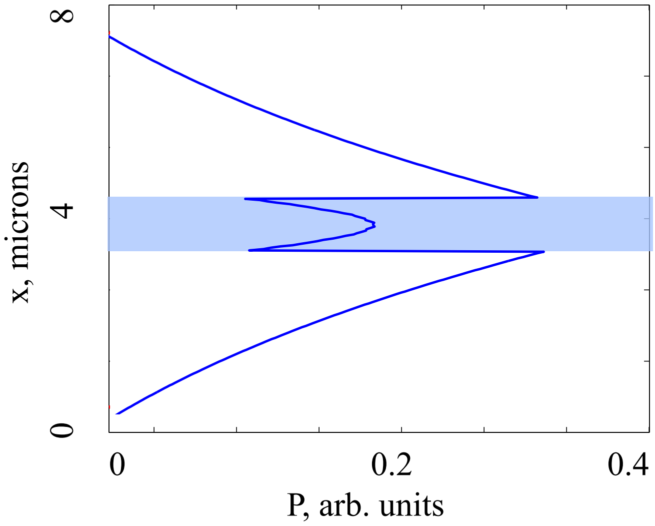

Figure 6.5: *Energy density profile along the x axis of a Zenneck mode bounded to the interfaces of a 1 μm thick suspended* SiO_2 *membrane. The result is obtained by FDTD numerical simulations by using the excitation frequency* $\nu = 900$ cm^{-1} *where the relative permittivity of* SiO_2 *satisfies Zenneck mode condition* ($\epsilon_r > 0$ *and* $\epsilon_i > 0$)*. The scale is in arbitrary units.*

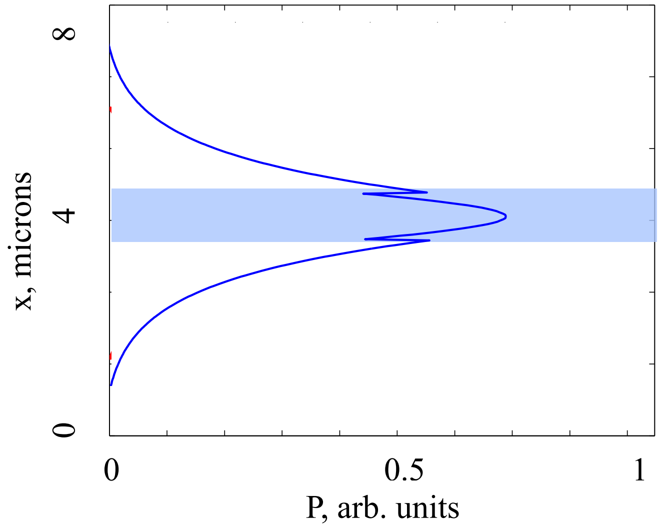

Figure 6.6: *Energy density profile along the x axis of a TM guided mode bounded to the interfaces of a 1 μm thick suspended* SiO_2 *membrane. The result is obtained by FDTD numerical simulations by using the excitation frequency* $\nu = 2500$ cm^{-1} *where the relative permittivity of* SiO_2 *satisfies TM guided mode condition* ($\epsilon_r > 0$ *and* $\epsilon_i \approx 0$)*.*

In order to understand the difference between Zenneck and TM guided modes, one needs to compare the energy density profiles of these modes shown on Figure 6.5 and Figure 6.6 respectively, by considering a slice of the energy density for a fixed value of z along the x axis. In the case of Zenneck mode, the energy is mostly propagating outside of the membrane similarly to polaritons due to the significant absorption inside the membrane. There is also an increase of the energy density in the center of the membrane similarly to the case of TM guided modes but with lower intensity as the Zenneck mode can be considered as an intermediate mode between the polaritonic and TM-guided cases. The profile of the energy density of the TM guided mode reveals that the energy is propagating mostly inside the membrane as predicted by the theory in the chapter 5.

6.1.2 FDTD numerical results for a 0.5 μm thick SiO$_2$ film deposited on aluminum

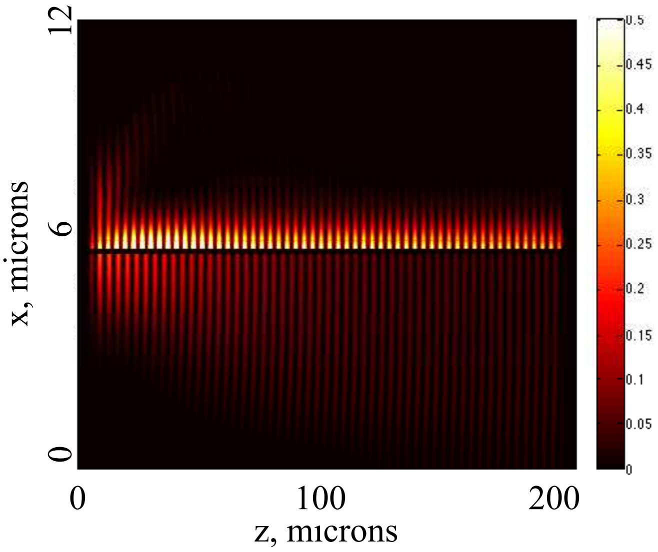

Figure 6.7: *Energy density plot of a TM guided mode bounded to the interfaces of a 0.5 μm thick SiO$_2$ film deposited on the top of 0.25 μm thick aluminum layer. The result is obtained by FDTD numerical simulations by using the excitation frequency $\nu = 2500$ cm^{-1} where the relative permittivity of SiO$_2$ satisfies TM guided mode conditions ($\epsilon_r > 0$ and $\epsilon_i \approx 0$). The scale is in arbitary units.*

After verifying the numerical model for the simple case of a 1 μm thick suspended SiO$_2$ membrane, the same code can be used to compute the electromagnetic field distribution for a slightly different geometry. As has been mentioned earlier in this chapter, the fabrication of a suspended large SiO$_2$ membrane remains complicated and an electromagnetically equivalent system can be created by using a metallic mirror. Indeed, if the excitation frequency is small enough (compared to the plasma frequency in metal) similar to the method of images in electrostatic approximation one can design a structure consisting of a metallic substrate and a SiO_2 thin layer deposited on its surface with a thickness of 0.5 μm being twice thinner than the equivalent 1 μm thick suspended SiO_2 membrane. Instead of a metallic substrate, a thin layer of metal can be used if thicker than the maximum penetration depth of the field inside the metal. In our case, we have chosen an aluminum layer of thickness $d_{Al} = 0.25$ μm being thick enough to behave like an electromagnetic mirror in this case. We have chosen aluminum out of all possible metals because it provides a strong mechanical contact between glass and silicon and it is one of the most common material for infrared optics. The equivalence of these two systems can be simply checked by running a FDTD numerical simulation using exactly the same parameters for this new geometry.

Figure 6.7 shows the result of the FDTD simulation for an excitation frequency $\nu = 2500$ cm^{-1} being in the TM guided region. The upper half part of the plot shows exactly the same behaviour as the one of a 1 μm thick suspended SiO_2 membrane shown on Figure 6.4. The bottom half part of the plot shows the propagation of weakly coupled plasmons along the aluminum interface with the wave vector being very close to the one of vacuum. Note that the wave vector of the mode in the upper half of the plot is not the same as the one of the bottom half, as in the first case the wave vector is driven by the glass dispersion.

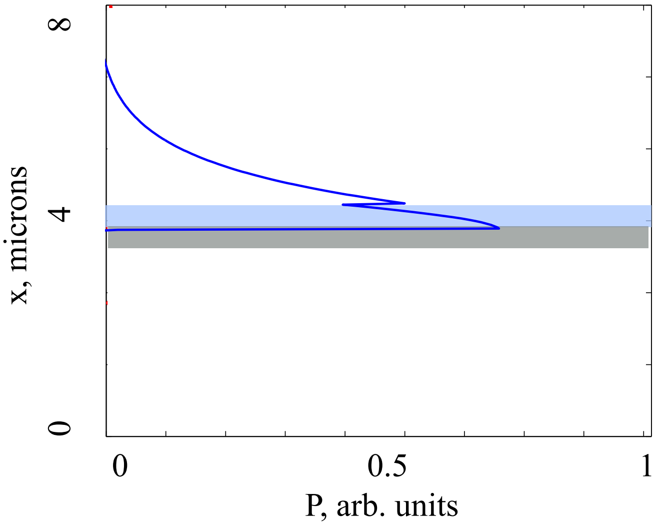

Figure 6.8: *Energy density profile along the x axis of a TM guided mode bounded to the interfaces of a 0.5 μm thick SiO_2 film deposited on the top of a 0.25 μm thick aluminum layer. The result is obtained by FDTD numerical simulations by using the excitation frequency $\nu = 2500$ cm^{-1} where the relative permittivity of SiO_2 satisfies the TM guided mode conditions ($\epsilon_r > 0$ and $\epsilon_i \approx 0$). The gray region indicates the position of aluminum, the blue region indicates the position of the 0.5 μm thick SiO_2 film.*

Figure 6.8 shows the energy density profile of a TM guided mode in this geometry. It is superimposed with the one reported previously for a 1 μm thick suspended SiO_2 membrane in the upper half shown on Figure 6.6. The fact that the two profiles are superimposed proves that these two systems are equivalent for this frequency.

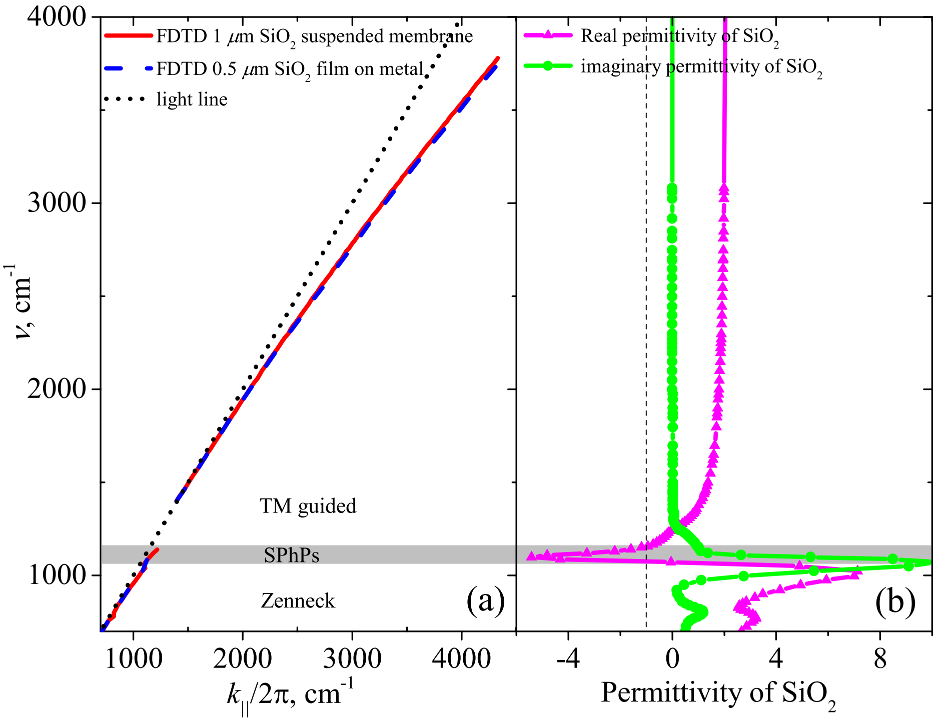

Figure 6.9: *(a) Dispersion relations obtained by running series of FDTD numerical simulations over different excitation frequencies for a 1 μm thick suspended SiO_2 membrane (red line) and a 0.5 μm thick SiO_2 film deposited on the top of a 0.25 μm thick aluminum layer (blue dashed line). The dispersions are superimposed in all the frequency range indicating the electromagnetic equivalence of the two structures. (b) Real (magenta line) and imaginary (green line) parts of the relative permittivity of SiO_2 used in the FDTD simulations.*

In order to extend this approach to all the frequencies of interest and to compare the dispersion relations of the long-range surface modes supported by these two equivalent structures, we have introduced a loop over the excitation frequencies to perform a series of numerical simulations for all the excitation frequencies from 750 cm^{-1} to 4000 cm^{-1}. The obtained electromagnetic field distribution is then post-treated and the propagation length as well as the in-plane wave vector are obtained by fitting the numerical data. The resulting dispersion relations for both systems (1 μm thick suspended SiO_2 membrane and 0.5 μm thick SiO_2 film deposited on the top of a 0.25 μm thick aluminum layer) are shown on Figure 6.9(a). They are almost superimposed in all the frequency region and the slight difference can be explained by the fitting algorithm and FDTD uncertainties. Figure 6.9(b) shows the real and imaginary parts of the relative permittivity of SiO_2 used for the FDTD model and indicates the frequency regions of different types of surface modes. These numerical results provide the proof that these two systems are electromagnetically equivalent in all the frequency range and that the 0.5 μm thick SiO_2 film deposited on the top of a 0.25 μm thick aluminum layer can be considered instead of a 1 μm thick suspended SiO_2 membrane.

6.2 Sample fabrication

6.2.1 Sample design

The numerical results demonstrated in the section above open the possibility of a practical fabrication of a sample that can be used to diffract thermally excited electromagnetic surface waves by a grating. We analyzed previous works done by different groups to diffract thermal energy by two-dimensional gratings Marquier, Joulain, Mulet, Carminati, Greffet, and Chen (2004); Joulain, Mulet, Marquier, Carminati, and Greffet (2005); Greffet, Carminati, Joulain, Mulet, Mainguy, and Chen (2002) and defined the period of the grating to be $\Lambda = 9.26$ μm, the grating depth $d = 0.5$ μm, the filling factor FF$= 0.5$, and the lateral size of the grating of 1 cm to be at least one order of magnitude larger than the maximum propagation length of the mode provided by the theory in the chapter 5. Taking into account the filling factor of the grating, the thickness of the SiO_2 layer with the grating is chosen to be 0.75 μm to effectively correspond to the $d = 0.5$ μm thick SiO_2 film deposited on the metallic layer which is electromagnetically equivalent to a 1 μm thick suspended SiO_2 membrane. In fact, these values of the filling factor and of the etching depth of the grating have been chosen to maximize the diffraction efficiency of the grating. The period of the grating has been chosen to be small enough to be able to diffract low frequency Zenneck modes but at the same time, we wanted to minimize the number of diffraction orders of the grating by using the largest period. We have also fabricated several gratings with slightly different periods in order to verify the experimental results. The sample discussed here is shown on Figure 6.10. Note that we used a 0.25 μm thick aluminum layer deposited on a silicon undoped wafer to act as an electromagnetic mirror according to the results of our numerical model demonstrated in the previous section. We also needed to have a large flat surface of the same thickness of SiO_2 on the same wafer in order to be able to perform normalization measurements in FTIR far field emission regime.

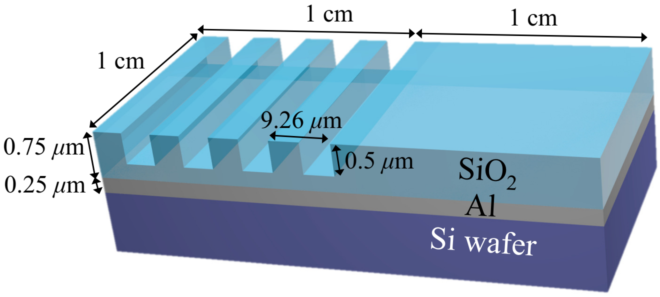

Figure 6.10: *Sample design for far-field detection of a coherent thermal emission due to thermally excited long-range surface waves.*

6.2.2 Checking the dielectric function of glass

Fabrication of such a structure can be done by applying standard clean-room technological processes such as various thin film deposition techniques, e-beam or optical lithography processes, and Reactive Ion Etching (RIE). Depending on SiO_2 deposition techniques, the dielectric function of the resulting SiO_2 film can be slightly different as it depends on the typical size of the crystalline structures and other micro parameters of the deposited layer. We have used two deposition technologies available and we need to pick up the one providing the material with the most resonant dielectric function in order to observe a strong SPhP signal. For this purpose, we have directly deposited thin layers of SiO_2 on two Si wafers (without Al layer) with sputtering and Plasma Enhanced Chemical Vapor Deposition (PECVD) processes and analyzed their reflectivity spectra.

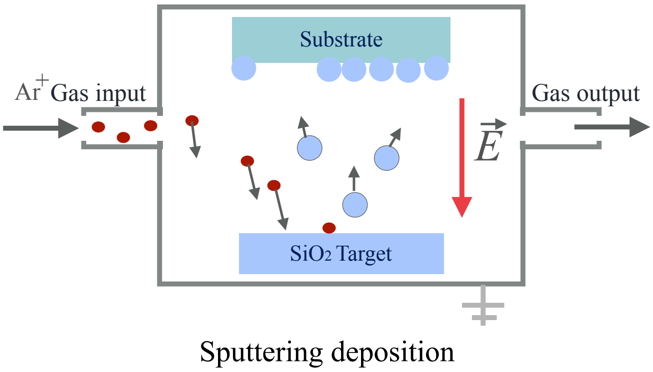

Figure 6.11: *Schematic of the sputtering deposition process of a thin SiO_2 layer. Red particles are Ar positive ions.*

Sputtering deposition of SiO_2 is a comparatively slow and expensive process which is a physical vapor deposition (PVD) method of thin film. It involves ejecting material from a target that is referred to as a source, on a substrate.

For example, Ar ions are accelerated by an electrostatic field inside the chamber and hit the SiO_2 target. These collisions produce particles of the target going in the direction of the substrate and forming a thin layer of SiO_2 on the top of it. Figure 6.11 illustrates this process. The advantage of this method is a high smoothness and an uniform thickness of the layer as well as a growth at low temperatures. However, the deposition rate is comparatively slow and this method is usually more expensive than other alternative methods of SiO_2 deposition.

Another technique that we used to obtain a thin layer of SiO_2 is PECVD. This is basically a chemical vapor deposition process used to deposit various thin films from a gas state to a solid state on a surface of a substrate involving radio frequency plasma. The schematic illustration is shown on Figure 6.12. The growing rates of PECVD methods are usually higher than in the case of sputtering processes but they provide significantly larger roughness and lower purity of the films.

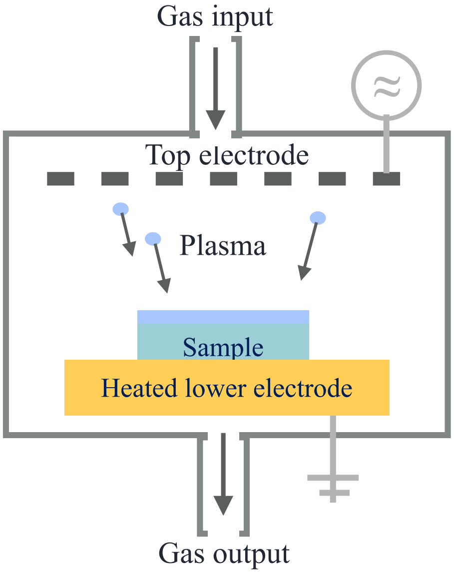

Figure 6.12: *Illustration of the Plasma Enhanced Chemical Vapor Deposition (PECVD) process of a thin SiO_2 layer.*

In order to select the most appropriate deposition technique for our sample fabrication, we analyzed the infrared reflectivity signal obtained by the FTIR setup discussed in details in the chapter 7. The experimental results obtained are shown on Figure 6.13. The data is obtained by using an infrared reflector Cassegrain microscope objective which collects signal on a wide range of incidence angles and therefore a direct Kramers-Kronig analysis de L. Kronig (1926) cannot be applied to obtain the relative permittivity of deposited SiO_2. However, the information about the dielectric function of the film can be analyzed indirectly by considering the position and the intensity of the reflectivity peak.

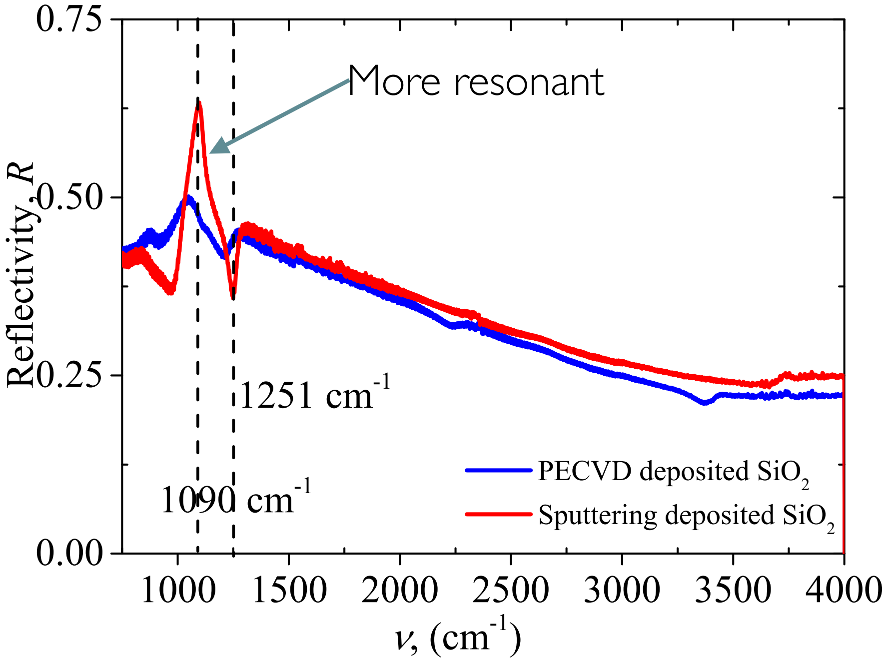

Figure 6.13: *Infrared spectral reflectivity measurement of a 0.5 μm thick SiO_2 layer deposited on an undoped Si wafer by sputtering and PECVD processes.*

In the case of sputtering deposited SiO_2 film, the reflectivity peak is significantly sharper indicating a strong nonlinearity of the dielectric function, which should provide a stronger SphP signal. It should also be noted that the dips in the spectra correspond to the high absorption values of the material due to the longitudinal and transverse modes of optical phonons. Such a difference between the two types of deposition technique can be explained by the fact that the fastly growing methods such as PECVD cannot provide the same amount of purity and uniformity compared to the sputtering method. During the deposition process of SiO_2 film with the PECVD method, the temperature is significantly higher than in the case of sputtering resulting in a different micro structure and as a result, less resonant values of the dielectric function.

In the chapter 5, we used the dielectric function of SiO_2 obtained from the experimental values of the reflectivity reported in the literature Palik (1985). In order to check if the dielectric function of our sputtering deposited SiO_2 film can be assumed to be the same as in our previous theoretical and numerical results, we ran a numerical FDTD simulations to obtain spectral transmission, reflection and absorption of a 0.5 μm thick SiO_2 layer deposited on an undoped Si wafer. The results of the simulations together with the experimental ones are shown on Figure 6.14. The fact that the experimental reflectivity behaves similarly to the one obtained in the FDTD model is an evidence that the dielectric function of SiO_2 used in the numerical model is almost the same as the one of the SiO_2 film obtained with the sputtering deposition.

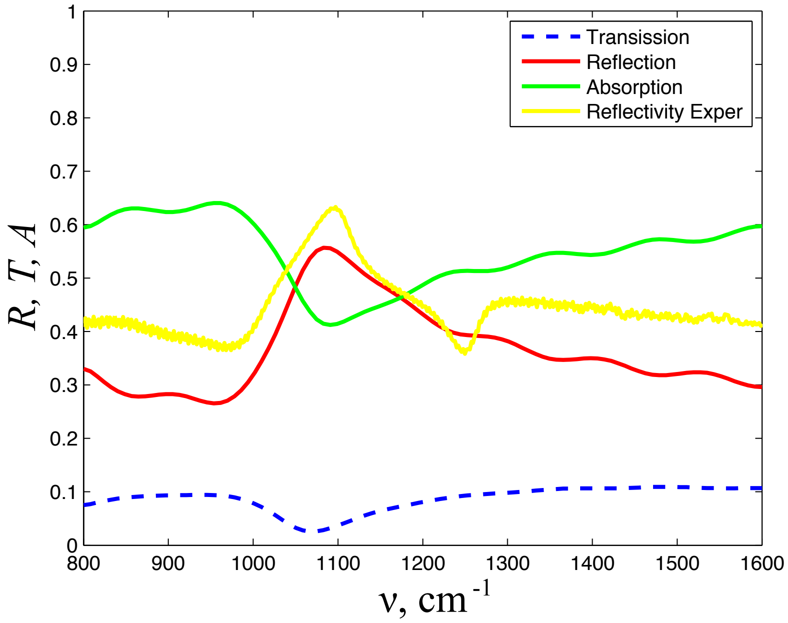

Figure 6.14: *FDTD numerical results of the transmission (dashed blue line), reflection (red line) and absorption (green line) of a 0.5 μm thick* SiO_2 *layer deposited on an undoped Si wafer compared with the experimental data obtained by FTIR reflectivity measurements (yellow line) of a sample produced by sputtering deposition of a 0.5 μm thick* SiO_2 *layer on an undoped Si wafer.*

Note that the simulations performed here are completely different from the ones that we used before in section 6.1. In the present case, we have developed a code to obtain the spectral reflectivity, absorption, and transmission in a single run by considering a plane broadband short pulse source illuminating the film from one side and by Fourier-transforming the response of this pulse in regions from both sides of the wafer with the SiO_2 film. However, in order to normalize the obtained spectra, we used exactly the same single run in simulation in an empty computation cell without wafer. This is a standard technique of MEEP FDTD code Oskooi, Roundy, Ibanescu, Bermel, Joannopoulos, and Johnson (2010) which provides transmission, reflection and absorption spectra for any geometry of the sample containing dispersive materials. The numerical error can be estimated by subtracting reflection, absorption and transmission from the unity. In our case the numerical error is smaller than 0.1% in the working frequency range.

We have also verified if the dielectric constant is changing after annealing the sample. We repeated the experimental measurement of the reflectivity of the sputtering deposited SiO_2 layer for various temperatures (up to 700 K) and the spectra were almost superimposed. This is a very important feature demonstrating that the same dielectric constant can be used in our temperature range.

6.2.3 Steps of clean room fabrication

The results discussed above lead to the following steps of fabrication shown on Figure 6.15 and Figure 6.16.

(a) CVD deposition of Al

(b) Deposition of glass

Figure 6.15: *Fabrication stages of a sample without a diffraction grating. (a) Chemical vapor deposition of a 0.25 μm thick aluminim layer; (b) sputtering deposition of a 0.75 μm thick layer of* SiO_2.

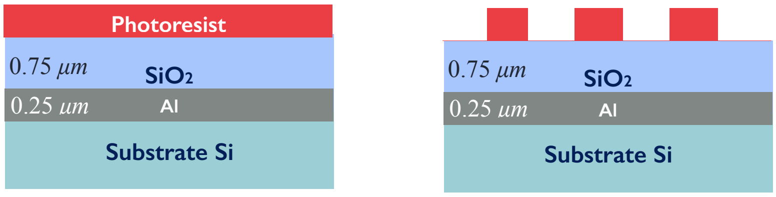

(a) Deposition of Photoresist

(b) UV lithography

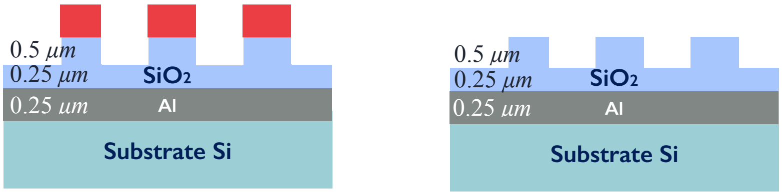

(c) Reactive Ion Etching of glass 0.5 μm

(d) Removing Photoresist

Figure 6.16: *Fabrication steps of a diffraction grating. (a) Deposition of optical photoresist with spincoating method; (b) UV lithography with a hard contact with the mask; (c) directive reactive ion etching of* SiO_2*; (d) photoresist cleaning with RIE method.*

We first deposit a 0.25 μm thick layer of aluminum on a polished surface of an undoped Si wafer. We used a chemical vapor deposition (CVD) technique for this purpose as shown on Figure 6.15(b). Right after the deposition of metal, we used a sputtering process to deposit a 0.75 μm thick SiO_2 layer. The deposition of SiO_2 was done fast enough to avoid any oxidation of the metal which itself guarantees the mechanical stability of the aluminum-SiO_2 interface.

The diffraction grating that we want to deposit on the top of this sample has comparatively deep grooves. Standard e-beam lithography with Reactive Ion Etching (RIE) cannot be used as the photoresist because it is not resistive enough to achieve a 0.5 μm etching depth of SiO_2. An alternative way is to use a standard UV lithography process as the photoresist used for this process is resistive enough to perform a 0.5 μm depth RIE of the SiO_2 film. Figure 6.16 shows the steps required to fabricate a diffraction grating.

In fact, there are two types of UV lithography and depending if it is a negative or positive lithography process, one can obtain gratings with filling factors slightly different from the one of the original hard mask. The schematic of the UV exposure of the photoresist is shown on Figure 6.17(a). In the case of negative optical lithography, the parts of the photoresist which are not exposed to the UV light are removed. In fact, the period of the grating $\Lambda = 9.26$ μm is comparatively small compared to the typical sizes of the details usually obtained by this kind of technology. Also note that the diffraction of the UV light also has a significant influence on the resulting pattern. Taking these two facts into account, we can assume that the filling factor of the photoresist pattern should be slightly larger than the expected 0.5 value as shown on Figure 6.17(b). When positive optical lithography is used, the photoresist is removed only in the regions where it is exposed to UV light, leading to a smaller filling factor of the photoresist mask as demonstrated on Figure 6.17(c). We decided to use negative UV lithography as it provided sharper edges of the mask and resulted in a better performance of the diffraction grating during the optical characterizations.

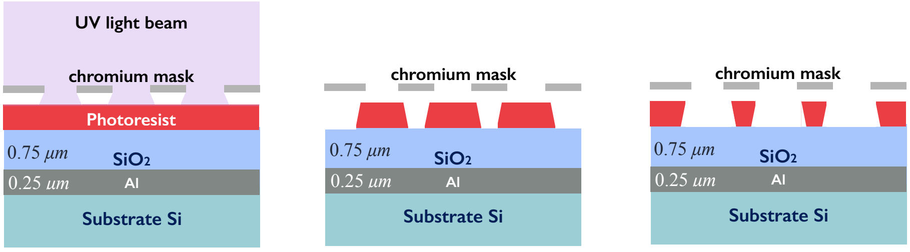

(a) UV exposure (b) Negative UV lithography (c) Positive UV lithography

Figure 6.17: *Demonstration of UV exposure of an optical photoresist (a). Comparison between negative (b) and positive (c) UV lithography methods.*

It is also important to mention that when the RIE is applied to the photoresit mask obtained by the UV lithography, the filling factor of the resulting SiO_2 structure is even larger because the etching process is not perfectly directive. This is shown in Figure 6.18(a) and Figure 6.18(b) for negative and positive UV lithography respectively. Note that both Figure 6.17 and Figure 6.18 are just schematic demonstrations of the processes and the real filing factor of diffraction grating driven by these two physical processes is usually just slightly different from the 0.5 value.

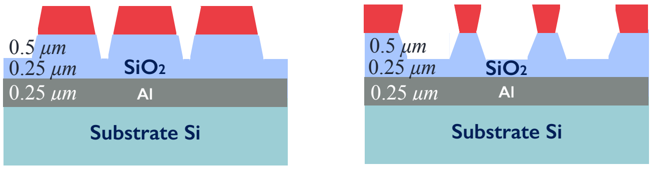

(a) Negative UV lithography

(b) Positive UV lithography

Figure 6.18: *Schematics of the results from directive RIE method applied to the samples with photoresist obtained by negative (a) and positive (b) UV lithography.*

Following the same fabrication steps as described above, we have fabricated the samples shown on Figure 6.19 with different periods ($\Lambda = 9.26$ μm, $\Lambda = 10.82$ μm, $\Lambda = 11.50$ μm) and a sample without metallic deposition but with a 2 μm thick layer of SiO_2 with exactly the same diffraction grating etched on the top of SiO_2 layer. The purpose of this sample was to check the single interface geometry case and to verify our experimental approach. In fact, a thickness of 2 μm is not enough for the layer to be equivalent to a single interface as has been shown in the chapter 5. However, the sample behaves very similarly to the single interface geometry case for frequencies close to the ones of SPhPs due to the fact that there is no effect of a metallic mirror and the layer of SiO_2 is thick enough to absorb most of the field penetrating inside the sample.

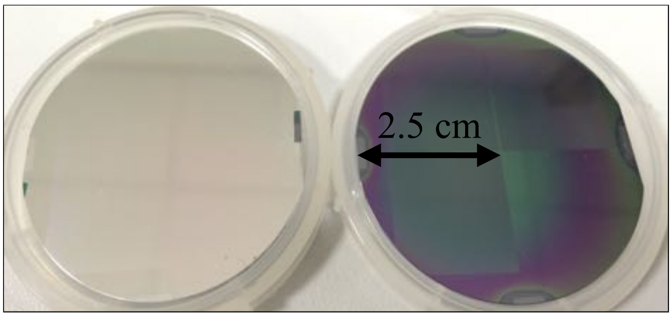

Figure 6.19: *Samples fabricated on silicon wafer with aluminum deposition (left sample) and without aluminum layer but thicker SiO_2 (right sample).*

Note that each wafer contains three diffraction gratings with different periods and one flat region used for normalization of the emission signal. The lateral size of each grating is around 2.5 cm to avoid any finite size effects.

6.3 Emission FTIR spectroscopy measurements

6.3.1 Principles of Emission FTIR spectroscopy

We used Fourier Transform Infrared emission spectroscopy to characterize the far-field thermal emission of the sample that was fabricated in the section above. The emission measurements are more complicated than reflectivity measurements discussed in details in the chapter 7 but the principle is similar and has been described in the literature Griffiths, Haseth, and Winefordner (2007). We use a standard FTIR spectrometer Nicolet 6700 equipped with a MCT-A detector operating at liquid nitrogen temperature. Figure 6.20 represents how the thermal emission of the sample is collected. The sample is placed on a heating stage designed to maintain a certain surface temperature of the sample with a precision of 1 K. The heating stage itself is placed on a tilt stage allowing smooth variation of the observation tilt angle of the sample with a precision of 0.5°. The collected sample emission over an area of 1 cm^2 is delivered to the FTIR spectrometer through a diaphragm and a KRS-5 holographic wire grid infrared polarizer which provides excellent transmission in the working frequency range (from 700 cm^{-1} to 4000 cm^{-1}). The role of the diaphragm is to limit the solid angle of thermal emission collection in order to lower the broadening of the grating emission peaks. The polarizer orientation can be changed in order to examine thermal emission in both TM and TE polarizations. The sample was usually heated up to the highest possible temperature to provide the best signal, and a spectral resolution of 1 cm^{-1} was used for most of the experiments with an average number of scans being between 256 and 128 with and without the polarizer respectively.

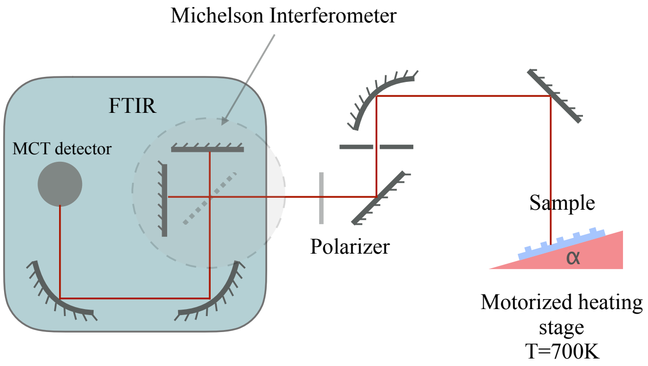

Figure 6.20: *Schematic of the FTIR emission setup and the optical path of the emitted infrared signal of the sample.*

Figure 6.21 shows a typical emission signal obtained when the sample surface is heated up to $T = 673$ K. The complexity of the emission spectroscopy is that the emission signal is usually small compared to the background signal. The background radiation is also not constant in time and depends on many factors. In order to characterize only the emission of the sample, the background radiation should be constantly monitored and subtracted from the sample emission signal. The difference of emission obtained from the surface of the sample and from the background signal normalized by the emission collected from a blackbody at the same temperature as the one of sample should yield the emissivity. This strategy is commonly used in such experiments Greffet, Carminati, Joulain, Mulet, Mainguy, and Chen (2002); Marquier, Joulain, Mulet, Carminati, Greffet, and Chen (2004); Joulain, Mulet, Marquier, Carminati, and Greffet (2005).

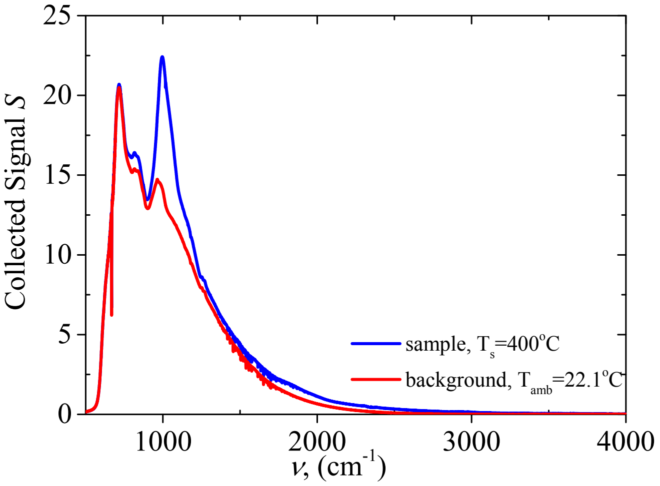

Figure 6.21: *Comparison of background signals collected by FTIR emission spectroscopy setup from the background at room temperature (red curve) with an emission signal coming from a sample heated up to* $T = 673$ K= 400°C *(blue curve).*

6.3.2 Normalized Emission Spectra

The emissivity is usually used to characterize the material but in our case the modification of the emission signal is caused by the geometry of the surface and it is better to use another characteristic of the emission, which does not depend on the material itself but only on the geometry. Such a method has been used in the literature to characterize the emission of nanostructures Schuller, Taubner, and Brongersma (2009). We first collect the emission signal from the surface of the diffraction grating and then from the flat surface of the sample under exactly the same conditions (surface temperature, observation angle, same optical path). The background signal is then subtracted from both diffraction grating and flat region emission spectra and the ratio is calculated as follows:

$$S_{gr}^{exp}(\nu, T_s, \alpha) = \frac{S_{gr}(\nu, T_s, \alpha) - S_{bg}(\nu)}{S_{fl}(\nu, T_s, \alpha) - S_{bg}(\nu)}, \tag{6.1}$$

where T_s is the sample surface temperature and α is the tilt angle. Note that this emission signal $S_{gr}^{exp}(\nu, T_s, \alpha)$ is not the same as emissivity as it also features the influence of the topography of the sample on its emission. The normalized spectrum value reduces to unity for any frequency where the grating has no impact on the sample emission. Fig. 6.22 shows this normalized emission spectrum obtained from our two samples (thin layer of SiO_2 deposited on aluminum layer and thick layer of SiO_2 without aluminum layer) for $T_s = 673$ K and a tilt angle $\alpha = 2.6°$ with a diffraction grating period $\Lambda = 9.26$ μm. Note that the normalized grating emission signal of the sample with the thick layer of SiO_2 is flat in most of the spectrum indicating the equivalence of the emission signal obtained from the diffraction grating and a flat surface of the sample. The sample with the thin layer of SiO_2 deposited on the aluminum film has sharp peaks which are the diffraction orders of the grating. These diffraction peaks are clear signatures of coherent thermal emission. There are also some oscillations of the signal which do not originate from the diffraction by the grating and they are observed due to the different SiO_2 effective thicknesses in the grating and flat regions of the sample.

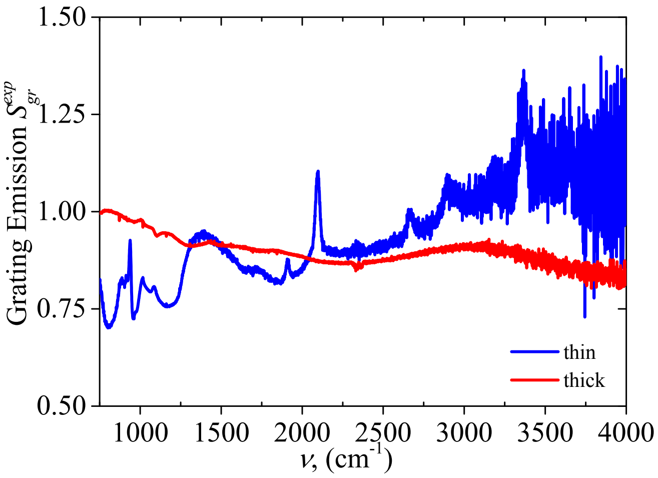

Figure 6.22: *Comparison of normalized emission spectra obtained from the diffraction grating etched on 0.75 μm thick SiO_2 film deposited on an aluminum layer (blue curve) and from the diffraction grating etched on a 2 μm thick SiO_2 film without aluminum layer.*

We then examine the polarization of the grating emission since the diffraction peaks can only exist for transverse magnetic polarization if they originate from surface waves Yang, Sambles, and Bradberry (1991); John Polo (2013). Figures 6.23(a, c, e) show the grating emission peaks observed by collecting emission signal from the grating with $\Lambda = 9.26$ μm on SiO_2 thin film deposited on aluminum substrate heated up to $T = 673$ K in three different frequency regions. In all these regions the emission peaks disappear for TE polarized signals as expected.

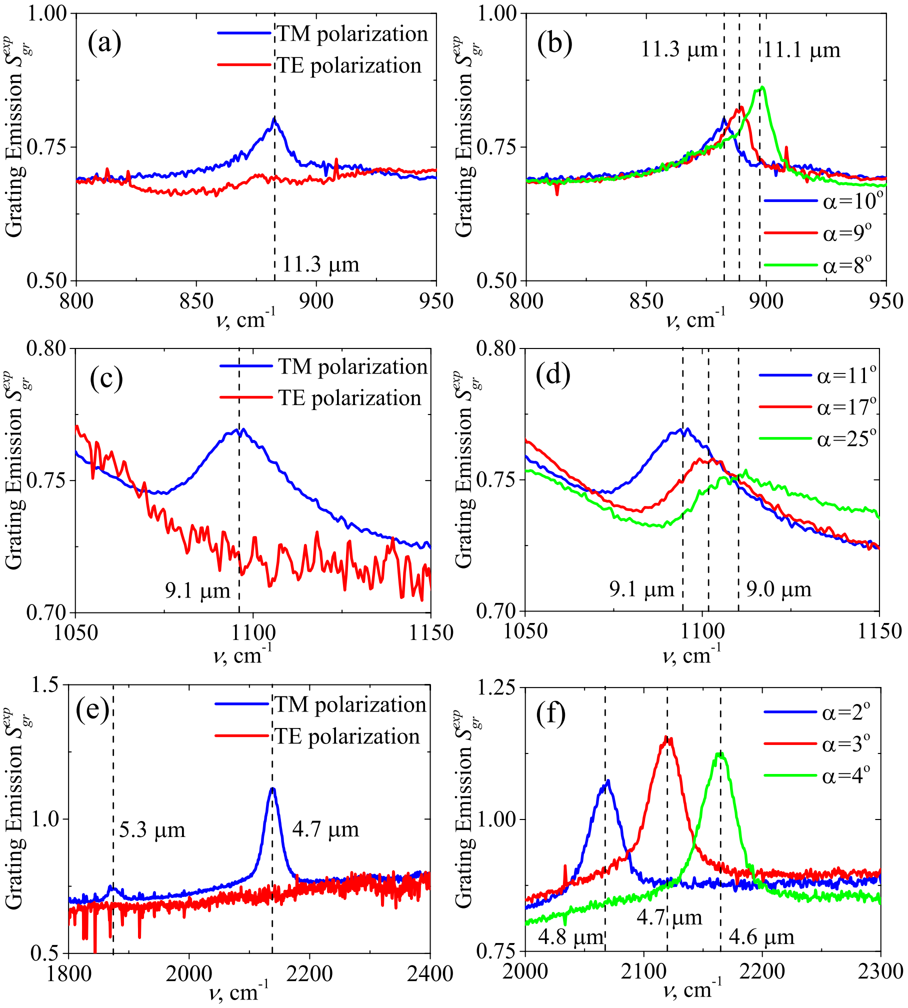

Figure 6.23: *Emission signal of the SiO_2 grating deposited on aluminum in TE and TM polarizations (left) and for different tilt angles (right). Figures (a) and (b): Zenneck region ($\epsilon_r > 0$, $\epsilon_i > 0$). Figures (c) and (d): Surface Phonon Polariton region ($\epsilon_r < -\epsilon_{air}$). Figures (e) and (f): subwavelength TM guided mode region ($\epsilon_r > 0$, $\epsilon_i \approx 0$).*

These frequency regions indicate different surface modes according to the values of the relative permittivity of glass as predicted by theory and numerical results on Figure 5.7 and Figure 6.9 respectively. These are Zenneck surface modes ($\epsilon_r > 0$, $\epsilon_i > 0$), Surface Phonon Polaritons ($\epsilon_r < -\epsilon_{\text{air}}$), and subwavelength TM guided modes ($\epsilon_r > 0$, $\epsilon_i \approx 0$) according to the classification of surface electromagnetic modes in thin dielectric films Yang, Sambles, and Bradberry (1991) John Polo (2013). Detection of Zenneck surface modes in a single interface system for these frequencies is usually not possible due to their short propagation length Yang, Sambles, and Bradberry (1991) while a thin film supports long-range Zenneck modes allowing for their diffraction by the grating. Figure 6.23(e) shows the existence of thermally excited subwavelength TM guided modes over a broad frequency range around $\nu = 2000$ cm^{-1} where the absorption is almost equal to zero.

Figures 6.23(b,d,f) demonstrate the frequency shift of the emission peaks when the tilt angle α is varied. This is of course a signature of the grating diffraction of thermal emission due to the presence of long-range surface modes according to the grating equation:

$$\frac{\omega}{c}\sin\alpha = k_{||} + m\frac{2\pi}{\Lambda}, \quad m \in \mathbb{Z}, \tag{6.2}$$

where $k_{||}$ is the in-plane wavevector and m is the diffraction order. In order to reconstruct the dispersion relation and propagation length of these modes, we have developed an algorithm which finds the peaks on the spectra and fits them with Gaussian function. The demonstration of this fitting process is shown on Figure 6.24. By applying this algorithm for normalized emission spectra obtained for different tilt angles of the gratings, one can define the central frequency of the peak and the Full Width at Half Maximum (FWHM) and their standard deviation values.

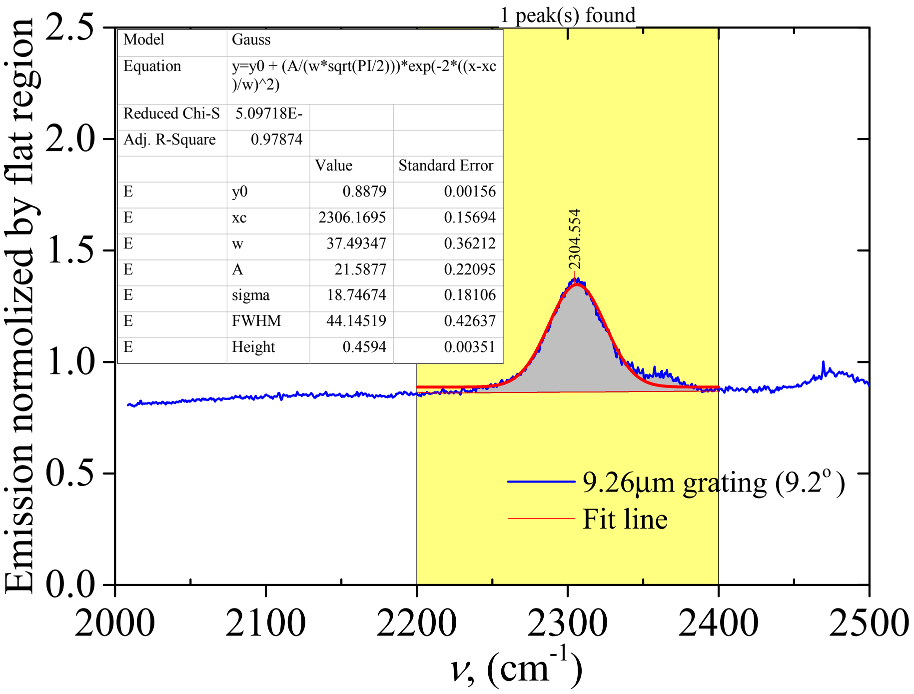

Model	Gauss		
Equation	y=y0 + (A/(w*sqrt(PI/2)))*exp(-2*((x-xc)/w)^2)		
Reduced Chi-S	5.09718E-		
Adj. R-Square	0.97874		
		Value	Standard Error
E	y0	0.8879	0.00156
E	xc	2306.1695	0.15694
E	w	37.49347	0.36212
E	A	21.5877	0.22095
E	sigma	18.74674	0.18106
E	FWHM	44.14519	0.42637
E	Height	0.4594	0.00351

Figure 6.24: *Demonstration of the finding and fitting of the diffraction grating peaks with a Gaussian function.*

6.3.3 Experimental Dispersion Relation of Surface Modes

Applying Equation 6.2 to the results provided by the fitting algorithm, one can obtain the folded dispersion relation of the surface waves as shown Figure 6.25. In order to obtain the usual dispersion relation of surface waves, the procedure of unfolding should be performed by considering proper values of the diffraction order parameter m of Equation 6.2. Figures 6.26 shows the resulting dispersion relation obtained after performing this unfolding procedure.

The fact that the dispersion relations obtained by considering different diffraction periods are superimposed confirms the proper choice of the diffraction order parameters during the unfolding procedure. Also note, that the dispersion relation behaves similar to the ones obtained theoretically and numerically as shown on Figure 5.7 and Figure 6.9 respectively. We are able to detect thermal coherent emission in a broad frequency range from 867 cm^{-1} to 3725 cm^{-1}, whereas an interface between two semi-infinite materials only supports surface waves from 1072 cm^{-1} to 1156 cm^{-1}. This spectral broadening is the result of Zenneck and subwavelength TM guided surface waves excitation from 867 cm^{-1} to 1072 cm^{-1} and from 1979 cm^{-1} to 3725 cm^{-1} respectively in addition to Surface Phonon-Polaritons.

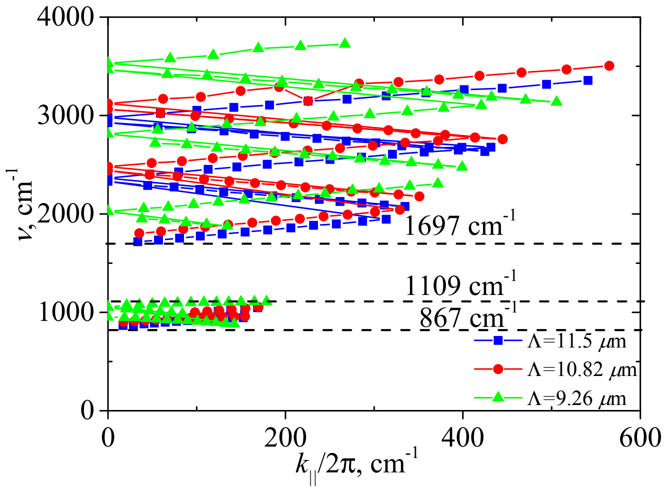

Figure 6.25: *Folded dispersion relations obtained by considering the experimental diffraction peak positions for various diffraction grating periods* Λ *and tilt angles* α *from diffraction gratings etched on 0.75* μm *thick* SiO_2 *film deposited on the aluminum layer.*

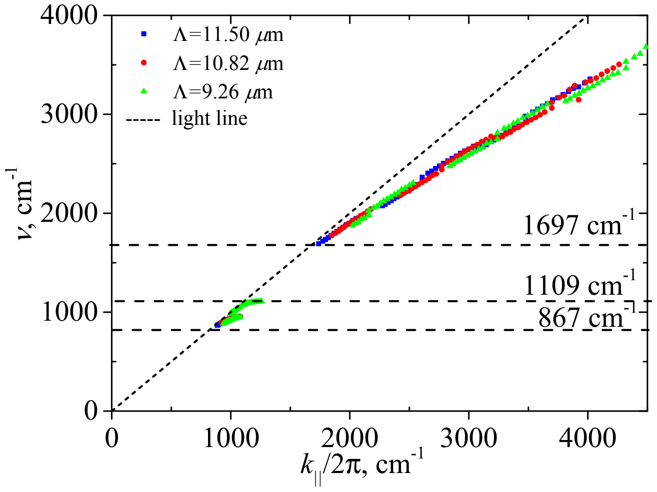

Figure 6.26: *Dispersion relation obtained by considering the experimental diffraction peak positions for various diffraction grating periods Λ and tilt angles α from diffraction gratings etched on the 0.75 μm thick SiO$_2$ film deposited on the aluminum layer.*

6.3.4 Coherence length of Surface Modes

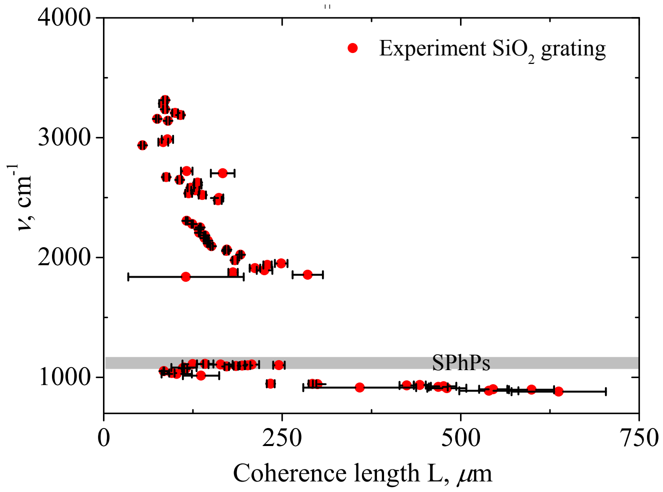

Figure 6.27: *Coherence length of the surface waves for the thin SiO$_2$ film deposited on aluminum layer obtained from the experimental measurements.*

Lifetime estimation of these surface modes can be obtained by analyzing the width of the grating emission peaks. Considering the experimental dispersion to be photon-like, the coherence length can be deduced as follows:

$$L = \frac{1}{2\Delta\nu}, \tag{6.3}$$

where $\Delta\nu$ is the full wave number width at half maximum of the emission peak in cm^{-1}. Figure 6.27 shows that the typical coherence length is in the order of 100 μm, that is ten times larger than the typical coherence length of these surface waves in a semi-infinite SiO_2-air interface. These values are in agreement with theoretical predictions for a 1 μm thick SiO_2 suspended film reported by Ordonez-Miranda *et al.* Ordonez-Miranda, Tranchant, Tokunaga, Kim, Palpant, Chalopin, Antoni, and Volz (2013). The obtained length range is also ten times larger than the typical coherence length of the surface waves of a semi-infinite SiO_2-air interface Ordonez-Miranda, Tranchant, Tokunaga, Kim, Palpant, Chalopin, Antoni, and Volz (2013) Joulain, Mulet, Marquier, Carminati, and Greffet (2005). The coherence length L reaches 700 μm for Zenneck modes which is almost two orders of magnitude larger than their wavelength. Such a large coherence length is achieved due to the fact that most of the electromagnetic energy is propagating in the air close to the interface of the dielectric rather than in the material, decreasing the absorbed power and enhancing the coherence length. Note that we underestimate the coherence length of the modes since the grating obviously introduces radiative losses and that the values are expected to be even larger for smooth thin films. The efficiency of grating diffraction depends on the ratio of etching depth to the attenuation length of the mode inside the layer and for more confined modes the diffraction is larger. In the case of TM guided modes, the electromagnetic field is well confined to the interfaces as has been demonstrated in the numerical simulations on Figure 6.4 and Figure 6.6. It results a very efficient diffraction of the mode by the grating, which significantly lowers experimentally measured propagation lengths. In the case of Zenneck modes the attenuation length of the electromagnetic field is large as shown on Figure 6.3 and Figure 6.5 compared to the grating etching depth. The propagation length of the mode is almost not influenced by the diffraction grating resulting in a large experimentally measured propagation.

6.4 Theoretical estimation of in-plane thermal conductivity of a thin glass membrane due to long-range surface modes

The results obtained in the chapter 5 together with the experimental results reported above should be considered when calculating the in-plane thermal conductivity of thin membranes due to the coupling of lattice phonons with photons at the interface of a thin film. It can be derived by considering a heat flux q_z along the film in z direction through its cross section $A_\perp$ as shown on the Figure 6.28.

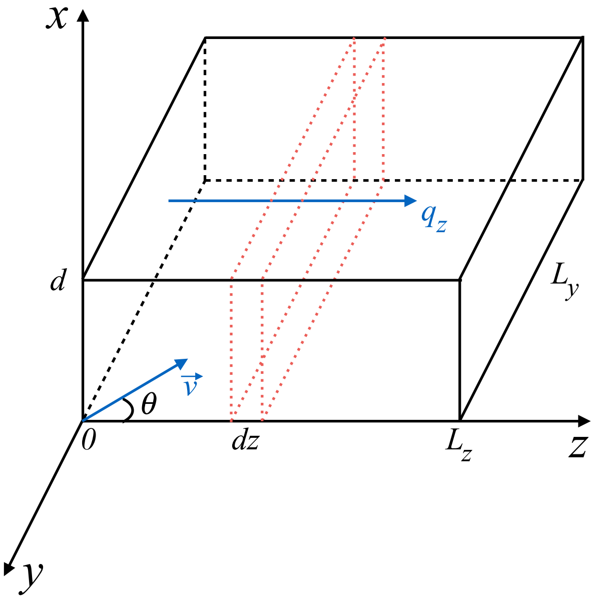

Figure 6.28: *Schematic illustration of an infinite membrane membrane of a thickness* d *used for calculation of a heat flux* q_z *along the film in* z *direction.*

By definition the heat flux is

$$dq_z = \frac{dE}{dtdA_\perp}, \tag{6.4}$$

where the energy can be defined according to the statistical mechanics as follows:

$$dE = e_m F_m \frac{d^2x d^2p}{h^2}. \tag{6.5}$$

The e_m is the energy of the mode, F_m is the electromagnetic mode distribution function, and h is a Planck constant. In the case of the plane geometry shown on Figure 6.28 one can obtain the following expressions:

$$d^2x = \frac{d^3x}{d} = \frac{dA_\perp dz}{d}, \tag{6.6}$$

$$dz = (\boldsymbol{v} \cdot \boldsymbol{z})\, dt, \tag{6.7}$$

$$p = \hbar k_{||}, \tag{6.8}$$

where $\boldsymbol{v}$ is the group velocity of the mode, $\hbar$ is a reduced Planck constant, and $k_{||}$ is the electromagnetic mode wavevector parallel to the film in z axis direction.

By using these later expressions, one can obtain the following expression for dq_z:

$$dq_z = \frac{e_m F_m}{4\pi^2 d} v \cos(\theta) d^2 k_{||}, \tag{6.9}$$

where for polar coordinates in $k_{||}$ space

$$d^2 k_{||} = k_{||} dk_{||} d\theta. \tag{6.10}$$

The heat flux can be obtained by integrating Equation 6.9 as follows:

$$q_z = \frac{1}{4\pi^2 d} \int v e_m F_m k_{||} dk_{||} \cos(\theta) d\theta. \tag{6.11}$$

Let us now consider the Bolzman Transport Equation (BTE) under steady state condition

$$\boldsymbol{v} \cdot \boldsymbol{\nabla} F = \frac{F_0 - F}{\tau}. \tag{6.12}$$

Assuming the propagation of the electromagnetic surface modes mainly in z direction

$$\boldsymbol{v} \cdot \boldsymbol{\nabla} F \backsimeq v_z \frac{\partial F}{\partial z}, \tag{6.13}$$

one can use the following expression of BTE for this system:

$$v_z \frac{\partial F}{\partial z} = \frac{F_0 - F}{\tau}. \tag{6.14}$$

In fact, if the propagation length $\Lambda = |\boldsymbol{v}|\tau$ of the mode is smaller than the size of the system L_z, the following assumption can be used:

$$\frac{\partial F}{\partial z} \backsimeq \frac{\partial F_0}{\partial z}. \tag{6.15}$$

By using this assumption, one can obtain the following expression for the distribution function F:

$$F = F_0 - \Lambda \cos(\theta) \frac{\partial F_0}{\partial z}. \tag{6.16}$$

Applying Equation 6.16, the heat flux given by Equation 6.11 can be written as follows:

$$\begin{aligned} q_z = \frac{1}{4\pi^2 d} \int v e_m k_{||} dk_{||} \Bigg[\int_{-\pi/2}^{\pi/2} \left(F_0 - \Lambda \cos(\theta) \frac{\partial F_0}{\partial z} \right) \cos(\theta) d\theta + \\ + \int_{\pi/2}^{3\pi/2} \left(F_0 - \Lambda \cos(\theta) \frac{\partial F_0}{\partial z} \right) \cos(\theta) d\theta \Bigg]. \end{aligned} \tag{6.17}$$

After the simplifications, one can write Equation 6.17 in the following form:

$$q_z = -\frac{\partial T}{\partial z}\frac{1}{4\pi d}\int v e_m \Lambda \frac{\partial F_0}{\partial T} k_{||} dk_{||} \equiv -\frac{\partial T}{\partial z}\kappa_m. \tag{6.18}$$

Thus, we have obtained a thermal conductivity of a thin film due to the surface electromagnetic modes presence as follows:

$$\kappa_m = \frac{1}{4\pi d}\int v e_m \Lambda \frac{\partial F_0}{\partial T} k_{||} dk_{||}, \tag{6.19}$$

where F_0 is the Bose-Einstein function and T is the temperature of the film. Equation 6.19 shows the dependence of the thermal conductivity due to the presence of electromagnetic surface modes in the film. However, in order to calculate the numerical value we need to use the dispersion relation of the modes in ether complex frequency or complex wavevector formalisms. For this reason, we will now consider both cases.
Let us consider the case of a complex frequency and real wavevector. In this case the group velocity of the mode is simply:

$$v = \frac{\partial \omega_r}{\partial k_{||}}, \tag{6.20}$$

where ω_r is the real part of the complex frequency. The coherence length:

$$\Lambda = \frac{v}{2\omega_i}, \tag{6.21}$$

where ω_i is the imaginary part of the complex frequency. The energy of the mode is:

$$e_m = \hbar\omega_r. \tag{6.22}$$

Applying Equations 6.20-6.22 to Equations 6.19 we obtain the expression for the thermal conductivity of thin film due to the presence of surface modes for a complex frequency formalism

$$\kappa_m = \frac{1}{4\pi d}\int \hbar \frac{\omega_r(k_{||})}{2\omega_i(k_{||})} v^2(k_{||}) \frac{\partial F_0}{\partial T} k_{||} dk_{||}. \tag{6.23}$$

In the case of real frequency and complex wavevector, the group velocity is defined as follows:

$$v = \frac{\partial \omega}{\partial k_{||r}}, \tag{6.24}$$

where $k_{||r}$ is the real part of the complex wavevector. The coherence length:

$$\Lambda = \frac{1}{2k_{||i}}, \tag{6.25}$$

where $k_{||i}$ is the imaginary part of the complex wavevector. The energy of the mode is:

$$e_m = \hbar\omega. \tag{6.26}$$

Equations 6.19 in the case of real frequency and complex wavevector should be written as follows:

$$\kappa_m = \frac{1}{4\pi d}\int \hbar\omega\Lambda(\omega)k_{||r}(\omega)\frac{\partial F_0}{\partial T}d\omega. \tag{6.27}$$

It has been shown Udagedara, Rukhlenko, and Premaratne (2011) that both formalisms provide the same results for the case of low absorption material (case of Zenneck region) and one can use ether complex frequency and real wavevector or real frequency and complex wavevector. We are using second formalism as in this case the integration over the real frequency is performed and the integration region can be defined and compared with the previous results in the literature Ordonez-Miranda, Tranchant, Tokunaga, Kim, Palpant, Chalopin, Antoni, and Volz (2013).

In order to calculate the in-plane thermal conductivity due to the presence of surface modes provided by Equation 6.27 one should consider the integration over the frequency region where electromagnetic modes can be thermally excited and optical phonons are present in the material. The density of states of phonons in pure amorphous SiO_2 has been reported in the literature and was obtained both theoretically, numerically and experimentally and compared by R.B. Laughilin and J.D. Joannopoulos Laughlin and Joannopoulos (1977) and later by A. Lehmann *et al.* Lehmann, Schumann, and Hubner (1983) and J. Sarnthein *et al.* Sarnthein, Pasquarello, and Car (1997) and is shown on Figure 6.29. The top frequency limit ω_t in the integral 5.1 should be considered as the maximum frequency for non-zero density of states of optical phonons in SiO_2. As shown on Figure 6.29(a, b, c), it is about $v = 1200$ cm^{-1} for all the methods. The bottom frequency limit ω_t should be set as the lowest frequency where the optical phonons are existing and surface electromagnetic waves are bounded to the interface of a thin film.

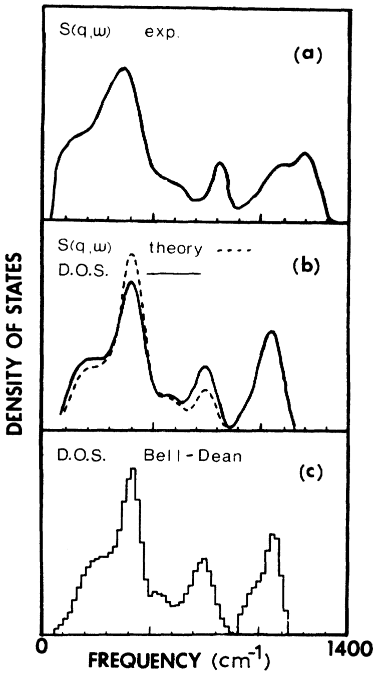

Figure 6.29: *Density of states of phonons in amorphous* SiO_2 *reported by R.B. Laughilin and J.D. Joannopoulos obtained by neutron measurements (a), by calculating average density of states (solid line) and by comparing with experimental data (dashed line) (b), by theoretical modelling with random-network model (c). The results are demonstrated in the work of R.B. Laughilin and J.D. Joannopoulos Laughlin and Joannopoulos (1977).*

One should take into account these new frequency limitations discussed above to calculate the in-plane thermal conductivity due to long-range surface modes. In order to understand the influence of Zenneck and SPhP modes, we analyzed the integrand function of Equation 5.1 for the in-plane thermal conductivity of the amorphous SiO_2 suspended membrane of 1 μm thickness shown on Figure 6.30. Thermal conductivity due to the surface waves can be obtained by calculating the surface under the curve in a proper frequency region. Grey and yellow colors indicate Zenneck and SPhP regions for all the temperatures. The contribution of Zenneck modes to the in-plane thermal conductivity is significantly larger than the one of SPhPs. Taking the lower limit of the integral being equal to the lowest experimentally detected frequency value of the diffraction resonance in the thermal emission (ω_l = 867 cm^{-1} = 163.4 TRad/s) and taking the upper limit as the highest frequency where SPhPs can be excited (ω_h = 1156 cm^{-1} = 217.9 TRad/s), one can obtain the in-plane thermal conductivity due to Zenneck and SPhP modes as shown on Figure 6.31. Note that such large values of thermal conductivity have never been predicted before as the contribution of Zenneck modes has never been taken into account.

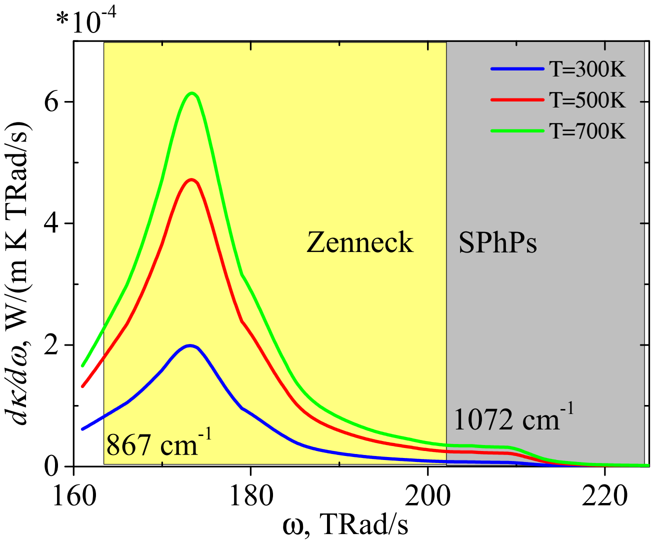

Figure 6.30: *Spectral in-plane thermal conductivity of 1 μm thick amorphous SiO_2 suspended membrane due to the long-range surface waves for different temperatures. Thermal conductivity can be calculated by considering the surface under the curve in the proper frequency range.*

We did the calculations for different thicknesses of the film and different temperatures similarly to the plot reported by J. Ordonez Ordonez-Miranda, Tranchant, Tokunaga, Kim, Palpant, Chalopin, Antoni, and Volz (2013) in order to demonstrate the importance of the Zenneck modes contribution to the total thermal conductivity due to surface waves. One can notice that for a 50 nm thick suspended SiO_2 membrane, thermal conductivity reaches 23 W/m.K while the bulk one is usually lower than 2 W/m.K. The effect is significantly higher for higher temperatures and for 700 K, the in-plane thermal conductivity reaches almost 80 W/m.K. It is more than 20 times higher than the one calculated by J. Ordonez when considering only the impact of SPhP modes. Note that these results are obtained for ideally smooth infinite suspended membranes and experimental detection of thermal conductivity increase due to surface waves remains complicated. Similar results could be obtained for any polar dielectric materials such as SiN, BN and others, and for some of these materials there are existing fabrication processes to obtain thin suspended membranes. Thus, the experimental detection of in-plane thermal conductivity increase due to long-range surface modes can be performed. We believe that this enormously large values of in-plane thermal conductivity due to Zenneck modes should lead to significant improvement in the thermal management design of nanoscale devices.

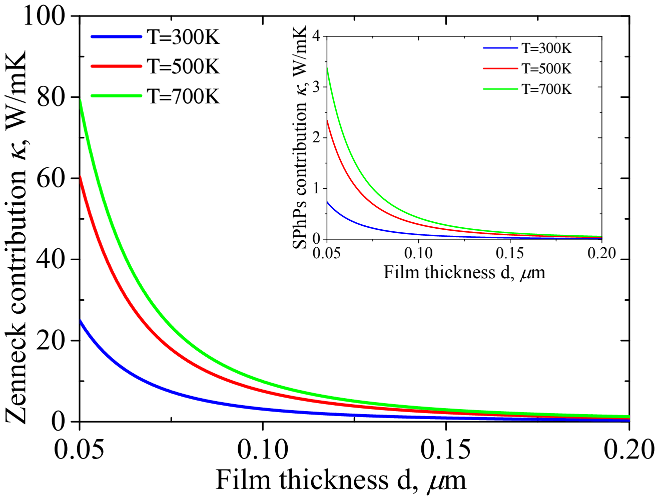

Figure 6.31: *Theoretical calculation of the in-plane thermal conductivity of an amorphous glass membrane as a function of its thickness calculated for different temperatures by considering both Zenneck and SPhP modes. The inset plot displays the same results obtained by considering only SPhPs modes Ordonez-Miranda, Tranchant, Tokunaga, Kim, Palpant, Chalopin, Antoni, and Volz (2013).*

6.5 Conclusions

In this chapter, we have demonstrated both numerically and experimentally that thin suspended polar dielectric membranes support long-range thermally excited surface waves for a significantly broader frequency range than is usually assumed. In fact, we have demonstrated that 1 μm thick SiO_2 suspended membrane supports thermally excited surface modes from 867 cm^{-1} to 3725 cm^{-1}, whereas an interface between two semi-infinite materials only supports surface waves from 1072 cm^{-1} to 1156 cm^{-1}. This important feature can be used to provide coherent thermal radiation in this frequency range as they have a very long coherence length (reaching almost 700 μm for Zenneck modes). The contribution of these modes to the in-plane thermal conductivity of thin suspended membranes has been demonstrated to be significantly higher than the phononic one. It reaches almost 80 W/mK for a 50 nm thick amorphous SiO_2 suspended membrane while the bulk thermal conductivity of SiO_2 is only 2 W/mK. Such a high thermal conductivity originate from the presence of Zenneck modes presence and the effect can be only observed for thin membranes where the surface effects predominate over volumetric ones.

Part IV

CALITREC project

Chapter 7

Infrared Characterization of Tunable Quantum Cascade Laser Optical Filters

In this chapter, we experimentally demonstrate the infrared spectroscopy mapping of Cavity Resonant Integrated Grating Filters (CRIGFs) designed as a part of the ANR research project CALITREC. We operated an infrared microscope coupled with a Fourier Transform Infrared spectrometer and performed the measurements of optical filters in order to optimize the parameters of the laser.

7.1 Description of the project

In this section, we will describe briefly the purpose of the ANR project and our contribution to it. This section is based on the information provided in the ANR proposal "Cascade Laser In Tunable Robust Extended Cavity" created by Olivier Gauthier-Lafaye *et al.*

7.1.1 Introduction

The CALITREC project focuses on the development of new external cavity tunable laser sources in the mid-infrared (3 - 12 μm)*, using Quantum Cascade Lasers (QCLs) with medium gain and using novel wavelength selective mirrors inspired from Guided Mode Reflective Filters (GMRF), the so-called Cavity Resonant Integrated Grating Filters (CRIGFs).*
The principle of quantum cascade was initially proposed in 1971 Kazarinov (1971), and implemented in 1994 Faist, Capasso, Sivco, Sirtori, Hutchinson, Cho, et al. (1994). *QCL is a unipolar device and the laser operation is obtained by inter-sub-bands transitions of a structure with coupled quantum wells, composed of a multitude of stacked heterostructures. This quantum confinement is due to large conduction band offsets. Currently these lasers show room*

temperature operation from 3 *to* 20 μm. *The use of a Distributed Feedback (DFB) or External Cavity Quantum Cascade Laser (EC-QCL) allows obtaining single frequency sources suitable for spectroscopy. In both architectures, the wavelength can be tuned, either by variation of the temperature in DFB (a few* cm^{-1}*), or by the rotation of a diffraction grating in the EC-QCL (hundreds of* cm^{-1}*). The advantage of the DFB configuration is that it makes a very stable source, insensitive to vibrations and with a spectral line width which can easily be stabilized to below 1 MHz. The tuning range of such sources is limited to a few* cm^{-1}*, either by direct change of the temperature of the component with a Peltier module, or indirect change of the temperature by changing the current into the device. It proves to be sufficient in the case of a mono-simple-gas spectroscopy but does not allow discrimination between different molecules within the same system or complex molecules, as it is the case for most molecules of interest in security and defense. Broader tunable ranges can be obtained via the use of an EC-QCL. The wavelength is not inscribed into the laser section, but it is usually provided by the reinjection of light by a diffraction grating. In this configuration, the diffraction grating behaves like a prism and for a given angle, only one wavelength is directed back into the laser. With this principle it has been shown a tuning range of* 200 cm^{-1} *at room temperature in continuous wave operation. These very interesting results at scientific level, did not allow the commercially available external cavities to enter systems for spectroscopy. In particular, for broadly tunable lasers, the wavelength accuracy and repeatability is limited to a few* cm^{-1}*, and their linewidth is limited by thermal and mechanical vibrations of the external cavity* Cendejas, Phillips, Myers, and Taubman (2010)*. Indeed, the mechanical stability (short term and long term), is insufficient. It can be attributed to the challenging alignment of the cavities used in such configurations.*

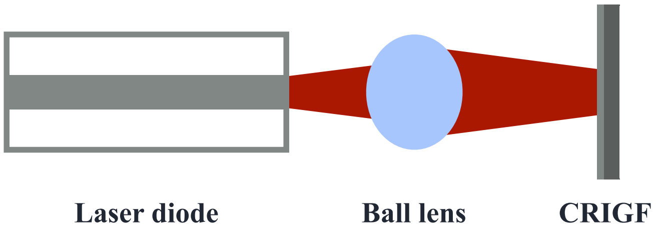

Figure 7.1: *Schematic illustration of a CRIGF filter typically used for laser diode output.*

The purpose of this project is to explore a new route to achieve highly robust, tunable external cavities for QCLs, using innovative wavelength selective mirrors that enable the use of extremely simple, cat's eye like, external cavities for laser diodes as shown on Figure 7.1. *Such tunable source would then easily find applications both for defense applications (gas sensing, environment monitoring) and for civil applications (environmental monitoring, process monitor-*

ing...), in fact for all applications where a compact, stable laser source with extended tunability could allow remote spectroscopy with high discrimination capabilities Rao and Karpf (2011).

7.1.2 Project stages

The CALITREC project consists of four main stages: theoretical and numerical modeling, fabrication, infrared CRIGF spectroscopy characterization, and building a prototype and tests.

The first part has been done at Institute Fresnel. They have developed theoretical and numerical models based on Rigorous Coupled-Wave Analysis (RCWA) and Finite-Difference Time-Domain models to design a non-tunable and tunable CRIGF and numerically optimize the parameters of CRIGF. Continuous tuning of the external cavity is achieved on a large range by tuning continuously the resonant wavelength of the CRIGFs. For 1D-CRIGF designs, continuous tuning is achieved by introducing a parametric gradient on some design parameters along the normally invariant direction. The external cavity tuning is achieved by mechanical translation of the filter which is one of the mirrors of the optical laser cavity. The models are used to choose the best design parameter, allowing the maximum continuous tuning range within fabrication constraints and best preserving both the reflectivity and bandwidth of the CRIGF. Optimized modeling codes developed at Institute Fresnel are used to quantify the achievable index variation, and the compatibility of complex layers with the realization of an anti-reflection coating.

The second part of the project, the fabrication of the CRIGF samples for their infrared spectroscopy characterization, was done by LAAS laboratory. Five different sets of CRIGF batches were fabricated on GaAs/AlGaAs materials at LAAS according to the results obtained at the first stage of the project. We have characterized each set of samples and provided a feedback that was used to improve each new generation of the samples by changing the fabrication techniques and adjusting the parameters.

The third part of the project, infrared spectroscopy micro-characterization of the CRIGF samples was performed by our team. We have tested the reflectivity of each sample fabricated at the second stage of the project and optimized the experimental setup to increase the sensitivity. We were providing the results to the LAAS group in order to achieve a better performance of the CRIGF. We have also performed an infrared microscopy spectral mapping of the Diffraction Grating region of the CRIGF in order to experimentally observe the lateral size of the mode.

The last part of the project is still in progress. LAAS group will build an external cavity adapted for MIR emission. The external cavity performance will be compared to expected performances from the chip. *Laser system characterization will be performed using high resolution spectroscopy to fully characterize the system performances. Single mode emission will be characterized* *by Fabry-Perot analysis of the emission line. At the end of this task LAAS group should establish frequency locking of an anti-reflection coated QCL laser using a CRIGF mirror. The cavity losses and optical feedback efficiency will be estimated through threshold comparison of the external cavity system with typical performances of the QCL structures investigated. The achievable tuning range will be established using separate CRIGF filters with varying periods. Single mode emission from the system will be assessed through high resolution spectroscopy of the emission at different driving currents. In these experiments, emission tuning by current variation in the QCL cavity will be measured. Using different coupling coefficients, the maximal bandwidth of the CRIGF required to achieve single mode emission will be determined.*

7.2 Sample design

Typical CRIGF filter consists of two Bragg mirrors forming a cavity with a diffraction grating in the center as shown on on Figure 7.2. The period of the Bragg gratings is chosen to form a cavity for a particular wavelength. The period of the diffraction grating in the center of the cavity is half the period of the Bragg grating. This is done in order to diffract efficiently the cavity mode in the direction normal to the interface. The length and the filling factors of each gratings as well as the offset region length were optimized by means of RCWA simulations to provide the performance of the CRIGF (narrow spectral width and high reflection efficiency). However, the values of the dielectric functions of the materials as well as the experimental geometrical parameters should slightly differ from the ones used in the numerical model and experimental reflectivity characterization should be performed in order to define the optimum values of the CRIGF parameters.

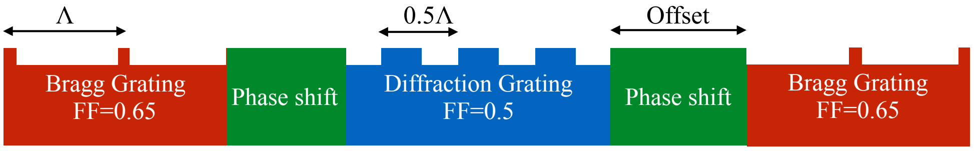

Figure 7.2: *Schematic illustration of CRIGF filter consisting of two Bragg mirrors forming a cavity with a diffraction grating in the middle separated by offset regions.*

The final version of CRIGF filters was fabricated in GaAs 2.15 μm thick layer deposited on AlAs 5.7 μm thick layer itself deposited on GaAs substrate as shown on figure 7.3. The grating has been etched using unisotropic Reactive Ion Etching (RIE) using nanoprint technological process. The lateral size of each CRIGF filter has been chosen to be 100 μm in width and 640 μm in length with about 50 μm width diffraction region at the center of the cavity. Typical period of the Bragg grating was around 1.4-1.5 μm.

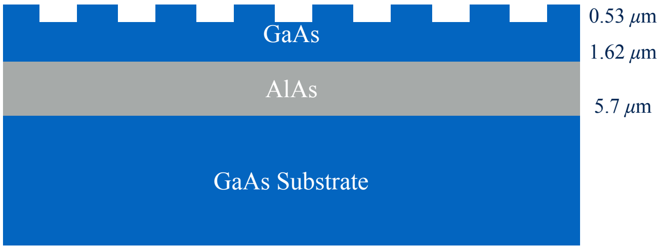

Figure 7.3: *Cross section schematic illustration of the last version of CRIGF filter.*

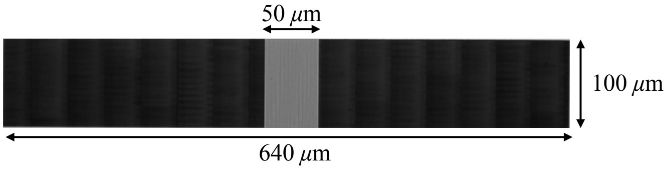

Figure 7.4: *SEM image of a single CRIGF filter demonstrating the lateral size of one unit. The middle grey region demonstrates the Diffraction grating.*

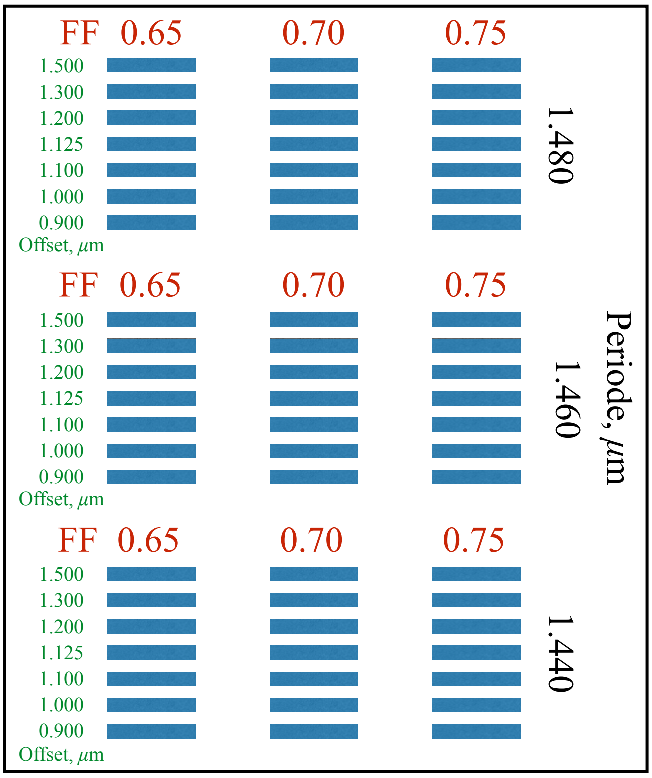

Figure 7.5: *Illustration of a test set of CRIGF filters designed for optimization of cavity parameters.*

Figure 7.3 shows a schematic illustration of a set consisting of 63 of CRIGF filters with different parameters. There were three parameters of the CRIGF filters the influence of which was examined experimentally: Filing Factor (FF) of the Bragg gratings, their period, and offset values. The FF of the diffraction grating was fixed to be 0.5, according to numerical simulation results.
A typical SEM image of the surface diffraction grating in the center of the cavity of the final sample generation is shown on figure 7.6.

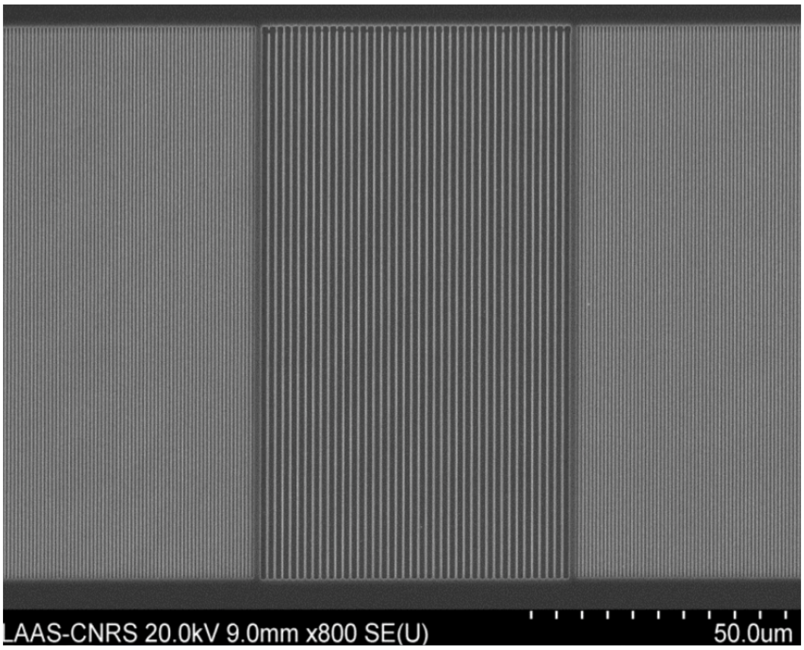

Figure 7.6: *Diffraction grating SEM image in the center of CRIGF filter with 1.460 μm period, FF=0.65, and 1.125 μm offset values. The results are obtained by LAAS group.*

In fact, our task was to measure the spectral reflectivity of the diffraction grating and to perform a spectral mapping of this region, which lateral size is only ten times larger than the wavelength. We needed to do such measurements for different CRIGF filter (in total 63 samples in each set) in order to define the optimum parameters of the CRIGFs.
Figure 7.7 shows a zoomed SEM image of a border of Bragg grating (larger period) with diffraction grating (smaller period and larger FF) with offset region in between two regions. It demonstrates high fabrication quality of the samples. The cross section SEM image is shown on 7.8, where the thicknesses of each layer are experimentally verified.

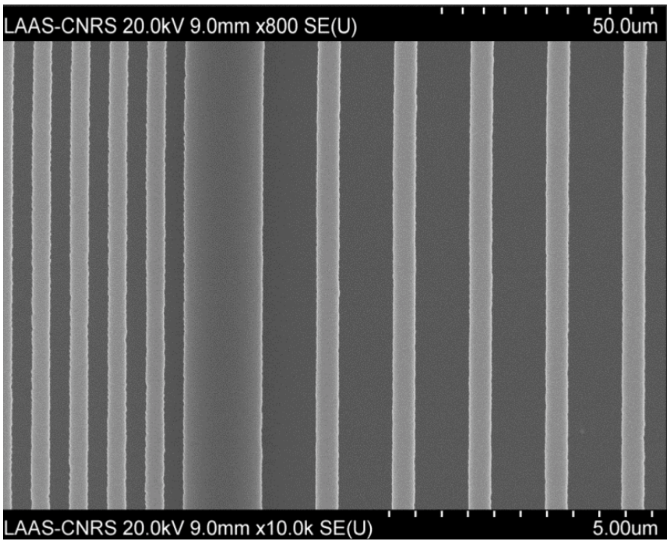

Figure 7.7: *SEM image of a CRIGF filter with 1.460 μm period, FF=0.65, and 1.125 μm offset zoomed on the border of Bragg grating (right side) with diffraction grating (left side) with offset region (wide strip in the middle). The results are obtained by LAAS group.*

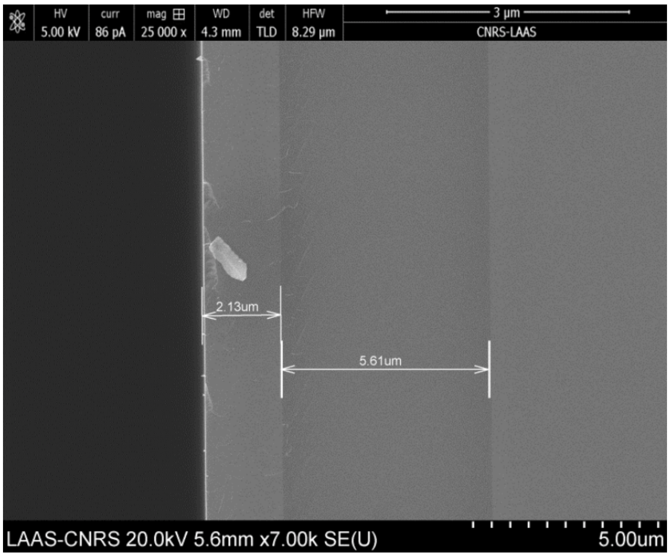

Figure 7.8: *Cross section SEM image of a CRIGF filter. GaAs wafer is located on the right side of the image. The results are obtained by LAAS group.*

Figure 7.9 shows a typical set of 63 filters which we used in our experimental analysis. The size of each wafer was about 2 cm.

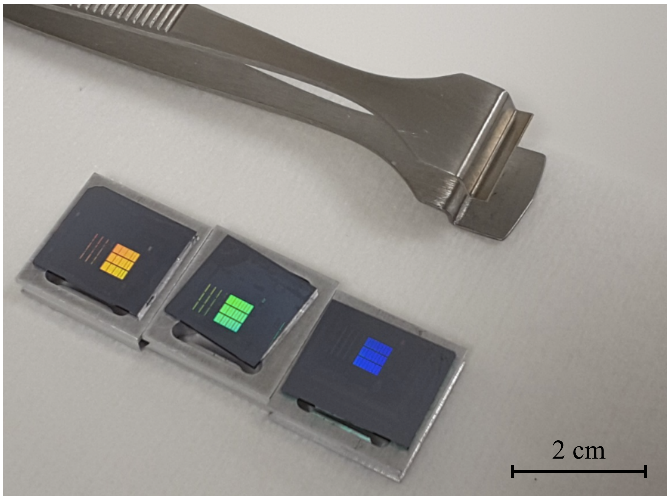

Figure 7.9: *Photo of a CRIGF filter sets fabricated on GaAs wafers for infrared spectroscopy characterization. The bright colour part of the sample contains 63 CRIGF filters with different parameters. The samples are fabricated by LAAS group.*

7.3 Experimental setup

In order to characterize the infrared spectral reflectively in micro-structured samples we used a standard FTIR spectrometer Nicolet 6700 coupled with a Continuum infrared microscope operated in reflectivity regime. The photo of the setup is shown on Figure 7.10.

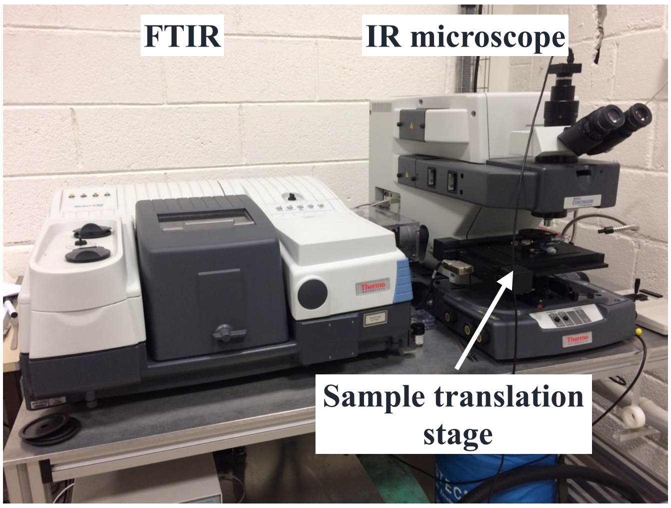

Figure 7.10: *FTIR spectrometer coupled with an infrared microscope.*

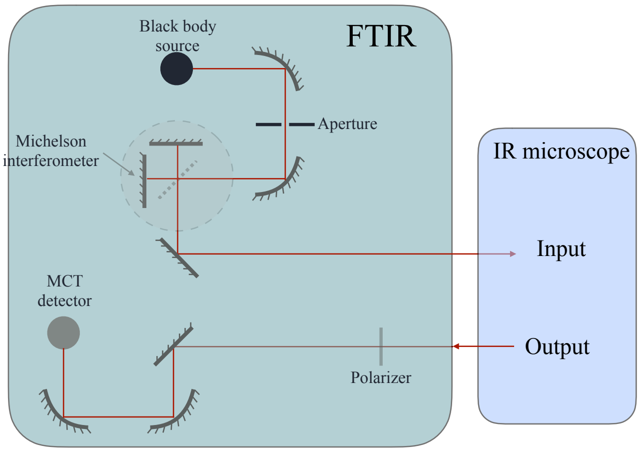

Figure 7.11: *Schematic illustration of the FTIR spectrometer coupled with the infrared microscope, operated in reflectivity regime.*

Figure 7.11 shows the internal structure of the spectrometer when operating together with the infrared microscope. We used a Globar heat radiation source in Turbo regime and modulated its infrared emission with a Michelson interferometer. The modulated beam was then sent to the infrared microscope. The reflected signal from the microscope was then detected with a MCT-A detector operating at liquid nitrogen temperature and standard analysis was performed in order to obtain infrared spectra discussed in details in the literature Griffiths, Haseth, and Winefordner (2007). We also used a KRS-5 holographic wire grid infrared polarizer which provides excellent transmission in the working frequency range (from 700 cm^{-1} to 4000 cm^{-1}). The polarizer orientation can be changed in order to examine thermal emission in both TM and TE polarizations. However, the polarizer decreases the sensitivity of the measurements for low intensity signals and it can be removed when needed.

The measurements were normally performed with a spectral resolution of 1 cm^{-1} for most of the experiments with the average number of scans being between 256 and 128 with and without the polarizer respectively. The average acquisition time of one measurement for these spectrometer parameters is usually about five minutes. However in order to obtain one reflectivity spectra there should be two experiments performed: the one of the reflected signal from the sample and another one measurement of the reflected signal from the gold mirror. The later signal is used for normalization purposes in order to obtain the spectral reflectivity of the sample.

Figure 7.12 shows the schematic structure of the infrared microscope used for the measurements in reflectivity regime. Globar emission signal modulated by FTIR spectrometer is used as an input. This signal is directed to the infrared objective through several mirrors and the signal reflected from the sample is then collected and separated from the rest of the beam by a separation mirror. The diaphragm is used to control the width of the output and input beam and as a result the illumination spot of the sample. The sample was placed on a motorized translation stage that allows for a precise positioning in both horizontal and vertical directions with less than 0.1 μm instrumental error. Our microscope was originally equipped with a Cassegrain reflector objective with 15× magnification, 0.4 numerical aperture, and 24 mm working distance shown on figure 7.13. Such an objective is a good choice for infrared microscopy spectroscopy as there are no dispersive elements and it provides excellent transmission without chromatic aberrations in a broad frequency range frequency range from 0.2 μm to 20 μm. However, due to its construction such an objective cannot collect signal for solid angles close to zero and cannot be used for measuring sharp reflectivity peaks of a CRIGF filter as they are expected to be observed for normal incidence angles only.

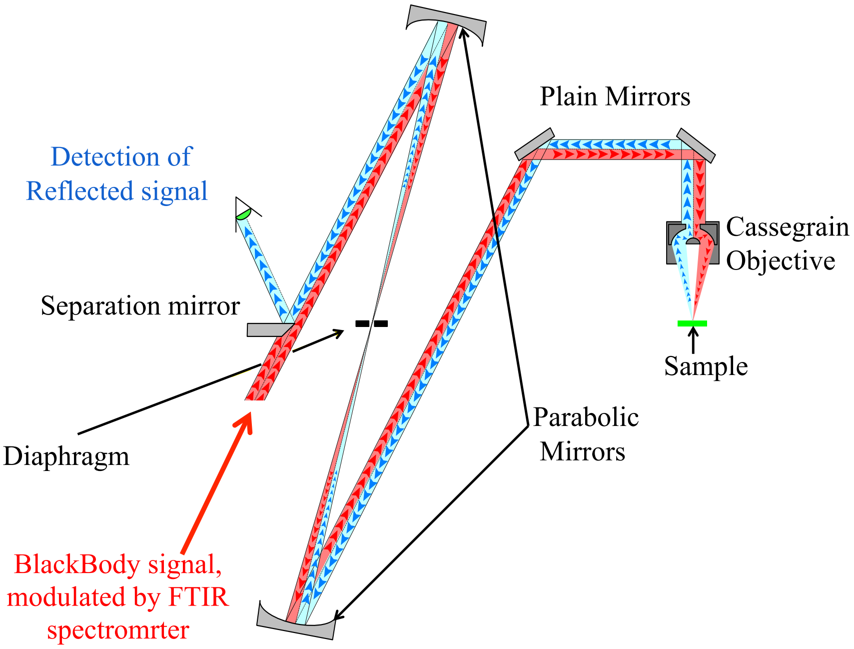

Figure 7.12: *Schematic illustration of the infrared microscope, operated in reflectivity regime.*

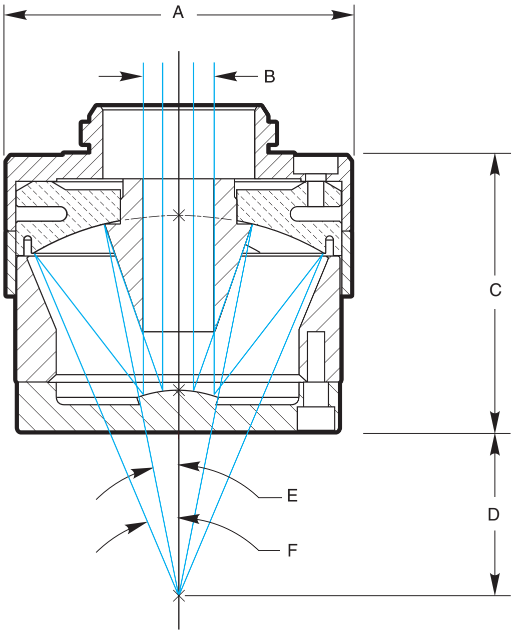

Figure 7.13: *Schematic illustration of a* 15× *Cassegrain reflector infrared microscope objective from Newport technical documentation.*

As we do not necessarily need a reflectivity spectrum in a broad frequency range but are only interested in a frequency region close the the CRIGF resonance from 4 μm (2500 cm^{-1}) to 5 μm (2000 cm^{-1}) we used ZnSe infrared objectives. We used a dielectric ZnSe lens as it provides a good transmission in the entire MIR region. However the transitivity drops rapidly in the visible part of the spectra which makes difficult the alignment of the sample and some additional illumination is needed. Spectral transmissivity of 5 mm thick ZnSe plate reported in ThorLabs technical documentation is shown on figure 7.14.

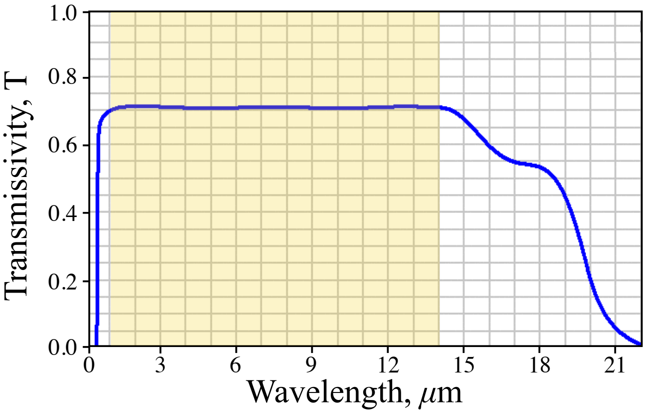

Figure 7.14: *Spectral transmissivity of a* 5 *mm thick ZnSe plate reported in ThorLabs technical documentation.*

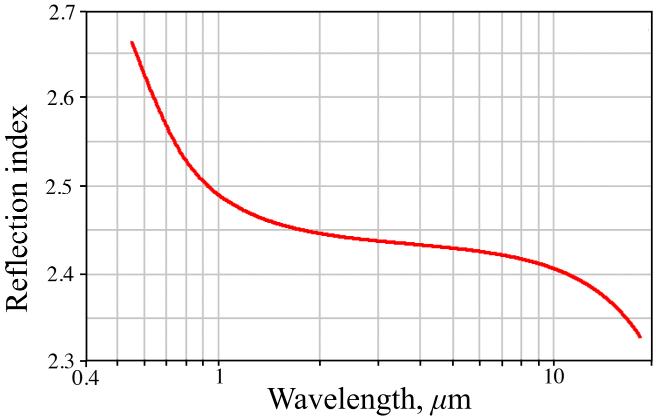

Figure 7.15: *Refraction index of ZnSe reported in ThorLabs technical documentation.*

Another important property of the objective is its dispersion which shows the variation of the refractive index with respect to wavelength. The refractive index dispersion of ZnSe is reported in the literature and we used the one provided in ThorLabs technical documentation shown on figure 7.15.

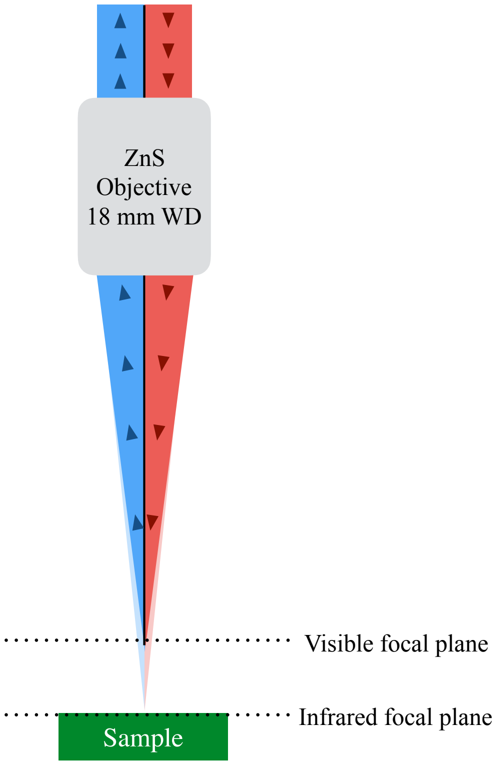

Figure 7.16: *Schematic demonstration of chromatic aberration caused by* 10% *difference of refraction index of ZnSe for visible and infrared wavelengths.*

ZnSe provides almost flat refractive index in the working frequency range from 4 μm (2500 cm^{-1}) to 5 μm (2000 cm^{-1}) with less than 0.5% variation within this interval. However, it is almost 10% larger for the visible part of the spectrum causing around 10% shorter focal length of the objective compared to the infrared part of the spectrum. This effect is demonstrated on figure 7.16. For each measurement, we need to align the sample in visible focal plane and then change the altitude of the sample by moving the translation stage in order to maximize the infrared reflected signal. In fact, by doing this, we can introduce a lateral displacement of the sample in infrared focal plane as schematically shown on figure 7.17.

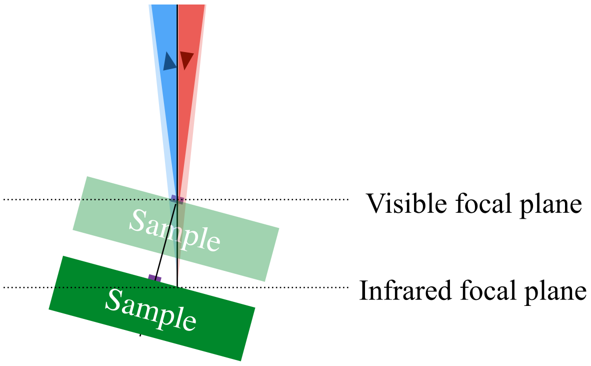

Figure 7.17: *Schematic demonstration of possible miss-alignment caused by a possible tilt angle of the sample with respect to the microscope objective.*

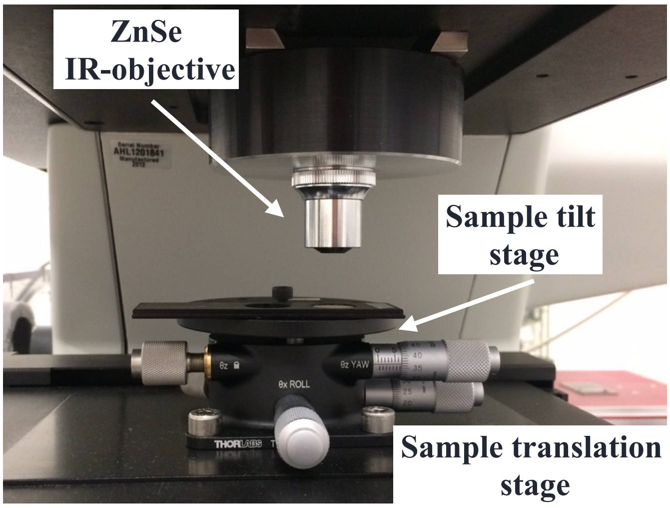

Figure 7.18: *ZnSe infrared objective used in the IR microscope. The sample is placed on a tilt stage, which is attached to the translation stage.*

Such kind of displacement can be significantly reduced by introducing a tilt stage shown on figure 7.18 allowing for a fine control of sample tilt. Together with translation stage, the tilt stage gives all six degrees of freedom to position a sample in space and to achieve proper alignment of a sample.

We had three different ZnSe microscope objectives available for our setup: with 6 mm Working Distance (WD), numerical aperture NA= 0.25, maximum collection angle $\alpha_{max} = 14.5°$; with WD= 12, NA= 0.13, $\alpha_{max} = 7.5°$; with WD= 18 mm, NA= 0.08, $\alpha_{max} = 4.5°$. In fact, we are interested in the smallest maximum collection angle of the objective in order to collect the reflectivity peak of the CRIGF filter. It is important to notice that smaller collection angles also causes smaller numerical apertures and as a result smaller intensity of the signal together with low magnification of the objective.

It is also important to mention that the orientation of the sample should be chosen in such a way that most of the light with largest incident angles should illuminate the samples along the grating as shown on figure 7.19

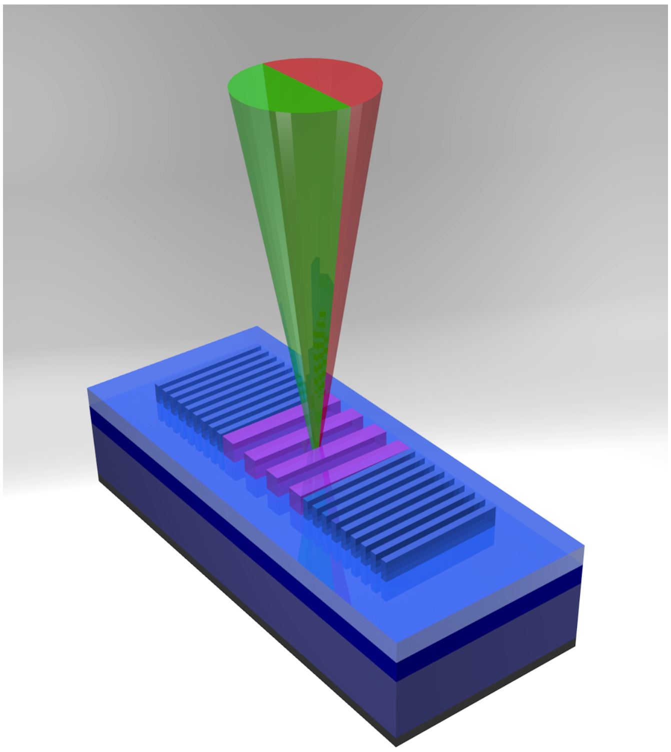

Figure 7.19: *Schematic demonstration of how incident light focused by the ZnSe objective is being reflected from the diffraction grating region of a CRIGF sample. The red and green colours correspond to the incident and reflected parts of the beam respectively.*

It is also important to notice that if the separation mirror is slightly misaligned according to the center of the beam, the incident and reflected parts of the beam would not be equal and the reflected signal with the smallest angles would not be detected. This would result in a low value of the reflectivity peak of the CRIGF filter as it is designed to provide maximum reflectivity in a very narrow angle range close to zero degree. In fact, this is what we observed at the beginning of the measurements and a lot of efforts were done in order to achieve a proper alignment of the separation mirror. However, the alignment cannot be done perfectly and we should still be missing a part of the reflected signal for incident angles close to zero degree and our measurements should provide an underestimation of the reflectivity peak.

7.4 Results

In this section, we compare the last two generations of the samples fabricated by the LAAS laboratory and skip all previous sets of samples that we have measured. The latest generation of the sample is marked as CVL4C9_14_1. The generation of the sample before CVL4C9_14_1 is marked as CVL5C9_6_1. These names are used to distinguish between different fabrication steps used and we keep them like they are to make this thesis clear for our partners.

7.4.1 Parametric study

Figure 7.20 demonstrates spectral reflectivity of CVL4C9_14_1 CRIGF filter with FF$= 0.65$ μm, offset$= 1.125$ μm, and period$= 1.440$ μm. We used the polarizer to examine the reflectivity signal in TE polarization. Figure 7.20 shows three spectra for three different ZnSe objectives with working distances 18 mm, 12 mm, and 6 mm. Note, that for the objective with WD$=$ 18 mm the numerical aperture and the maximum collection angle are the smallest. As a result the signal of this objective is the lowest and the signal/noise ration is the smallest among all three objectives. However, we can observe the strongest reflectivity resonance as the maximum collection angle of the objective is the smallest $\alpha_{max} = 4.5°$. It is also the sharpest peak due to the same reason. The objective with larger collection angles provide better signal/noise ratio, but the large collection angles reduce the reflectivity peak and increase its width. We have also checked the reflectivity signal with completely closed diaphragm in order to verify that there is no back-reflection of the beam inside the microscope and the baseline is not shifted due to this reason. The dashed region on the plot indicates the frequency region where CO_2 absorption is large and the sensitivity of the spectrometer decreases. This effect results in smaller signal/noise ratio in this frequency region from 2330 cm^{-1} to 2380 cm^{-1}.

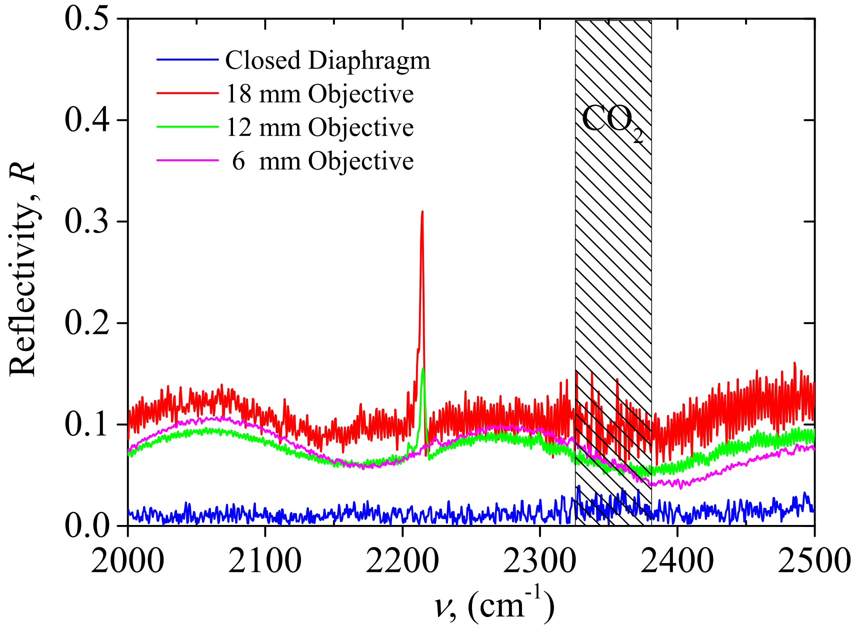

Figure 7.20: *Spectral reflectivity of CVL4C9_14_1 with FF=* 0.65 *μm, offset=* 1.125 *μm, and period=* 1.440 *μm. The data is obtained with three different ZnSe objectives (*18 *mm,* 12 *mm, and* 6 *mm working distance) for* 50 *μm diaphragm size (red, green, magenta curves) and with closed diaphragm (blue curve). All the reflectivity spectra are obtained in TE polarization with* 1 *cm^{-1} spectral resolution by averaging over 256 scans.*

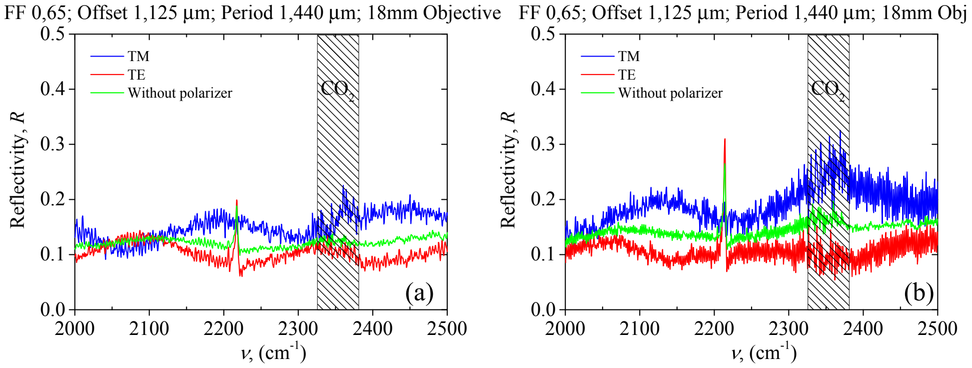

Figure 7.21: *Spectral reflectivity of CVL5C9_6_1 sample generation (a) and CVL4C9_14_1 sample generation (b) of a diffraction gratings of CRIGF filters with FF=* 0.65 *μm, offset=* 1.125 *μm, and period=* 1.440 *μm. The results are obtained with WD=* 18 *mm ZnSe objective for TM (blue curves) and TE (red curves) polarizations and without a polarizer (green curves).*

Figure 7.21(a) and Figure 7.21(b) show the spectral reflectivity of CVL5C9_6_1 and CVL4C9_14_1 generations of samples, respectively. The data was obtained with WD= 18 mm ZnSe objective for TE and TM polarizations and without a polarizer for CRIGFs with the same parameters (FF= 0.65 μm, offset= 1.125 μm, and period= 1.440 μm). There is no reflectivity peak for TM polarization as predicted by both theory and numerical simulations performed at Institute Fresnel by our partners due to the orientation of the diffraction grating. This important feature provides a possibility to separate the TM polarization and to consider only TE polarization. For TE polarization, the baseline is lower compared to the case when the polarizer is removed. This allows us to better separate the reflectivity peak from the noisy signal. From now on, we present all our results for TE polarization only. It should be also noticed that the latest generation of the samples provides more resonant reflectivity peak as the fabrication process of significantly improved compared to previous sample generation CVL5C9_6_1.

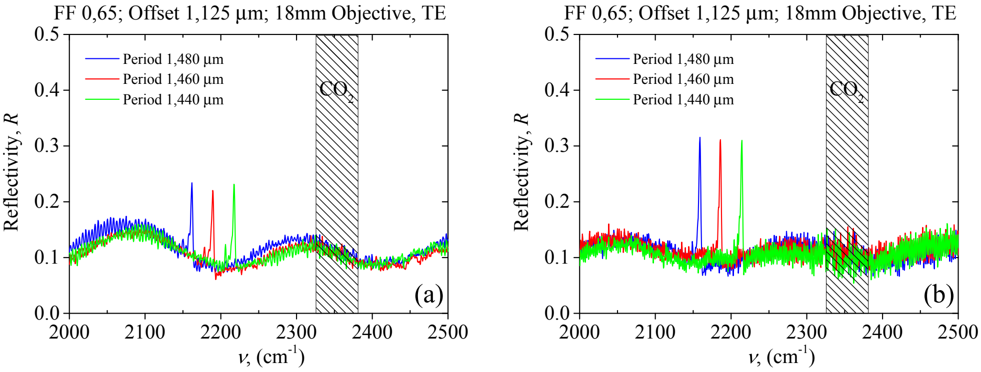

Figure 7.22: *Spectral reflectivity of CVL5C9_6_1 sample generation (a) and CVL4C9_14_1 sample generation (b) of a diffraction gratings for different CRIGF filters periods with same FF=* 0.65 μm *and offset=* 1.125 μm*. The results are obtained with WD=* 18 *mm ZnSe objective for TE polarization.*

Figure 7.22(a) and Figure 7.22(b) show the spectral reflectivity of CVL5C9_6_1 and CVL4C9_14_1 generations of samples, for different periods of the Bragg gratings of the CRIGF filters, respectively. We wanted to check if all the periods work in this frequency region. In fact, we have analyzed all the 63 different CRIGF filters with all possible variations of filing factors and offsets, but we are plotting only the best performing ones for the same values of filling factors and offset values in order to vary only one parameter of the filter at once. One can notice that both CVL5C9_6_1 and CVL4C9_14_1 generations of samples behave similarly but the latest generation (CVL4C9_14_1) provides significantly larger peak values of the reflectivity as well as smaller width of the peaks than CVL5C9_6_1 one for exactly the same parameters. For example, the reflectivity of CVL4C9_14_1 diffraction grating of the CRIGF filter with FF= 0.65 μm, offset= 1.125 μm, and period= 1.440 μm reaches almost $R = 0.32$ at $\nu = 2217$ cm^{-1} while the reflectivity of CVL5C9_6_1 generation is only $R = 0.24$ for exactly the same parameters. It should be also noted that the reflectivity peak shifts to the lower frequencies when the period of the CRIGF increases as predicted by the theory and numerical results.

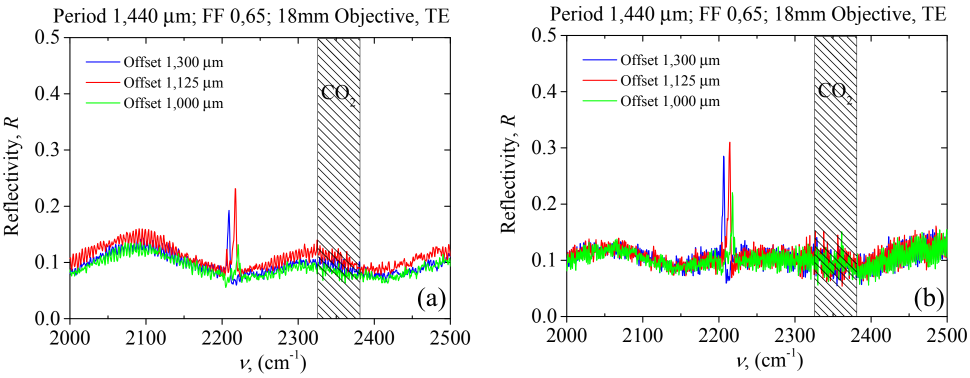

Figure 7.23: *Spectral reflectivity of CVL5C9_6_1 sample generation (a) and CVL4C9_14_1 sample generation (b) of diffraction gratings for different CRIGF filters offsets with same FF=* 0.65 *μm and period=* 1.440 *μm. The results are obtained with WD=* 18 *mm ZnSe objective for TE polarization.*

We now fix the period and filing factor and examine the influence of the offset on the reflectivity peaks of the CRIGF diffraction grating. Figure 7.23(a) and Figure 7.23(b) show the spectral reflectivity of CVL5C9_6_1 and CVL4C9_14_1 generations of samples for different offsets of CRIGF filters, respectively. We want to find the optimum value of the offset when the reflectivity peak is the most resonant. In fact, the reflectively peak was slightly shifted in frequency for non optimum values of offsets significantly decreasing its reflectivity. The optimum value of the offset was found to be close to 1.125 μm for all the periods and filling factors.

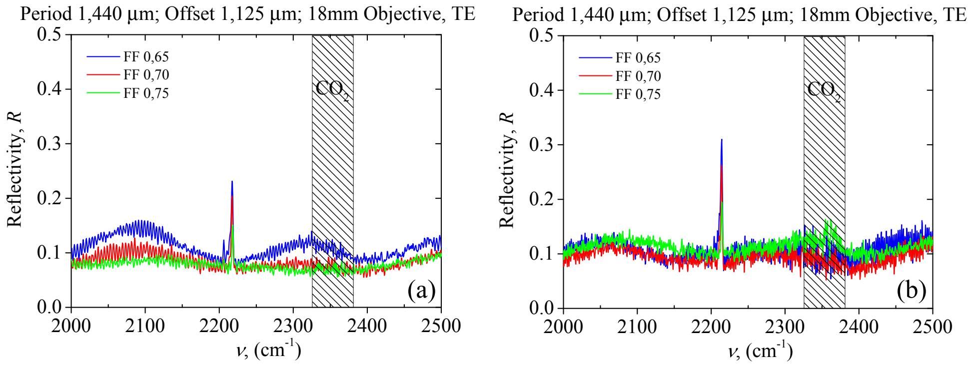

Figure 7.24: *Spectral reflectivity of CVL5C9_6_1 sample generation (a) and CVL4C9_14_1 sample generation (b) of diffraction gratings for different CRIGF filters filing factors with same offset=* 1.125 *μm and period=* 1.440 *μm. The results are obtained with WD=* 18 *mm ZnSe objective for TE polarization.*

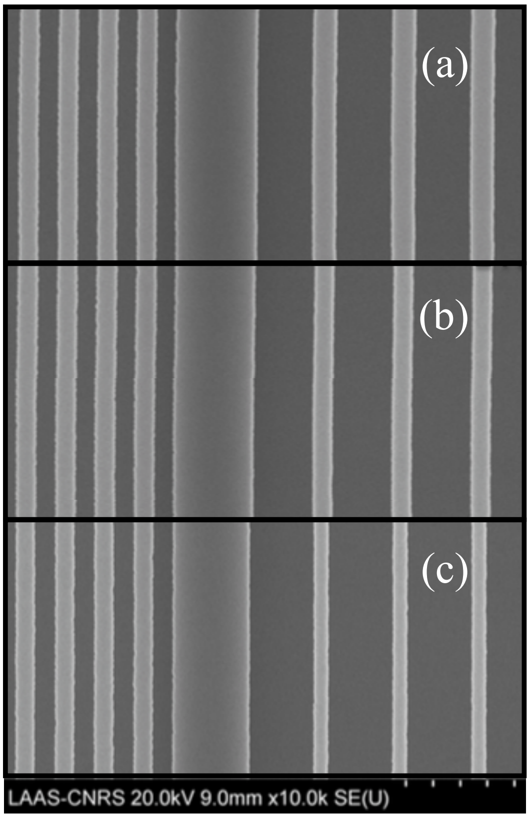

Figure 7.25: *SEM images of CVL4C9_14_1 CRIGF filters for different filling factors: (a) FF=* 0.65*, (b) FF=* 0.70*, and (c) FF=* 0.75*. The offset=* 1.125 *μm and period=* 1.440 *μm are the same for all samples. The results are obtained by LAAS partners.*

In order to defined the optimum filing factor of CRIGF filter, we compare the spectral reflectivity of CVL5C9_6_1 and CVL4C9_14_1 generations of samples shown on Figure 7.24(a) and Figure 7.24(b), respectively. For the smallest filling factor FF= 0.65, the reflectivity peaks are more resonant for both generations of the samples. In fact, we should consider a grating even with smaller filling factor in order to find the optimum parameter. Figures 7.25(a,b,c) show SEM images of CVL4C9_14_1 CRIGF filters for different filling factors of Bragg gratings and same offset= 1.125 μm and period= 1.440 μ. The real FFs are slightly different from the ones designed. By analyzing these SEM images, we found that for predesigned FF= 0.65, FF= 0.70, and FF= 0.75 the real filling factors are about 15% larger: FF= 0.76, FF= 0.82, and FF= 0.88, respectively. This is the reason why the predesigned FF= 0.65 appears to be the best performing one, while the numerical simulations and theory predict FF= 0.70.

We used a spectral resolution of 1 cm^{-1} for all our measurements as with higher resolution, we need to increase the acquisition time significantly. For example, for a resolution of 0.5 cm^{-1}, one measurement takes 4 times longer than for 1 cm^{-1} resolution with same signal/noise ratio. However, we wanted to examine if the resolution is good enough in order to spectrally resolve the reflectivity peak. Figure 7.26 shows spectral reflectivity of the CVL4C9_14_1 CRIGF filter with FF= 0.65, offset= 1.125 μm and period= 1.440 μm measured with usual 1 cm^{-1} resolution and 0.5 cm^{-1} resolution with same signal/noise ratio. Note that the two experimental results are almost superimposed and this proves that a 1 cm^{-1} spectral resolution is enough to resolve the reflectivity peaks.

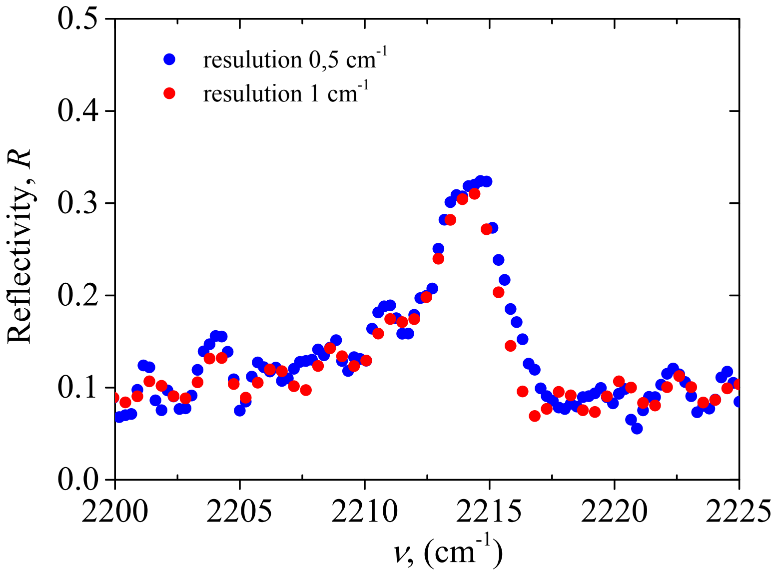

Figure 7.26: *Spectral reflectivity of CVL4C9_14_1 CRIGF filter with FF=* 0.65*, offset=* 1.125 *μm and period=* 1.440 *μm measured with usual* 1 *cm*$^{-1}$ *resolution and* 0.5 *cm*$^{-1}$ *resolution with 256 and 1024 scans, respectively.*

Our infrared microscope was equipped with electrically controlled diaphragm as was shown on Figure 7.12 which allows us to continuously adjust the illumination spot of the sample area where the reflectivity signal is collected. However, the instrumental uncertainty of the illumination area spot was around several microns. When the diaphragm size reduces the reflected signal decreases as well resulting in a low signal/noise ratio. Figure 7.27 illustrates the smallest illumination spot with respect to the SEM image of the CRIGF when the signal can be detected. For illumination spots less than 40 μm, the reflectivity signal cannot be detected. We typically used illumination spots slightly larger than the minimum one (from 50 μm to 90 μm) in order to guarantee acceptable signal/noise ratio.

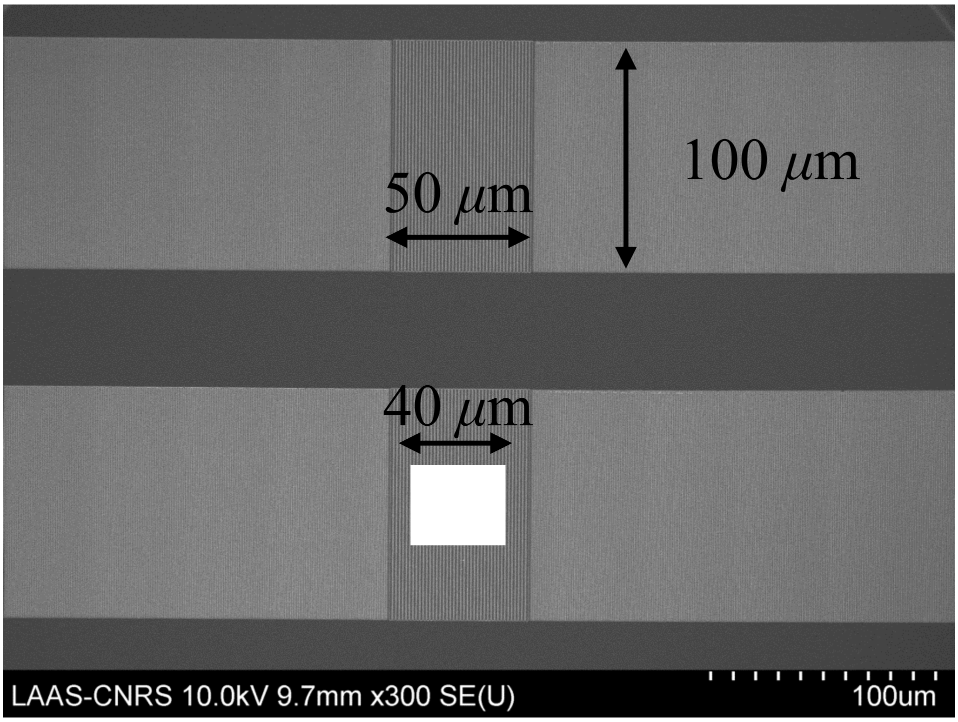

Figure 7.27: *Schematic illustration of a minimum illumination spot of the CRIGF diffraction grating with respect to the SEM image of the CRIGF when the reflectivity signal can be detected.*

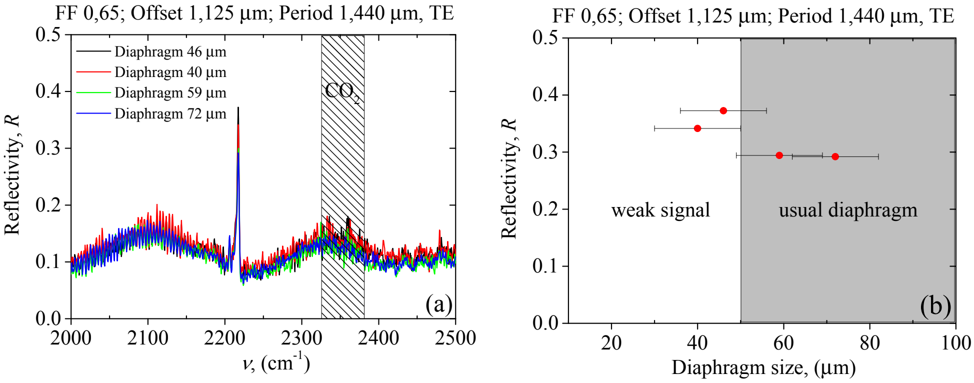

Figure 7.28: *(a) Spectral reflectivity of CVL4C9_14_1 CRIGF filter with FF=* 0.65*, offset=* 1.125 μm *and period=* 1.440 μm *obtained for different sizes of the diaphragm (illumination spots of the diffraction grating). (b) Maximum of the reflectivity peaks as a function of diaphragms size.*

In order to study the dependence of the maximum value of the reflectivity peak of illumination spot of the diffraction grating we performed measurements of same CVL4C9_14_1 CRIGF filter with FF= 0.65, offset= 1.125 μm and period= 1.440 μm for different diaphragm sizes. Figure 7.28(a) shows these spectra. Figure 7.28(b) demonstrates the maximum values of the reflectivity peaks. The peaks are observed to be stronger for smaller values of the diaphragms. Also note that the noise increases when diaphragm size decreases. For diaphragm size of 46 μm we detected reflectivity peak as large as $R = 0.38$.

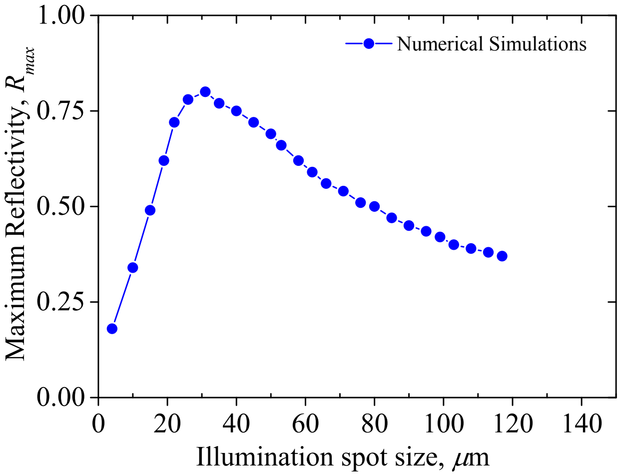

Figure 7.29: *RCWA numerical results for the maximum of the reflectivity peaks of CVL4C9_14_1 CRIGF filter with FF=* 0.65*, offset=* 1.125 μ*m and period=* 1.440 μ*m as a function of diaphragm sizes. These results are obtained by our partners at Institute Fresnel.*

Our partners from Institute Fresnel have performed RCWA simulations for the same CRIGF filter shown on figure 7.29 where they have analyzed the reflectivity of the diffraction grating for normal incidence as a function of illumination spot. They found the largest value of the reflectivity peak $R = 0.81$ for illumination spot close to 30 μm. The maximum of the reflectivity decreases rapidly for larger illumination spot area. The difference between the absolute values of the reflectivity peak for the same illumination spot can be explained by significantly larger collection angle range of the objective used in the experiments as well as some fabrication uncertainties of the samples.
Figures 7.30(a,b,c) demonstrate the continuous improvement of the reflectivity peaks with each new generation of the sample. All the samples are measured with exactly the same parameters. Figure 7.30(a) shows one of the first generation of the CRIGF filters where the maximum reflectivity of the diffraction gratings is smaller than $R = 0.18$, while the latest generation demonstrates the reflectivity as high as $R = 0.32$. We have also significantly improved the linewidth of the picks for the latest generation of the sample shown on figure 7.30(c).

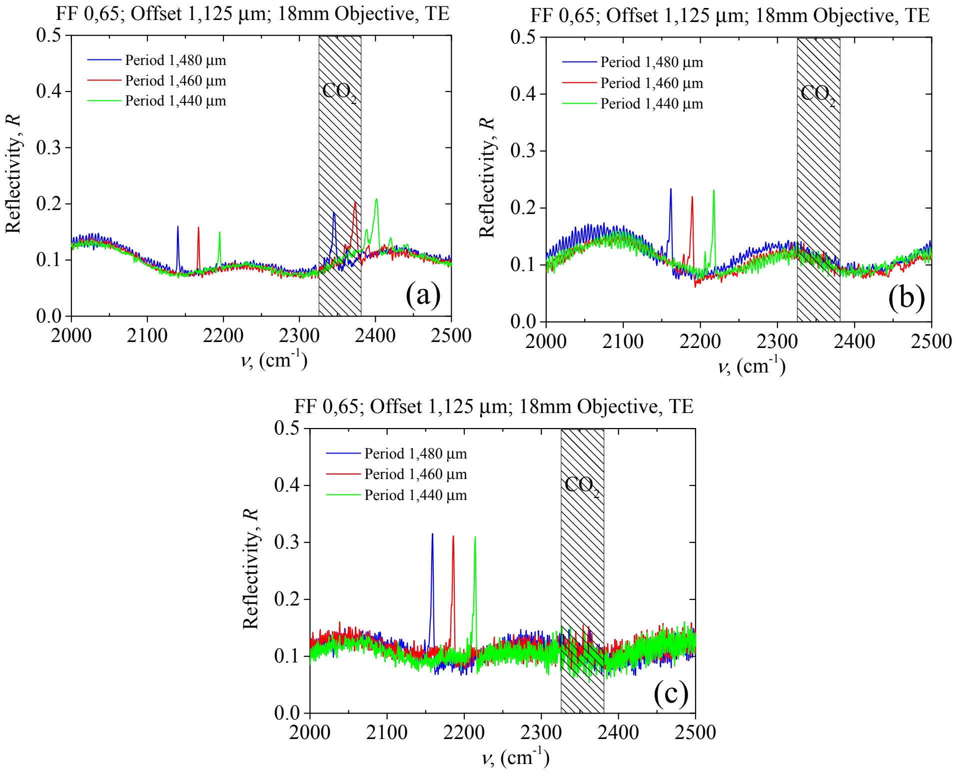

Figure 7.30: *Demonstration of the reflectivity pick improvement for the first (a) second (b) and third (c) generations of the samples. The results are obtained for exactly the same parameters of the CRIGF filters with FF=* 0.65*, offset=* 1.125 *μm and period=* 1.440 *μm under TE polarization.*

7.4.2 Infrared mapping of the diffraction region of CRIGF

In this section, we demonstrate the possibility of infrared spectroscopy mapping of diffraction gratings of CRIGF filters. Our setup allows to control position of the sample in the horizontal plane using the motorized translation stage. We used a step of 10 μm in both x and y directions to obtain spectral reflectivity around the middle of the diffraction grating of the CRIGF with the four optimum parameters of the filter (FF= 0.65, offset= 1.125 μm and period= 1.440 μ). Figure 7.31(a) shows the map of the reflectivity of CVL5C9_6_1 CRIGF filter for the resonant frequency $\nu_{\text{res}} = 2217$ cm^{-1}. The reflectivity is large on the center of the diffraction grating and drops down for the Bragg gratings. Figure 7.31(b) shows the map of the reflectivity of CVL5C9_6_1 CRIGF filter for a frequency $\nu = 2192$ cm^{-1}. This frequency is out of the sharp reflectivity peak of the diffraction grating and we cannot distinguish between diffraction grating and Bragg grating as they have nearly the same reflectivity. Note that the lateral position of the diffraction grating is exactly the same.

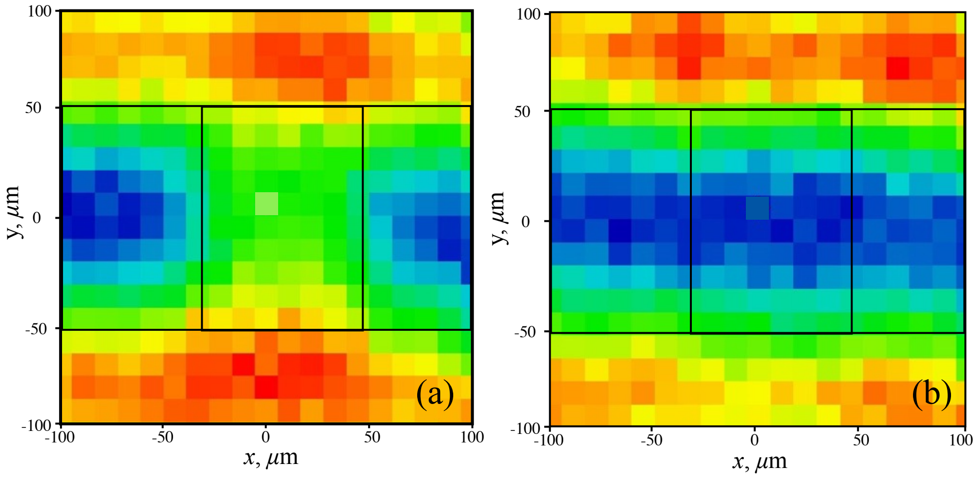

Figure 7.31: *CVL5C9_6_1 CRIGF diffraction grating map obtained for the resonance frequency* ν_{res} = 2217 cm^{-1} *(a) and for a frequency out of resonance* ν = 2192 cm^{-1} *(b). The measurement was performed for a CRIGF filter with FF=* 0.65*, offset=* 1.125 μm *and period=* 1.440 μm*. Black lines indicate the lateral position of the CRIGF filter with respect to its diffraction grating region.*

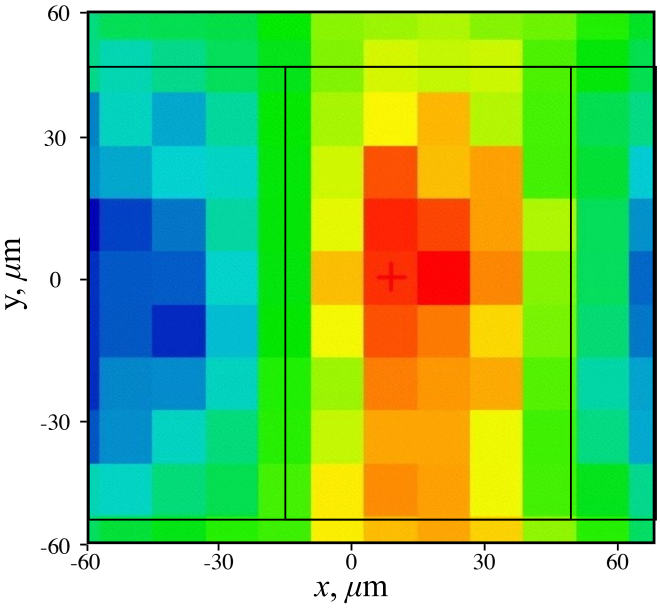

Figure 7.32: *CVL4C9_14_1 CRIGF diffraction grating map obtained for resonance frequency* ν_{res} = 2217 cm^{-1}*. The measurement was performed for CRIGF filter with FF=* 0.65*, offset=* 1.125 μm *and period=* 1.440 μm*. Black lines indicates the lateral position of the CRIGF filter with its diffraction grating region.*

Mapping in such a large area is a very slow process and it requires nearly 34 hours to obtain one infrared map. For this reason we usually use significantly smaller area of the map with less number of scans and smaller resolution. When the resolution is set to be 2 cm^{-1} and the number of scans is fixed to be 64 for one point of the map, the process does not take longer than 3 hours for one map. Figure 7.32 shows the map of the diffraction grating of CVL4C9_14_1 CRIGF filter with FF= 0.65, offset= 1.125 μm and period= 1.440 μm for a resonance frequency of $\nu_{\mathrm{res}} = 2217\ \mathrm{cm}^{-1}$. One can clearly observe that the infrared reflectivity for this frequency indicates the position of the diffraction grating.

7.5 Conclusions

In this chapter we have developed and demonstrated infrared spectroscopy microscopy measurements of the reflectivity of diffraction gratings used as a part of CRIGF filters in Quantum Cascade Lasers. Together with our partners we found that the best performance of the CRIGF filters can be achieved with Filling Factors of the Bragg gratings around 0.65 and offsets values around 1.125 μm for periods of the Bragg gratings from 1.440 μm to 1.480 μm. Such CRIGF filters can provide reflectivity as large as $R = 0.38$ for TE with linewidth of less than 3 cm^{-1} when the reflectivity out of resonance is not exceeding 10%. We have also developed a methodology to perform a spectral mapping of diffraction grating region of CRIGF filters which allows us to distinguish the shape of the mode inside the cavity. All the results discussed above demonstrates the underestimation of the reflectivity peaks and the overestimation of the linewidth of the CRIGF filters as we collect the reflectivity spectra within 9 degrees angles. These results demonstrate the possibility of realization of tunable QCL in an atmospheric window around 4.5 μm wavelength.

Conclusion

In this work, we have studied optical and thermal properties of Surface Phonon Polaritons, Zenneck modes, and guided modes for various geometrical micro and nano systems both theoretically and experimentally. We used optical and thermal systems based on ordinary amorphous glass in most of our work as this material is a very common dielectric used in the industry and its dielectric constant exhibits a resonance around 10 μm corresponding to the maximum of black body radiation at room temperature. In fact, most of our results are general and can be applied for any polar dielectrics supporting surface waves (e.g SiC, SiN, BN, VO).

We have shown that conical and wedge glass micro structures are efficient tools for concentration of Surface Phonon Polaritons. We have performed an optimization of the geometrical parameters of both structures and compared the efficiencies of focusing. For these optimum parameters, cone shows about four times more efficient concentration of thermal energy through Surface Phonon Polaritons than wedge.

Based on numerical simulations, we have demonstrated a superfocalisation of infrared radiation diffracted by subwavelength apertures using thin glass membranes. We show that the diffraction angles of such a system can be more than twice smaller than the one of just an aperture. We have also demonstrated that even for the apertures smaller than the wavelength, our system provides a directive radiation.

We have detected that thin suspended polar dielectric membranes support long-range thermally excited surface waves for a significantly broader frequency range than is usually assumed. In fact, we have experimentally demonstrated that 1 μm thick SiO_2 suspended membrane supports thermally excited surface modes from 11.53 μm to 2.68 μm, whereas an interface between two semi-infinite materials only supports surface waves from 9.33 μm - 8.65 μm. We have demonstrated a broadband coherent thermal source in this frequency range and have measured a very long spatial coherence length (reaching almost 100 wavelengths for Zenneck modes). The contribution of these modes to the in-plane thermal conductivity of thin suspended membranes has been demonstrated to be almost 40 times higher than the phononic one for a 50 nm thick amorphous SiO_2 suspended membrane.

Finally, as a part of an ANR project, we have developed an experimental Infrared spectroscopy methodology of micro-characterization of highly selective IR mirrors used for quantum cascade lasers. We performed parametric optimization of the mirrors in order to achieve the best laser performance and did a precise infrared reflectivity mapping of a micro sized optical device for narrow range of incidence angles close to zero.

In the future, we are planing to demonstrate experimentally superfocalisation of infrared radiation through long-range surface waves for sub-wavelength apertures. We also planing to measure the contribution of thermally excited SPhPs and Zenneck modes to the total thermal conductivity of thin dielectric membranes.

References

Agranovich, V. M. and D. L. Mills (1982). *Surface Polaritons - Electromagnetic Waves at Surfaces and Interfaces.* North-Holland: Elsevier Science Ltd. *(p. 21)*

Arfken, G. B. and H. J. Weber (2001). *Mathematical Methods for Physicists.* San Diego, USA: Harcourt/Academic Press. *(p. 22)*

Babadjanyan, A. J., N. L. Margaryan, and K. V. Nerkararyan (2000). Superfocusing of surface polaritons in the conical structure. *J. Appl. Phys. 87*, 3785–3788. *(p. 17, 27)*

Bouhelier, A., T. Huser, H. Tamaru, H. J. Guntherodt, D. W. Pohl, F. I. Baida, and D. V. Labeke (ï¿½ï¿½2001). Plasmon optics of structured silver films. *Phys. Rev. B 63*, 155404. *(p. 16)*

Bouwkamp, C. (1950). On sommerfeld's surface wave. *Phys. Rev. 80*, 294. *(p. 67)*

Cendejas, R. A., M. C. Phillips, T. L. Myers, and M. S. Taubman (2010). Single-mode, narrow-linewidth external cavity quantum cascade laser through optical feedback from a partial-reflector. *Optics express 18*(25), 26037–26045. *(p. 116)*

Chalopin, Y., H. Dammak, M. Hayoun, M. Besbes, and J.-J. Greffet (2012). Size dependent infrared properties of mgo nanoparticles with evidences of screening effect. *Appl. Phys. Lett. 100*, 241904. *(p. 29)*

Chen, D.-Z. A., A. Narayanaswamy, and G. Chen (2005, Oct). Surface phonon-polariton mediated thermal conductivity enhancement of amorphous thin films. *Phys. Rev. B 72*, 155435. *(p. xv, 10, 15, 68)*

Datsko, V. and A. Kopylov (2008). On surface electromagnetic waves. *Phys. Usp. 51*, 101–102. *(p. 67)*

de L. Kronig, R. (1926). On the theory of dispersion of x-rays. *J. Opt. Soc. Am. 12*, 547–557. *(p. 92)*

Faist, J., F. Capasso, D. L. Sivco, C. Sirtori, A. L. Hutchinson, A. Y. Cho, et al. (1994). Quantum cascade laser. *Science 264*(5158), 553–555. *(p. 115)*

Fan, S. (2014). Photovoltaics: An alternative sun for solar cells. *Nature nanotechnology 9*(2), 92–93. *(p. xi, 7, 8)*

Gluchko, S., J. Ordonez-Miranda, L. Tranchant, T. Antoni, and S. Volz (2015). Focusing of surface phonon-polaritons along conical and wedge polar nanostructures. *Journal of Applied Physics 118*(6), 064301. *(p. 15, 35)*

Gluchko, S., B. Palpant, S. Volz, R. Braive, and T. Antoni (2017). Thermal excitation of broadband and long-range surface waves on sio2 submicron films. *Applied Physics Letters 110*(26), 263108. *(p. 81)*

Greffet, J.-J., R. Carminati, K. Joulain, J.-P. Mulet, S. Mainguy, and Y. Chen (2002, 03). Coherent emission of light by thermal sources. *Nature 416*(6876), 61–64. *(p. xv, 6, 8, 15, 16, 69, 90, 99)*

Griffiths, P. R., J. A. D. Haseth, and J. D. Winefordner (2007). *Fourier Transform Infrared Spectrometry* (2 ed.). Wiley. *(p. 98, 123)*

Hill, D. and J. Wait (1980). On the excitation of the zenneck surface wave over the ground at 10 mhz. *Ann. Télécommun. 35*, 179â“182. *(p. 67)*

Huber, A. J., B. Deutsch, L. Novotny, and R. Hillenbrand (2008). Focusing of surface phonon polaritons. *Appl. Phys. Lett. 92*, 203104. *(p. 9, 16)*

Jackson, J. D. (1998). *Classical Electrodynamics* (3rd ed. ed.). John Wiley & Sons, Inc. *(p. 18, 24)*

John Polo, Tom Mackay, A. L. (2013). *Electromagnetic Surface Waves: A Modern Perspective* (1 ed.). Elsevier Insights. Elsevier. *(p. 5, 67, 70, 73, 74, 100, 101)*

Joulain, K., J.-P. Mulet, F. Marquier, R. Carminati, and J.-J. Greffet (2005). Surface electromagnetic waves thermally excited: Radiative heat transfer, coherence properties and casimir forces revisited in the near field. *Surface Science Reports 57*(3â“4), 59 – 112. *(p. xi, 5, 6, 7, 90, 99, 105)*

Kazarinov, R. (1971). Possibility of amplification of electromagnetic waves in a semiconductor with superlattice. *Sov. Phys.-Semicond. 5*(4), 707–709. *(p. 115)*

Kukushkin, A. (2009). On the existence and physical meaning of the zenneck wave. *Phys. Usp. 52*, 755â“756. *(p. 67)*

Kume, T., T. Kitagawa, S. Hayashi, and K. Yamamoto (1998). Long-range surface modes supported by sio2–ag composite thin films. *Surf. Sci. 395*, 23. *(p. 15)*

Kurihara, K., A. Otomo, A. Syouji, J. Takahara, K. Suzuki, and S. Yokoyama (2007). Superfocusing modes of surface plasmon polaritons in conical geometry based on the quasi-separation of variables approach. *J. Phys. A: Math. Theor. 40*, 12479. *(p. 17, 27)*

Kurihara, K., K. Yamamoto, J. Takahara, and A. Otomo (2008). Superfocusing modes of surface plasmon polaritons in a wedge-shaped geometry obtained by quasi-separation of variables. *J. Phys. A: Math. Theor. 41*, 295401. *(p. 17, 27)*

Laughlin, R. and J. Joannopoulos (1977, September). Phonons in amorphous silica*. *Phys. Rev. B 16*, 2942–2952. *(p. xix, 109, 110)*

Lehmann, A., L. Schumann, and K. Hubner (1983, June). Optical phonons in amorphous silicon oxides. *Phys. Stat. Sol. (b) 117*, 689–698. *(p. 109)*

Marquier, F., K. Joulain, J.-P. Mulet, R. Carminati, J.-J. Greffet, and

Y. Chen (2004, Apr). Coherent spontaneous emission of light by thermal sources. *Phys. Rev. B 69*, 155412. *(p. 90, 99)*

Max, B. and W. Emil (2002). *Principles of Optics: Electromagnetic Theory of Propagation, Interference and Diffraction of Light* (7 ed.). Cambridge University Press. *(p. 46, 50)*

Mills, D. L. (1975). Attenuation of surface polaritons by surface roughness. *Phys. Rev. B 12*, 4036. *(p. 15)*

Moon, P. and D. E. Spencer (1988). *Field theory handbook: Including coordinate systems, differential equations, and their solutions*. New York: Springer-Verlag. *(p. 22)*

Mulet, J. P., K. Joulain, R. Carminati, and J. J. Greffet (2001). Nanoscale radiative heat transfer between a small particle and a plane surface. *Appl. Phys. Lett. 78*, 2931. *(p. 15)*

Nerkararyan, K. V. (1997). Superfocusing of a surface polariton in a wedge-like structure. *Phys. Lett. A 237*, 103–105. *(p. 17, 27, 38)*

Olver, F. W. J., D. W. Lozier, R. F. Boisvert, and C. W. Clark (Eds.) (2010). *NIST Handbook of Mathematical Functions*. Cambridge Univ Press. *(p. 22, 23, 26, 49)*

Ordonez-Miranda, J., L. Tranchant, S. Gluchko, T. Antoni, and S. Volz (2014). Fresnel-like formulas for the reflection and transmission of surface phonon-polaritons at a dielectric interface. *Phys. Rev. B 90*, 155416. *(p. 16)*

Ordonez-Miranda, J., L. Tranchant, B. Kim, Y. Chalopin, T. Antoni, and S. Volz (2014a). Effects of anisotropy and size of polar nano thin films on their thermal conductivity due to surface phonon-polaritons. *Appl. Phys. Express. 7*, 035201. *(p. 30)*

Ordonez-Miranda, J., L. Tranchant, B. Kim, Y. Chalopin, T. Antoni, and S. Volz (2014b). Quantizedthermal conductance of nanowires at room temperature due to zenneck surface-phonon polaritons. *Phys. Rev. Lett. 112*, 055901. *(p. 16, 21, 31)*

Ordonez-Miranda, J., L. Tranchant, T. Tokunaga, B. Kim, B. Palpant, Y. Chalopin, T. Antoni, and S. Volz (2013). Anomalous thermal conductivity by surface phonon-polaritons of polar nano thin films due to their asymmetric surrounding media. *J. Appl. Phys. 113*, 084311. *(p. xv, xix, 10, 16, 30, 68, 74, 105, 109, 111, 112)*

Oskooi, A. F., D. Roundy, M. Ibanescu, P. Bermel, J. D. Joannopoulos, and S. G. Johnson (2010, January). MEEP: A flexible free-software package for electromagnetic simulations by the FDTD method. *Computer Physics Communications 181*, 687–702. *(p. 51, 82, 94)*

Palik, E. D. (1985). *Handbook of Optical Constants of Solids*. Orlando: Academic. *(p. xii, xiii, xvi, 29, 30, 40, 52, 76, 77, 93)*

Rao, G. N. and A. Karpf (2011, Feb). External cavity tunable quantum cascade lasers and their applications to trace gas monitoring. *Appl. Opt. 50*(4), A100–A115. *(p. 117)*

Rephaeli, E., A. Raman, and S. Fan (2013). Ultrabroadband photonic structures to achieve high-performance daytime radiative cooling. *Nano letters 13*(4), 1457–1461. *(p. xi, 8, 9, 10)*

Ropers, C., C. C. Neacsu, T. Elsaesser, M. Albrecht, M. B. Raschke, and C. Lienau (2007). Grating-coupling of surface plasmons onto metallic tips: A nanoconfined light source. *Nano Lett. 7*(9), 2784–2788. *(p. 16)*

Sarnthein, J., A. Pasquarello, and R. Car (1997). Origin of the high-frequency doublet in the vibrational spectrum of vitreous sio2. *Science 275*(5308), 1925–1927. *(p. 109)*

Schuller, J. A., T. Taubner, and M. L. Brongersma (2009). Optical antenna thermal emitters. *Nat. Photon. 3*, 658–661. *(p. 99)*

Sommerfeld, A. (1909). Über die ausbreitung der wellen in der drahtlosen telegraphie. *Ann. Phys. Lpz. 28*, 665â"736. *(p. 67)*

Taflove, A. (2013). *Advances in FDTD Computational Electrodynamics* (1 ed.). Artech House. *(p. 51)*

Udagedara, I. B., I. D. Rukhlenko, and M. Premaratne (2011, Mar). Complex-ω approach versus complex-k approach in description of gain-assisted surface plasmon-polariton propagation along linear chains of metallic nanospheres. *Phys. Rev. B 83*, 115451. *(p. 109)*

Vernon, K. C., D. K. Gramotnev, and D. F. P. Pile (2007). Adiabatic nanofocusing of plasmons by a sharp metal wedge on a dielectric substrate. *J. Appl. Phys. 101*, 104312. *(p. 16)*

Wilde, Y. D., F. Formanek, R. Carminati, B. Gralak, P. A. Lemoine, K. Joulain, J. P. Mulet, Y. Chen, and J. J. Greffet (2006). Thermal radiation scanning tunnelling microscopy. *Nature 444*, 740. *(p. 15, 16)*

Yang, F., J. R. Sambles, and G. W. Bradberry (1991, Sep). Long-range surface modes supported by thin films. *Phys. Rev. B 44*, 5855–5872. *(p. 69, 70, 73, 74, 100, 101, 102)*

Zenneck, J. (1907). Über die fortpflanzung ebener elektromagnetischer wellen längs einer ebenen lieterfläche und ihre beziehung zur drahtlosen telegraphie. *Ann. Phys. Lpz. 23*, 846â"866. *(p. 67)*

université PARIS-SACLAY
ÉCOLE DOCTORALE
Sciences mécaniques et énergétiques, matériaux et géosciences (SMEMAG)

Titre: Manipulation d'Énergie Thermique avec des Ondes de Surface Électromagnétique aux Échelles Micro- et Nanoscopiques

Mots-clés: transfert thermique, conductivité thermique, ondes de surface, phonons polaritons de surface, ondes de Zenneck, radiation thermique, champ proche, spectroscopie infrarouge, microscopie infrarouge.

Résumé: Les phonons polaritons de surface (SPhPs) sont des ondes électromagnétiques de surface évanescentes générées par le couplage phonon-photon et se propageant le long d'une interface entre un milieu polaire (tel que SiO_2 et SiC) et un diélectrique. Dans ce mémoire, nous nous intéressons à de possibles applications des SPhPs pour améliorer les performances thermiques des nanosystèmes, en focalisant leur énergie thermique avec des micro- et nanostructures, en réduisant leurs angles de diffraction à travers des ouvertures sub-longueur d'onde, et en démontrant leur émission thermique cohérente large-bande. Nous avons aussi effectué des mesures par microscopie spectrophotométrique infrarouge de micro-objets et démontré l'excitation thermique de modes de grandes longueurs de propagation dans un large domaine spectral. Nos résultats sont obtenus sur des bases à la fois théoriques, de simulations numériques et expérimentales. Ces travaux sont pertinents dans les domaines liés au transfert thermique, à l'optique infrarouge, au rayonnement thermique de champ proche, à la microscopie infrarouge, et à la polaritonique.

Title: Thermal Energy Manipulation via Electromagnetic Surface Waves at Micro and Nanoscales

Keywords: heat transfer, thermal conductivity, surface waves, Surface Phonon Polaritons, Zenneck waves, thermal radiation, near-filed, infrared spectroscopy, infrared microscopy.

Abstract: Surface phonon-polaritons (SPhPs) are evanescent electromagnetic surface waves generated by the phonon-photon coupling and that propagate along the interface of a polar medium (such as SiO_2 and SiC) and a dielectric one. In this work, we investigate possible applications of SPhPs for enhancing the thermal performance of micro- and nanoscale devices, focusing of thermal energy with micro-structures, decreasing the diffraction angles of infrared radiation on sub-wavelength apertures, and demonstrating broadband coherent thermal emission. We also perform infrared spectroscopy microscopy measurements of microscale objects and demonstrate long-range thermally excited surface modes in a broad frequency range. The results presented in this thesis can have possible applications in fields related to heat transfer, infrared optics, near-field thermal radiation, infrared microscopy, and polaritonics.